UNIVERSITÀ
DEGLI STUDI
DI PADOVA

Sede Amministrativa: Università degli Studi di Padova

Dipartimento di Fisica e Astronomia "Galileo Galilei"

CORSO DI DOTTORATO DI RICERCA IN: FISICA

CICLO XXIX

Development of computational methods for the analysis of conductance and unitary permeability of channels formed by connexins involved in hereditary deafness

Coordinatore: Ch.mo Prof. Gianguido Dall'Agata

Supervisore : Ch.mo Prof. Fabio Mammano

Co-Supervisore : Ch.mo Prof. Francesco Zonta

Dottorando : Damiano Buratto

Abstract

This Ph.D. research project focused on the study of channels composed of connexin 26 (Cx26) protein subunits. In particular, we analyzed conductance, permeability and/or structural differences of deafness-related mutations of Cx26 intercellular gap junction channels or unpaired hemichannels, using different molecular dynamics approaches and statistical mechanics.

The **first part** of this thesis introduces the structure of gap junction channels and the connexin proteins that form them. Next, it dwells on the function of gap junction channels and connexin hemichannels, particularly on their *conductance* and *permeability*, two fundamental properties explored in the rest of the work. This introductory section contains also a brief overview of *electrophysiology* experiments performed on connexin channels. It ends with a section on *gating properties* that modify conductance state and a discussion of disease-related connexin *mutations*. The **second part** presents the key results obtained during this Ph.D. work, beginning with the full atom model on which the work was based, and a discussion of the improvements achieved during this project. The rest of the results are subdivided into three topics: (a) *structural analysis*, (b) *conductance* and (c) *permeability*.

a) This section summarizes the results obtained for the mutant Cx26 C169Y, the analysis of which shows a large displacement of the extracellular loops and, consequently, of residues critically involved in hemichannel *docking*.

b) This section introduces two methods to compute the ionic conductance of a connexin hemichannel and applies them to three different models: the mutant Cx26 M34T, the WT Cx26 hemichannel in a Coarse-Grained representation and the full-atom WT hemichannel model bound to an antibody.

c) This section starts with the explanation of the method used to compute the potential of mean force (PMF) for the passage of a molecule through the channel pore and a possible interpretation of this potential. The PMF was then used to quantify permeation of different molecules (IP_3, ATP) through Cx26 WT and V84L mutant hemichannels. The chapter ends with a structural analysis which accounts for the differences in the permeability of the two models.

This thesis also contains an overall discussion of the results highlighted above and a methodological appendix.

Contents

Introduction

The survival of multicellular organisms depends on the individuality of each cell type, even though all cellular activities must be coordinated with other cells. In order to achieve this, organisms have evolved multiple strategies such as long-range or short-range interactions that include direct physical or cell-to-cell contact. While the first strategy involves interactions at a distance, one mode of direct communication involves the cell-to-cell transmission of molecules through channels in a specialized cell surface membrane structure, so-called *gap junction channels* (GJCs) [1].

A number of independently pursued and unrelated studies indicated gap junctions as discrete plasma membrane domains were most likely to account for direct cell-cell communication. Pioneering work in the 1950*s* on fast excitatory transmission in the giant fibre system [2] of crayfish and in the neurons of lobster cardiac ganglion [3] indicated that these cells communicated directly via electrical pathways. As recollected by Bennett in Ref. [4], electrical synapses allow multiple cells to act with almost the same precision as a single cell, but at the time, the emerging conclusions contradicted the prevailing view of animal cells as independent entities surrounded by an electrically insulating membrane and communicating solely by release of extracellular messengers. Controversies regarding the relative contributions and importance of chemical synapses and electrical junctions as modes of communication in the nervous system have continued, but with increasing acceptance that both mechanisms of inter-cellular communication often operate in parallel. A significant morphological advance in deducing the membrane basis of potential cell-cell communication pathways used Mauthner cell synapses in goldfish brains, where a striking hexagonal arrangement of apposed channels was observed [5]. Although the biochemical identification of gap junction proteins would take a further 18 years [1, 6], these earlier morphological approaches contributed to drawing clearer functional distinctions between chemical and electrical junctions and between gap junctions and tight junctions.

Gap junctions are present in virtually all tissues of the body, with the exception of fully developed adult skeletal muscle and mobile cell types such as sperm or erythrocytes. Even loosely associated aggregates of cells, as in lymph glands [7] and haemopoietic tissue [8–10], are organized as interacting cellular networks extensively coupled by gap junctions [11]. Over the years, Gap Junction channels and hemichannels have been experimentally well characterized. The patch-clamp and double path-clamp techniques played a fundamental role in the characterization of two of the most important properties of these channels: *conductance* and *unitary permeability* to small molecules. These techniques were largely used to characterize the conductance of different Gap junction channels and hemichannels [12,13]. Moreover, in the last decade, a combination of dual patch-clamp recordings and Ca^{2+} fluorescence resonance energy transfer (FRET) was proposed to compute the unitary permeability of the Gap junction to small molecules [14, 15].

Despite the incredibly large amount of data produced on the physiological properties of gap junction channels and the pathological behaviour generated by mutation in the connexin proteins forming the gap junction channels, we are far from completely understanding their behaviour. In vertebrates, Gap Junction channels are formed by a family of proteins named connexins that, in humans, count 21 isoforms. Most of the properties of the Gap Junction channels, like conductance, unitary permeability and gating mechanism, depend on the connexins isoform that make up the Gap Junction and these properties did not seem to be correlated with each other [16]. This difficulty was also exacerbated by the fact that the structure of a gap junction channels was unknown until 2009 when the first high resolution X-Ray crystal structure of a human Gap junction channel was published [17]. This work provided an invaluable insight into the understanding of the properties of gap junction channels and hemichannels, and also opened the possibility of using computational techniques like molecular dynamics (MD) simulations, to better understand the mechanisms underlying the behaviour of the system at spatial and temporal resolutions that challenge current experimental techniques. Molecular Dynamics simulations are increasingly being partnered with experiments in this quest because simulations can track system behaviour across a vast spatiotemporal domain-with length scales up to thousands of angstroms, with atomic precision, and timescales up to milliseconds, at femtosecond resolution.

Molecular dynamics simulations are based on a classical description of the system. During the simulation, the trajectories of atoms and molecules are determined by numerically solving Newton's equations of motion for a system of interacting particles, where forces between the particles and their potential energies are calculated using a potential that takes into account electrostatic, Van der Waals and chemical bounds. The set of parameters that describe this potential is called a *force field*. Despite the limitations due to the time scale that can be achieved, (from hundreds of nanoseconds up to dozens of microseconds depending on the type of model used) and the limitations due to the use of a classical approach instead of the Schrodinger equation, MD can be extremely useful in understanding and interpreting the experimental results, thus giving an insight at molecular level. Even if we are not able to completely predict the behaviour of the system using MD simulations, the huge progress of these years, especially in computing power, may open huge opportunities in the next few years and is always worth investigating in this field.

After the publication of the X-Ray crystal structure, the structure of the channel was revealed and reliable computational models started to be built [18–22]. These models were used to gain an insight in the dynamics of the Gap Junction channel. Moreover, a lot of effort went into reproducing the experimental result of conductance and unitary permeability to small molecules [19, 20].

The **aim** of this thesis work is to extend the work on the Gap Junction model. Our purpose is to use the molecular dynamics technique in order to understand, reproduce and eventually predict the experimental results obtained for wild type and deafness related mutants of the connexin proteins that constitute Gap Junction channels. In particular, we will focus on the study of permeability and conductance, the two phenomenological parameters that are used to describe the passage of permeants through channels such as the Gap Junction using Molecular Dynamics methods. Both of these parameters contain information about how easy or difficult it is for a permeant to enter a channel, move through it, and exit on the other side, but in some cases conductance and permeability can report different aspects of the permeation process. In general, using MD methods we found an atomistic explanation that explains the experimental results for the behaviour of

the deafness related mutations we studied, but we were still unable to produce quantitative results.

This work is separated into three parts. The first part is made up of two chapters in which will briefly introduce the biological system that we intend to study. In chapter 1 the structure of the membrane channel and the connexin proteins that form it is introduced. In chapter 2 we examine the principal functions and properties of the Gap Junction channels and hemichannels.

The second part discusses to the results obtained. In chapter 3 the computational model we used for this work is explained, and in chapter 4 we present the results with a structural analyses of the trajectory obtained with equilibrium molecular dynamics of Cx26WT and the natural C169Y mutation model. In chapter 5 two different methods for computing the conductance of a connexin hemichannel using molecular dynamics are introduced; these methods were applied to Cx26WT and the natural M34T mutation model, a system made of Cx26WT and a human antagonist antibody for Cx26 and a Coarse Grained model of Cx26WT. In chapter 6 the problem of computing the unitary permeability of the hemichannel to small molecules is introduced and the Umbrella Sampling method used to compute it is explained, showing the preliminary results obtained for the passage of small molecule through wild type and the natural V84L mutant hemichannel model.

The third part is dedicated to the discussion of the results.

Part I

Introduction to Connexin Channels

Chapter 1

Key structural features

In vertebrates gap junction channels are constructed by the serial docking of two hemichannels (HCs), or connexons. They spans the plasma membranes of two adjacent cells allowing the exchange of cytoplasmic molecules with sizes up to $\sim$ 1 kDa [23]. Thousands of docked connexon pairs are tightly packed into Gap Junctional plaques that are planar, double-layered structures with distinct boundaries (Figure 1.1) and leave a gap of 2–4 nm between the two cells.

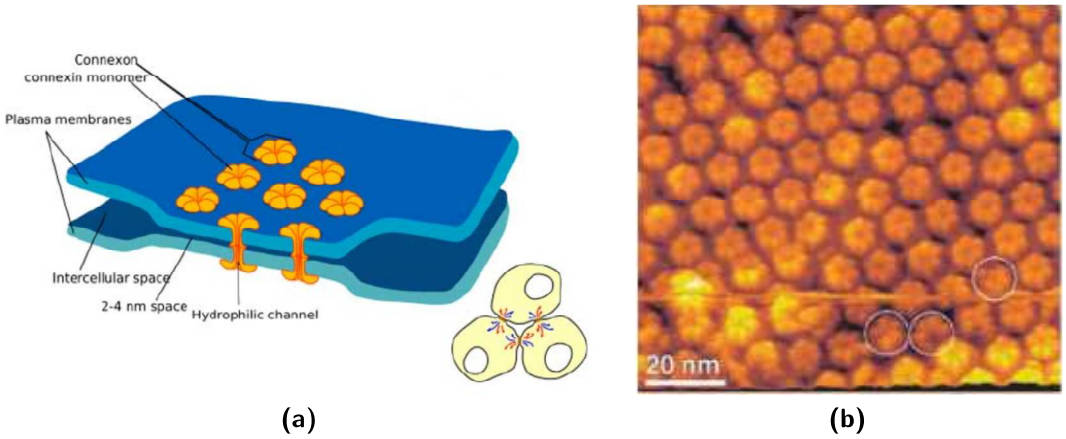

Figure 1.1: **(a)** Model of a gap junction [11]. The hexameric connexin sub-units in each of the plasma membranes dock to generate the gap junction channel connecting the two cytoplasmic compartments. **(b)** Extracellular connexon surface of a GJCs plaque recorded with atomic force microscopy (AFM) [24, 25]. AFM topograph showing the connexon arrangement. Individual connexons exhibit defects of the size of single connexins as indicated by circles.

Hemichannels are hexamers made of a six protein subunit called connexins (Cxs; see Section 1.1)[1] Every hemichannel is about 70 Å wide and from 85 Å to 125 Å long, depending on the CT size of the constitutive connexin protein. Each connexon protrudes about 15–20 Å from the membrane face into the extracellular gap. The two connexons forming the junctional channel are not aligned. Indeed, between the two connexons there is a 30° rotation which brings each connexin into direct apposition with parts of two connexins

[1] In Vertebrate exist another family of protein (named Pannexin) that can form gap junction channels. In invertebrate a similar family of protein (named Innexin) was found to form gap junction channels. In our work we will treat only the Connexin protein.

in the opposing hemichannel. Early structural information about gap junction channels came from atomic electron microscopy (EM), X-ray diffraction patterns and atomic force microscopy (AFM) [26]; the latter provided the first insight into the connexon extracellular surface structure [27, 28]. The high resolution 3D structure of a gap junction channel at 3.5 Å resolution was obtained by X-ray diffraction in 2009 [17] (Figure 1.2) and more recently in [29].

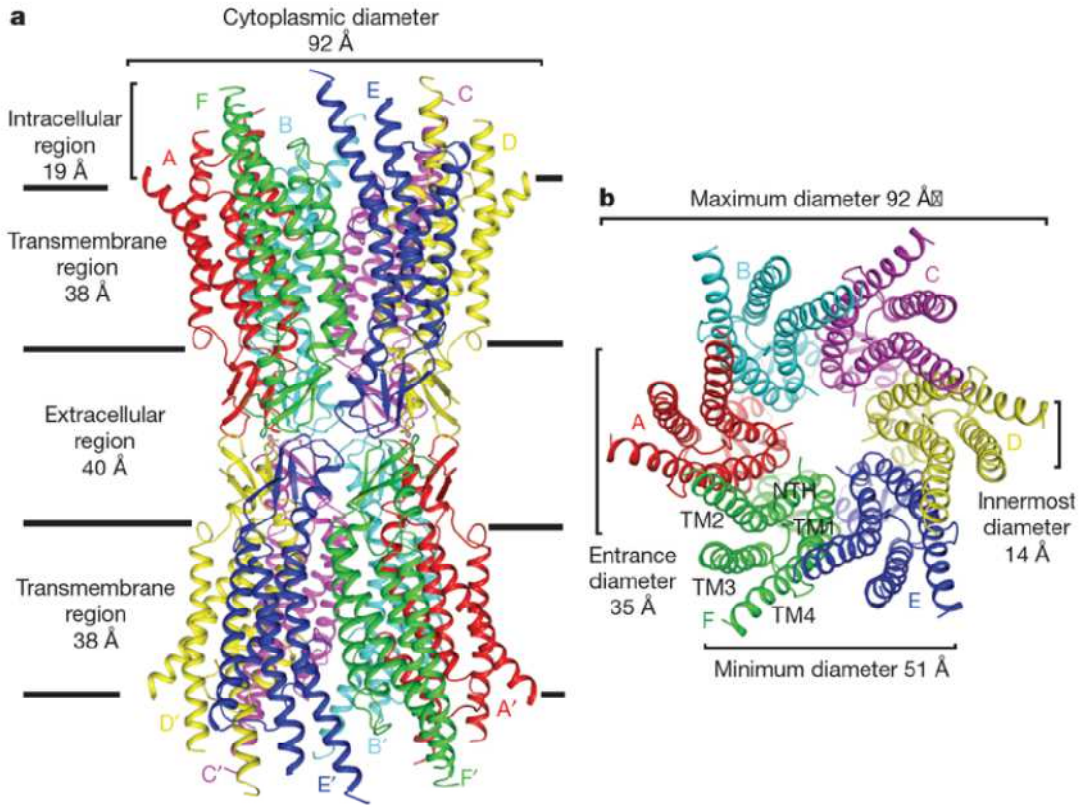

Figure 1.2: Junctional channel structure from X-ray crystallography , by Maeda et al. [17]. The structure is formed by two hemichannels which dock on the extracellular side, one of which is rotated by about 30° with respect to the other. The gap junction crystal structure is made of human connexin 26 (see Section 1.1), that is the connexin we are interested in.

Around 21 highly homologous products of connexin genes have been identified in humans [30]. Since most cell types express more than one connexin isoform, connexin channels come in several types. The most commonly studied are the simplest **homomeric** junctional channels, which are entirely composed of a single connexin isoform. **Heterotypic** junctional channels are composed wholly of a single connexin isoform for each hemichannel, but different isoforms compose the two hemichannels. **Heteromeric** hemichannels are composed of more than one connexin isoform (Figure 1.3).

1.1 Connexins

Connexins are identified as a family of proteins by sequence similarity and inferred transmembrane topology [31]. As we have previously said, there are at least 21 human

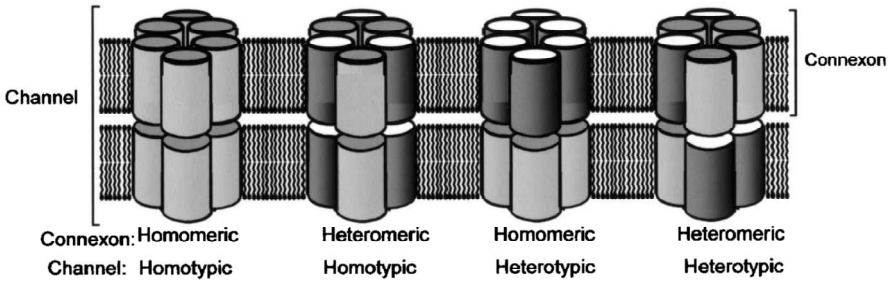

Figure 1.3: Gap Junction channels [11]. Possible arrangements of connexins in a gap junction channel unit.

isoforms of connexins [30], with a high degree of conservation among species. Each connexin is named for its predicated molecular weight, *i.e.* Cx26 is the isoform with molecular weight of 26 kDa, Cx43 is the 43 kDa isoform and so on [31]. Where it is important to designate species-specific orthologs, a lower-case prefix is added, as in $cCx42$ for chick $Cx42$, $hCx46$ for human $Cx46.6$, $mCx32$ for murine $Cx32$, $rCx26$ for rat $Cx26$ or $zCx45$ for zebrafish $Cx45$.

The structure of connexin proteins and their assemblies was largely unknown until the publication of the already mentioned model based on high resolution (3.5 Å) X-ray data of a hCx26wt channel [17]. The X-ray model permits to tackle issues left unresolved by previous models based on lower resolution data [32–35] such as the correct position of transmembrane helixes and the structure of extracellular regions.

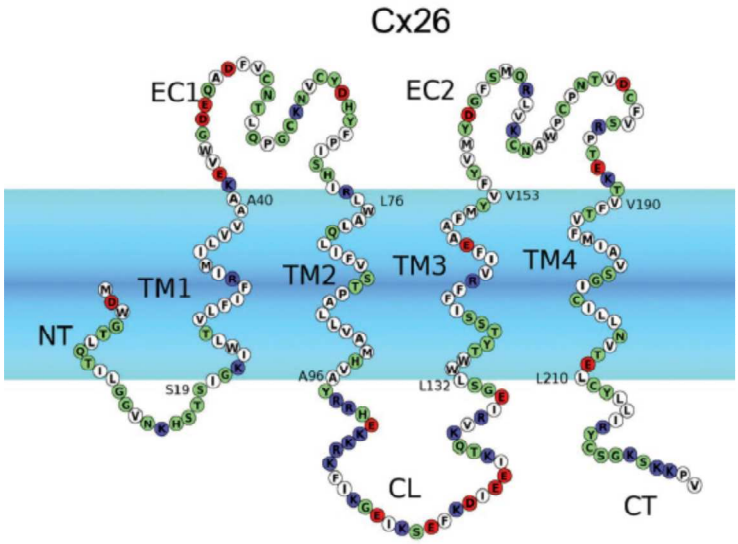

Figure 1.4: hCx26 topology representation [19]. NT, N-terminus; CT, C-terminus; TM1-TM4, transmembrane helices 1 to 4; CL, cytoplasmic loop connecting TM2, TM3; EC1, EC2, extracellular loops connecting TM1 to TM2 and TM3 to TM4, respectively. Residue color code: blue, positive; red, negative; white, hydrophobic; green, hydrophilic.

Despite significant variation in length, primarily in the cytoplasmic domains, all connexin proteins are supposed to share the same topology. Each connexin has four

predominantly hydrophobic, membrane-spanning regions (TM1-TM4) (Figure 1.4). The carboxy- and amino-domains (CT and NT, respectively) are accessible from the cytoplasm, as is the hydrophilic cytoplasmic loop (CL) domain between TM2 and TM3. The hydrophilic domains between TM1 and TM2 and between TM3 and TM4 are accessible from extracellular space and form extracellular loops EC1 and EC2. The length of the CT varies among connexins and is responsible for most of the differences in molecular mass. The transmembrane domains and extracellular loops are also highly conserved across connexins.

Moreover, the X-ray data show that, when assembled in hexamers, hCx26wt subunits create an aqueous pore in the plasma membrane (with a minimum diameter of $\sim 1.2\ nm$), whose walls are formed by TM1 and TM2, plus the NT that folds inside the pore at the cytoplasmic mouth of the channel (Figure 1.5a).

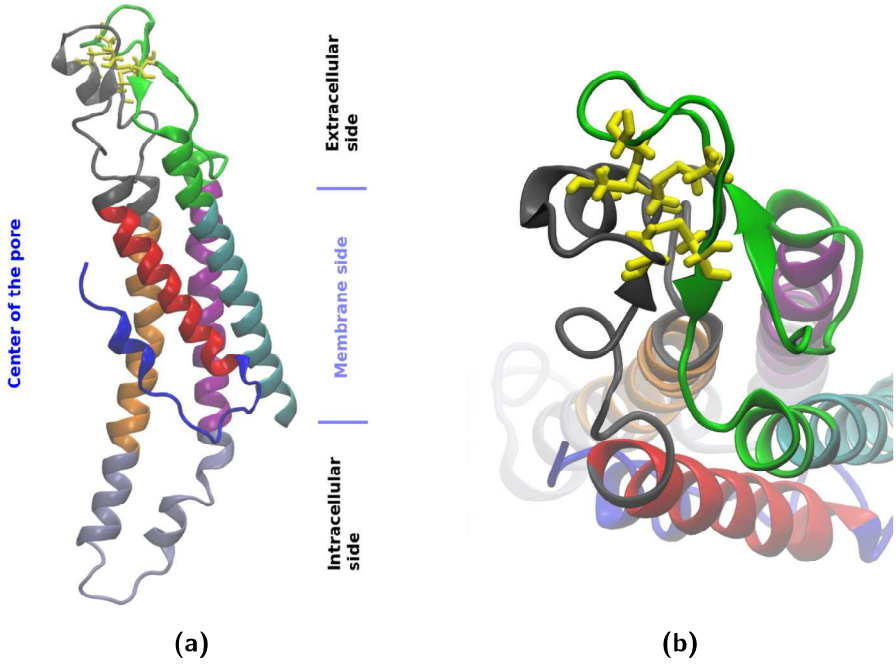

Figure 1.5: Cx26 structure representation. **(a)** side view of a connexin protein with membrane on the left and the center of the pore on the right. The transmembrane helixes (TM1-4) are drawn in red, orange, purple and cyan, respectively. The extracellular loops (EC1-2), N- and C- teminus are drawn in black, green, blue and ochre respectively. **(b)** Top view of the protein with the three pairs of disulphide bridge highlighted in yellow.

The two extracellular loops are thought to be involved in initiating the interaction between connexons in adjacent cells. A set of three cysteine residues exists in each of the extracellular loops with a characteristic arrangement that is a signature of connexins. These three pairs of disulphide bridge (Figure 1.5b) that help to maintain the rigid tertiary structure and enables two opposing connexons to dock with each other [22]. The regions between the transmembrane domains TM2 and TM3, as well as the CT of the connexins, are highly variable among the different connexins and are, therefore, thought to be important for regulation.

In this work, we will focus our attention on hCx26, which is composed by 226 amino acids and is one of the smallest member of the connexin family.

Chapter 2

Key functional characteristics

As stated in the introduction, the importance of electrical and molecular signalling through gap junction channels is widely recognized [16, 36, 37].

Gap junctions may be seen to function at the simplest level as a direct cell to cell pathway for electrical currents, small molecules and ions. They appeared not only to be key in the development of cell polarity [38] and the left/right symmetry/asymmetry in animals [39, 40], but also the more fundamental differentiation of cells at later stages of embryonic development [41–44]. Moreover, gap junctions are particularly important in diverse tissues, notably **cardiac muscle**, where the signal to contract is passed efficiently through gap junctions, allowing the heart muscle cells to contract in unison, **in skin tissue**, which is heavily dependent upon gap junction communication for the regulation of differentiation and proliferation, **in the inner ear**, where they regulate the normal development, function and repair of the sensory epithelia cells and **in neurons**, where they are often referred to as electrical synapses. (The electrical synapse was discovered using electrical measurements before the gap junction structure was described.) Similar examples stand **for virtually every tissue** [45].

It was formerly believed that hemichannels could not or should not function as channels, that opening the hemichannel would be lethal, or would have to be artifactual, without biological relevance or experimental utility [46]. Only more recently has it been noted that connexin hemichannels open in response to various types of stimuli and conditions, including mechanical, shear, ionic and ischemic stress and provide a pathway for the release of intracellular ATP, *glutamate*, NAD^+ and *prostaglandin* $E2$, which act as paracrine messengers [36]. Increasing evidence shows that undocked HCs may have functional relevance in cell physiology allowing diffusional exchange of ions and small molecules between intra- and extra-cellular compartments. Compelling evidence for conducting hemichannels in the plasma membrane of native cells was first obtained from the horizontal cells of catfish retina [47]. Solitary horizontal cells, when in a low calcium medium, exhibit a plasma membrane conductance that is permeable to lucifer yellow. It is regulated by voltage, $cAMP$, $cGMP$, *dopamine*, and *intracellular* pH in a manner similar to the regulation of gap junction channels in pairs of the same cells. Moreover, recent studies have shown the importance of the ATP release from HCs for the spread of calcium waves in non-sensory cell networks of the developing cochlea [48]

2.1 Conductance and Permeability

Each different connexin channel show distinct conductance and permeability properties, and it is difficult to experimentally determine exactly which cytoplasmic ion or molecule can pass through the channels, how well, and which does not [16]. Generically, the pores of connexin channels are sufficiently wide (nominally $\sim 12\,\text{Å}$) to be permeable to a wide variety of cytoplasmic molecules. There is evidence for permeation through at least some types of connexin channels of virtually all soluble second messengers, amino acids, nucleotides, calcium ions, and glucose and its metabolites [45]. At first, the expectation was that any cytoplasmic molecule of appropriate size would permeate connexin channels, and that the limiting (*i.e.*, minimum) pore diameter would be the primary determinant of molecular permeation [16]. It had also been widely presumed that, due to the relatively large pore diameter, there would not be significant charge selectivity among permeants. Both expectations were incorrect: pore diameter, while obviously important, does not account for the observed molecular selectivities, and many connexin channels exhibit substantial charge selectivity, even among monovalent atomic ions [12]. Since conductance and permeability are the most important properties of the gap junction channels, we will dedicate the next section to introduce the experimental methodology for their computing.

2.2 Electrophysiology

Since one of the aim of this thesis is the computing of conductance and permeability of a gap junction channel, in this section we introduce the experimental approaches used to study connexin junctional channel and hemichannel current. We will split up our exposition in two parts depending on the kind of measurement: *Macroscopic and single-channel current* and *molecular permeability.*

2.2.1 Macroscopic and single-channel current

Recording of **junctional** current requires *simultaneous voltage-clamp of two coupled cells.* The voltage of each cell is initially clamped to a common potential so that junctional voltage (V_j) equals 0 mV (Figure 2.1). Typically, voltage is imposed across the junctional membrane by stepping the potential in one cell (V_1) while holding that of the other cell (V_2) constant. The current that flows through junctional channels (I_j) as a result of the non-zero V_j (which equals $V_2 - V_1$) is measured as the current supplied to the cell whose potential was unchanged (ΔI_b).

Since the potential in one of the two cells (V_2) is unchanged, the variation of the non-junctional current (ΔI_{m2}) is zero and the current supplied by that clamp equals $|I_j|$ (*i.e.* $\Delta I_b = |I_j|$) even though the currents provided by each circuit are equivalent to the sum of the non-junctional membrane current of that cell plus the junctional current ($I_a = I_{m1} + I_j$ and $I_b = I_{m2} - I_j$) [45].

In cases where the number of functioning channels is sufficiently small, this dual whole-cell patch clamp technique can be used to record currents through **single junctional channels** between mammalian cells (Figure 2.3) [51–55]. This can be achieved by selection of highly resistive cells with very low macroscopic junctional conductance [56], study of newly forming junctional channels [54, 55, 57, 58], or by treatment of coupled cells with

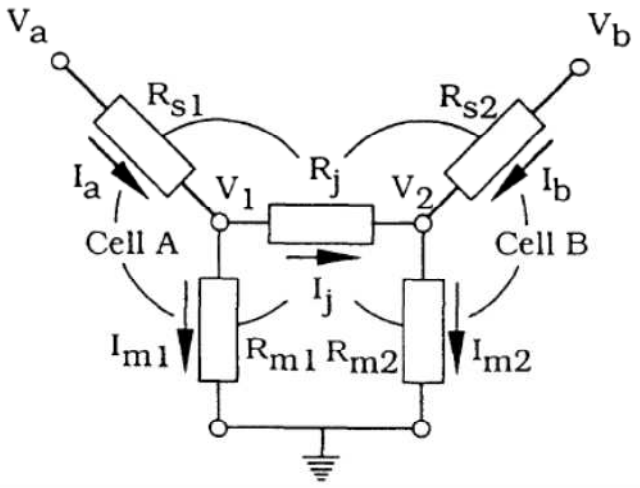

Figure 2.1: Equivalent circuit of dual whole-cell patch-clamp for recording junctional currents of two spherical cells [45]. V = voltage ; I = current ; I_m = current through non-junctional membrane ; R_s = series resistance including electrode resistance ; R_m = resistances of non-junctional membranes. R_j and I_j are junctional resistance and junctional current, respectively. When $V_a = V_b$, $I_j = 0$. If V_a is then stepped to a more positive potential and V_b held constant, $-I_j$ is recorded as the change in I_a [49].

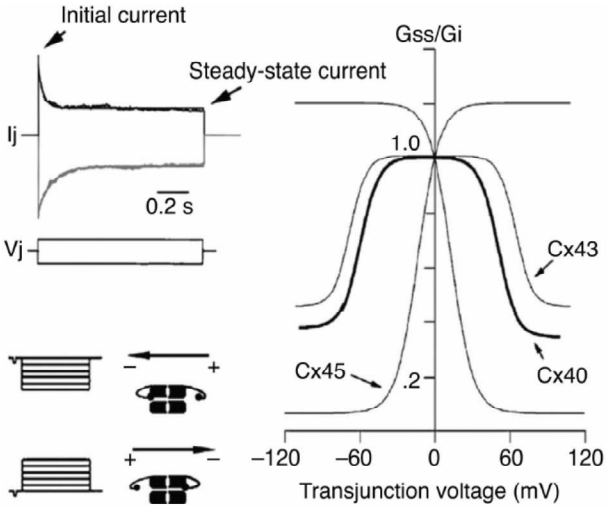

Figure 2.2: Voltage dependence of connexin channels. Voltage dependence of connexin channels. **Upper left** panel shows the current elicited by imposing a plus or minus 100 mV gradient across Cx43 channels. The initial current that decays over time until it reaches a lower steady-state current. **Right panel** shows a plot of the fractional conductance (steady-state conductance Gss divided by the initial conductance Gi) as a function of transjunctional voltage for Cx40, Cx43, and Cx45. **Lower left** panel demonstrates the concept of gating polarity of Cx43 (negative gating polarity, see section 2.3). If the voltage gradient is sufficiently large the gating particle will close the connexion that is relatively negative on the cytoplasmatic side [50].

agents that close junctional channels.

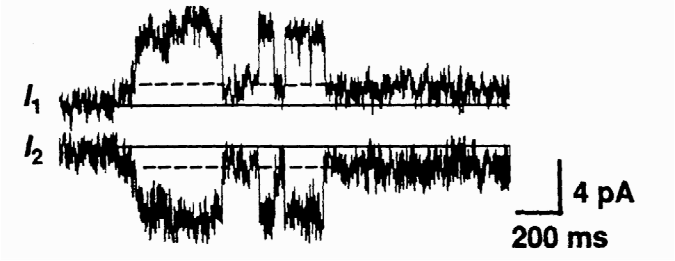

Figure 2.3: Single junctional channel currents recorded by dual whole-cell voltage-clamp [45]. Single junctional channel currents recorded by dual whole-cell voltage-clamp. I_1 and I_2 are clamp currents for two coupled cells, where V_j is maintained at 40 mV. With the opening of a junctional channel, the current enters one cell and leaves the other, resulting in changes in clamp currents of equal magnitudes in opposite directions. The initial slow opening corresponds to the opening of a newly formed junctional channel. This opening is followed by rapid transitions between a high conductance state and a subconductance state, typical of "V_j gating" (see section 2.3) [59].

Macroscopic hemichannel currents can be studied by conventional whole-cell voltage clamp techniques. Under normal conditions, hemichannels do not open except at sustained positive membrane voltages. The development of the outward current is slow, developing over many seconds. Reduction of extracellular calcium ion to 1 mM or less shifts the activation to more negative potentials, and dramatically increases the magnitude and rate of rise of the current [60–64]. There is no factor that uniquely characterizes, activates or inhibits all connexin channels, other than the ability to form channels through two membranes, which is irrelevant to the problem of identifying hemichannels. For these reasons, identification of hemichannel currents in native cells is difficult, and each attempt must be evaluated on its own merits. Most studies of macroscopic hemichannel currents are done in cells in which connexin is heterologously overexpressed.

The electrophysiological techniques for recording **single hemichannel** (Figure 2.4) currents are the same as those for recording other single channel currents. The ability to apply these techniques to hemichannels has had two major limitations. One is that only a subset of wild-type connexins form well-behaved conducting hemichannels. The other is that identifying the channels as formed by connexin protein can be difficult in native cells and in reconstituted systems. The first problem has been addressed by the use of connexins genetically modified to form conductive hemichannels.

2.2.2 Unitary permeability

A key characteristic of connexin **channels** is their permeability to molecules that cannot pass through most other channels (nominal pore diameter 12–14 Å). Intercellular diffusion of fluorescent tracers such as Lucifer Yellow (LY) is commonly used as an indicator of the presence of functional junctional channels. Tracers are also used to characterize the molecular selectivity of connexin channels for size, charge and molecular species. A direct and obvious approach to assess molecular permeability of junctions is to inject fluorescent

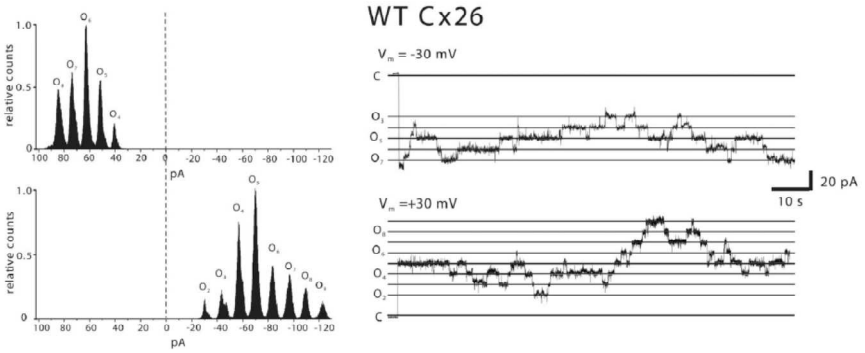

Figure 2.4: Single hemichannel recordings [65]. Multichannel cell-attached patch recordings of Cx26 WT hemichannels. The patch pipette and bath solutions consisted of *IPS* which consisted of (in mM) 140 KCl, 1 $MgCl_2$, 5 $HEPES$, 1 $CaCl_2$ and 3 $EGTA$, pH adjusted to 8.0 with KOH. The currents shown were recorded at $-30\ mV$ and $30\ mV$. Note that open probability (see section 2.3) for WT Cx26 is similar at both voltages. All currents were filtered at 1 kHz, and data were acquired at 5 kHz.

tracer into a cell through a microelectrode or patch pipette and note whether it spreads to adjacent cells [66–68].

The tracer permeability of **hemichannels** in plasma membrane is usually assessed by the ability of cells to become loaded with tracer when it is present in the extracellular medium. This method has been applied to hemichannel studies in Xenopus oocytes [60] and cultured cells [69]. The primary concern is the potential of other plasma membrane channels to mediate the tracer permeability. Until a few years ago, it was nearly axiomatic that only connexin channels would be permeable to tracers such as LY or 6-carboxyfluorescein. Now it is known that several types of membrane channels can be permeable to relatively large tracers and amino acids: several varieties of anion or "chloride" channels [70], channels activated by extracellular ATP [71–73], plasma membrane VDAC [74], and complement channels [75]. Therefore determination that dye permeability is due to hemichannels must rely on connexin-specific modulation of the permeability, specific inhibition by antibodies, or tight correlation with the properties of junctional channels in the same cells.

The first quantitative approach, introduced in 2005 for the analyses of Cx26 V84L mutant [14, 15], is based on a combination of dual patch-clamp recordings and Ca^{2+} fluorescence resonance energy transfer (FRET). As described in [15], monitoring optically the time course of the fluorescence changes in the injected cell (cell 1) and recipient cell (cell 2), the unitary permeability p_u (*i.e.* the permeability of the single pore) can be estimate by

$$p_u = \frac{V_2}{N_{pore}} \frac{dc_2/dt}{c_1 - c_2} \tag{2.1}$$

where V_2 is the volume of cell 2, N_{pore} is the number of open gap junction channels in the plague, c_1 is concentration in cell 1 and $c_2 < c_1$ is concentration in cell 2. Using equation 2.1 and matching the information derived from dual patch-clamp and fluorescent imaging, is it possible to estimate the unitary permeability for a particular molecule. In particular, in the range where the FRET rations $R_{1,2}$ are approximately proportional to c, the unitary permeability can be computed as

$$P_u = \frac{V_2}{g_j/\gamma} \frac{dR_2/dt}{R_1 - R_2} \tag{2.2}$$

where g_j/γ is the estimation of N_{pore} with g_j the conductance of the channel and γ the unitary conductance of the channel (see Figure 2.5).

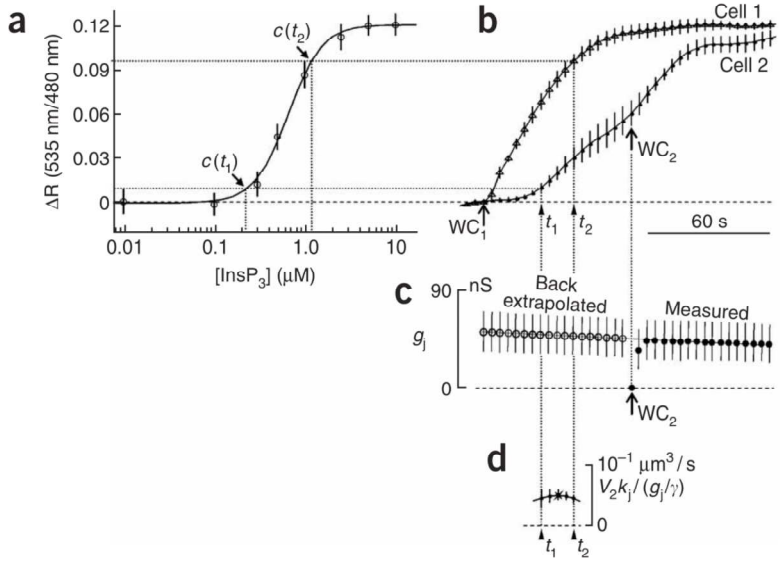

Figure 2.5: Estimate of HCx26wt permeability to IP_3 in pairs of transfected HeLa cells [15]. (a) Concentration-response curve for the IP_3 biosensor, LIBRA ($n \geqslant 5$ cells at each concentration). Ordinates are background-subtracted FRET emission ratio changes ΔR measured from prestimulus ratio R_0 . **(b)** Average FRET ratio traces ($n = 4$) obtained by delivery of 5 mM IP_3 to cell 1 under whole-cell recording conditions (WC_1), followed by delivery to cell 2 (WC_2). **(c)** Intercellular conductance g_j measured after achieving the whole-cell configuration in cell 2 (filled symbols) and back-extrapolated to the $WC_1 - WC_2$ interval (open symbols). **(d)** Estimated unitary permeability to IP_3.

2.3 Gating regulation

The term gating is often used to describe changes in channel opening and closing, *i.e.* a channel which state became either conductive or not conductive [76]. Gap junction channel activity is tightly regulated in response to changes in voltage (transmembrane voltage V_m or by transjuntional voltage V_j) and chemical composition ("chemical gating") of the intracellular milieu, especially by pH and Ca^{2+}. Chemical gating may also occur due to application of exogenous chemicals and pharmacological agents [77]. For simplicity we restrict our discussion to the most well known: gating regulated by the voltage, pH and Ca^{2+}.

Voltage regulation: The most prominent and well-characterized regulation is the sensitivity of macroscopic junctional conductance to the magnitude of transjunctional voltage (V_j).

Over the last two decades, the view of gap junction channel gating has changed from one in witch gap junction channels display a single V_j gating mechanism to one in witch each hemichannel of a formed gap junction channel, as well as unapposed hemichannels, containing two, molecularly distinct gating mechanisms. These mechanisms are termed *fast gating* and *slow* or *"loop"* gating. It appears that the fast gating mechanism is solely sensitive to V_j and induces fast gating transitions between the open state and a particular substate, termed the residual conductance state. The conductance is typically maximal at $V_j = 0$ and relaxes symmetrically and slowly (over hundreds of milliseconds to seconds) for hyperpolarizations or depolarizations of either cell. The slow gating mechanism is also sensitive to V_j, but there is evidence that this gate may mediate gating by transmembrane voltage (V_m), intracellular Ca^{2+} and pH. A distinguishing feature of the slow gate is that the gating transitions appear to be slow, consisting of a series of transient substates en route to opening and closing [78] (see Figure 2.6 for a example of V_j- and *loop*- gating registration).

Earlier studies suggested that the two distinct forms of voltage gating may be localized at opposite ends of a connexin hemichannel in the cytoplasmic NT domain and the extracellular loop domains [79](Verselis et al., 2009; Oh et al., 2000; Purnick et al., 2000b; Tang et al., 2009) [80]. Recent results obtained on N14K mutation had shown a profound effect of this mutation on loop gating, essentially eliminating stable closing events in low extracellular Ca^{2+} conditions (see next section) while V_j gating essentially remained unaffected [81].

Ca^{2+} regulation: The influence of calcium ions on gap junction coupling has been evident for over five decades [45] and was the basis of an early "calcium hypothesis" stating that cytoplasmic calcium ion levels regulate gap junction function [82]. The calcium ion plays important roles in regulating cell processes, so it makes sense that increases in cytosolic calcium, which may be correlated with cell damage as well as necrotic and apoptotic cell death, would be used a mechanism of uncoupling cells [83].

The effect of Ca^{2+} is suggested to act via calmodulin and inhibitors of calmodulin prevents uncoupling in a number of cell types [84]. This proposed mechanisem is supported by expression of calmodulin mutants with increased affinity for Ca^{2+} , showing that increased affinity of calmodulin also increases Ca^{2+} sensitivity of Cx32 [85]. Cx32 has been shown to contain two calmodulin binding domains [86]. With an increase in Ca^{2+} , calmodulin is believed to either physically block the channel or close the channel through a conformational change in Cx32. This may be mediated by transdomain bridging of calmodulin, where calmodulin interacts with the NT and the CT binding sites simultaneously [87]. A role for calmodulin in gating has also been suggested for Cx36 [88], Cx43 [89], Cx44 [90], and Cx45 [77, 91].

Despite the uncoupling cells mechanism related with an increase in intracellular Ca^{2+}, studies on connexin 32 hemichannel showed that an increase of cytoplasmic calcium concentration ($[Ca^{2+}]_i$) triggers hemichannel opening [92].

On contrary, a different gating that involves only hemichannel was showed for a decrease in extracellular calcium concentration ($[Ca^{2+}]$). In this conditions, the non-junctional gap junction hemichannels open [69, 93, 94].

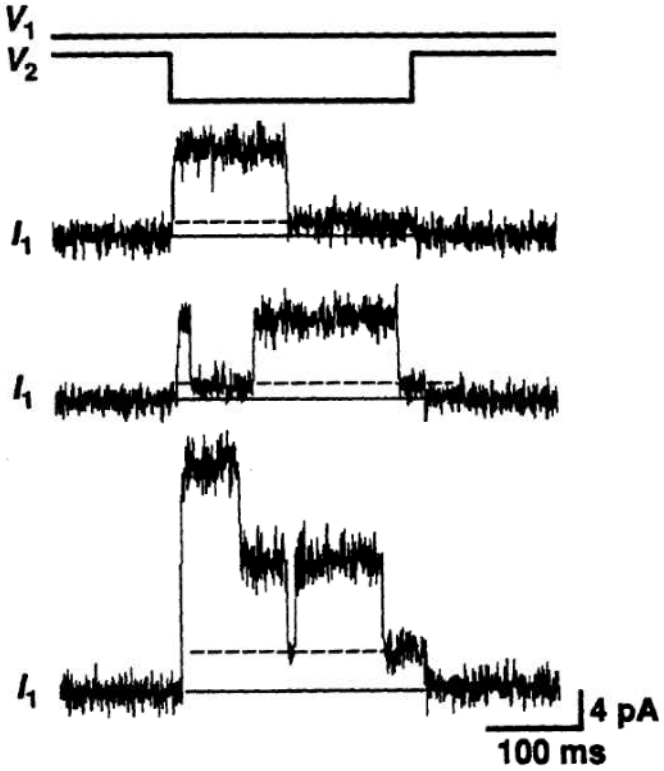

Figure 2.6: V_j**- and** *loop-* **gating in a Cx30 junctional channel. [45].** Channel is open at onset of each current trace, and the first upward transition in each trace reflects the imposition of a junctional voltage. Following this, in each current trace the transitions are (from left to right): (**Upper trace**) rapid transition to subconductance state (Vj-gating) slow transition to closed state (loop-gating). (**Middle trace**) rapid transition to subconductance state (Vj-gating) rapid transition to fully open state (Vj-gating) rapid transition to subconductance state (Vj-gating) slow transition to fully closed state (loop-gating). (**Lower trace**) rapid transition to subconductance state (Vj-gating) transition to fully open state (Vj- gating) transition to subconductance state (Vj-gating) slow transition to fully closed state (loop-gating) [59]. Loop-gating opening transitions are seen also in Fig. 2.3.

pH regulation: Gap junction channels and hemichannel are also known to be regulated by pH. Cytoplasmic acidification induces channel closure via conformational changes in intracellular domains, namely the C-terminus and/or cytoplasmic loop. While the exact mechanism appears to vary between members of the connexin family [45, 95, 96], Cx43 was the first connexin found to gate via a "particle/receptor" mechanism [96]. Low pH triggers interactions between the C-terminus and part of the cytoplasmic loop [97].

2.4 Mutations

As we said, virtually all cells in solid tissues are coupled by gap junctions [23], thus it is not surprising that mutations in connexin genes have been linked to a variety of human diseases, including cardiovascular anomalies, peripheral neuropathy, skin disorders, cataracts, and deafness [98–100]. For connexins, as for most membrane proteins, most mutations result in defects in trafficking, folding or assembly [101]. These defects typically produce a functional

knock-out of the affected connexin. They can also inhibit functional expression of other connexins by a "dominant negative" effect via heteromultimerization with non-mutant connexins. In addition, by analogous mechanism it is possible that mutant connexins could disrupt the function of other proteins with which they interact directly. When the mutants form functional channels, the pathology could be caused by altered permeability properties or by altered channel regulation [45].

Cx32 mutants are the most widely studied, due to the extraordinary number of Charcot Marie-Tooth-X (CMTX) inducing human mutations, which are distributed across the entire coding sequence. CMTX is a progressive atrophy of distal muscles and reduced axonal conduction by Schwann cells [102]. Some of these Cx32 mutations appear to affect the function of gap junctions or hemichannels that provide short-cut cytoplasmic pathways in the adaxonal and perinuclear Schwann cell cytoplasm in the myelin sheath; these radial pathways have been calculated to be a million times shorter than a circumferential route [103]. Mutations in Cx26, of which over 30 have been identified, account for about half of the inherited non-syndromic deafness in the western world and are emerging as the first practical genetic marker of inherited hearing loss [104]. The most common mutation is a recessive mutation ($35delG$) that results in premature stopping of protein translation; a further six dominant mutations are found in the first extracellular loop of Cx26 [105]. Mutations in Cx26 are also increasingly associated with skin diseases [106, 107]. In the lens, mutations in Cx46 and Cx50 are linked with cataract abnormalities [108].

In this thesis we are interested in the study of conductance, permeability and structural configuration for channels made of hCx26 using molecular dynamic techniques. With this in mind we will study mutations of this channel not only out of biological and medical interest but also to use it as a test bench. In order to verify the sensitivity of our model, we will test if the insertion of a single point mutation in the connexin proteins of our model leads to the same differences in conductance and permeability that are seen by performing the same experiment on the same mutant. For this reason, we will take advantage of some experimentally well-characterized mutations of hCx26 channel. In particular we use three of the deafness-related mutations of Cx26: C169Y, V84L and M34T. All these mutations lead to connexons that are correctly formed [109, 110] and targeted to the plasma membrane, but they display differences in conformation, conductance or permeability. We will summarize the experimental results of these mutants in the Results.

Part II

Results

The importance of electrical and molecular signalling through gap junction channels is widely recognized [16, 36]. It is also well established that connexin hemichannels open in response to various types of stimuli and conditions, including mechanical, shear, ionic and ischemic stress and provide a pathway for the release of intracellular ATP, *glutamate*, NAD^+ and *prostaglandin* $E2$, which act as paracrine messengers [36].
Connexin 26 hemichannel has been largely studied from the experimental point of view and well characterized by patch clamp experiments for conductance and permeability to different molecule with important biological functions.
The scope of this thesis is to study permeability and conductance, the two phenomenological parameters that are used to describe the passage of permeants through channels such as the homomeric gap junction hemichannel formed by hCx26 using Molecular Dynamics methods. Both of these parameters contain information about how easy or difficult it is for a permeant to enter a channel, move through it, and exit on the other side, but in some cases conductance and permeability can report different aspects of the permeation process. This difference arises because term permeability can be used as a measure of how readily a permeant will cross a membrane via an open channel. It is a reflection of the nature of the interaction of a particular test permeant with the channel, but can also include a contribution due to competition from other permeants that can limit accessibility of the channel to the test permeant. It is possible in principle, however, to circumvent these latter effects experimentally, and determine a measure of the interaction of the test permeant with the channel in the absence of competition from other permeants. This distinction is important to understand the significance of selectivity measurements that employ either permeability ratios estimated from reversal potentials or conductance ratios estimated from current-voltage relations. Channel conductance and conductance ratios are directly related to the apparent permeability whereas, under ideal conditions, reversal potentials measure the ratio of the intrinsic permeabilities. These two analyses can provide very different, but complementary, information about the permeation process [111].
In the next two chapters we will see different theoretical methods for computing the conductance and permeability of a channel and their application to our models. All our models are biological environments composed by a Connexin 26 connexon embedded into a POPC membrane and inserted into a realistic bath solution composed of water and 150mmol of KCL salt (on both side of the channel) [19, 20]. The aim is to reproduce and understand the experimental results obtained for the conductance and permeability of Cx26 channels and, in particular, describe the differences between wild type (WT) and mutant hemichannels in order to understand the molecular mechanism that lead to the differences. We will see that from simulations we are able to obtain not only an estimate value for these fundamental properties, but also an important insight into the function of connexin channels.

Technical description

Where not explicitly stated, all the molecular dynamics simulation were performed with GROMACS 4.6 software [112] using the Amber14sb force field [113] in the NTP ensemble at 300 K and 1atm, using the Berendsen thermostat and barostat [114]. The system is set in a cubic box with periodic boundary condition and unitary cells around 12×12 nm for the coordinate perpendicular to the axis of the pore, consistent with the channel density measured in a Cx26 gap-junction plaque by atomic force microscopy [25]. Fast smooth

Particle–Mesh Ewald summation [115] is used for long–range electrostatic interactions, with a cut off of 1.0 nm for the direct interactions. The simulation time step is comprised between 1 and 2 fs.

Single point mutations of the Cx26 protein are introduced using the "mutate" tool of the Swiss PDB–Viewer software package [116], starting from an equilibrium configuration of the Cx26WT model published in Refs. [19, 20].

Chapter 3

The Connexin 26 hemichannel model

As mentioned in Chapter 1, the most accurate structural information on connexin channels have been reported for hCx26 junctional channels by Maeda et al. [17], which obtained a structure with resolution of 3.5 Å by X-ray diffraction. This structure was used by Zonta et. al. to build an *in silico* model of connexin 26 hemichannel [19, 20].

The crystal structure of hCx26, accessible in the protein data bank [117], presents domains that are flexible or not well defined, namely the first residue (Metionine 1), the CL (residues 110 to 124) and a short segment of the C-terminus (residues 218-226). In the original work [19], these missing amino acids was added starting from their C^{α}, with positions assigned so as to mimic a random loop for both CL and C-terminus. The coordinates of the Metionine 1 C^{α} were assigned in register with NTH which follows it. All other atoms which were missing from the X-ray model, including hydrogen atoms, were added using the LEAP module of the Amber 9.0 software [113] and Amber03 force field parameters [118].

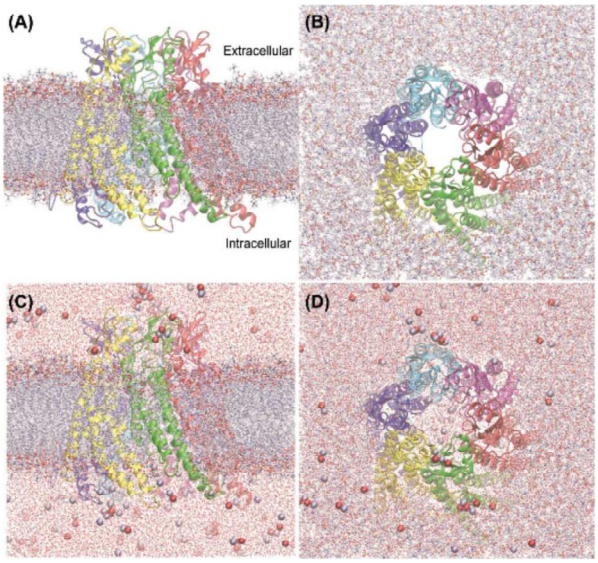

Figure 3.1: hCx26 connexon model in a realistic computational environment [19]. (A, B) The connexon is shown embedded in a phospholipid bilayer. **(C,D)** Also water molecules and ions (shown as colored spheres) were included in the MD simulations, A, C are side views; B, D are views from the extracellular side.

After a small C^{α} restrained MD equilibration in vacuo, the configuration was inserted in a hole opened in a prerelaxed membrane bilayer of phospholipids (palmytol posphatidyl choline, POPC) and all phospholipids in close contact with the protein were removed. The final membrane configuration comprises 493 phospholipids. The positive net charge of the hCx26 connexon was neutralized with 54 chloride ions; additional pairs of potassium and chloride ions were added to mimic a physiological ionic strength. The system was solvated with a total of 39189 water molecules and a brief relaxation run (100 ps) was performed with restrained dynamics on C^{α} and under periodic boundary conditions. The unitary cell dimensions ($\sim 12 \times 12 \times 11\ nm$) approximate the distance between adjacent channels in a gap–junction plaque, as measured by atomic force microscopy [24] (see Figure 3.1).

After that, the system dynamics was followed for 40 ns. To ensure that both MD connexon models achieved a stable steady state, the root mean square deviations (RMSD) was computed as

$$RMSD(v, w) = \sqrt{\frac{1}{n}\sum_{i=1}^{n} \|v_i - w_i\|^2} \tag{3.1}$$

where v and w are two sets of n points that represent the analysed frame and the reference frame, respectively. This variable was analysed from the initial configurations (Figure 3.2) for TM (black traces) and EC domains (grey traces), respectively.

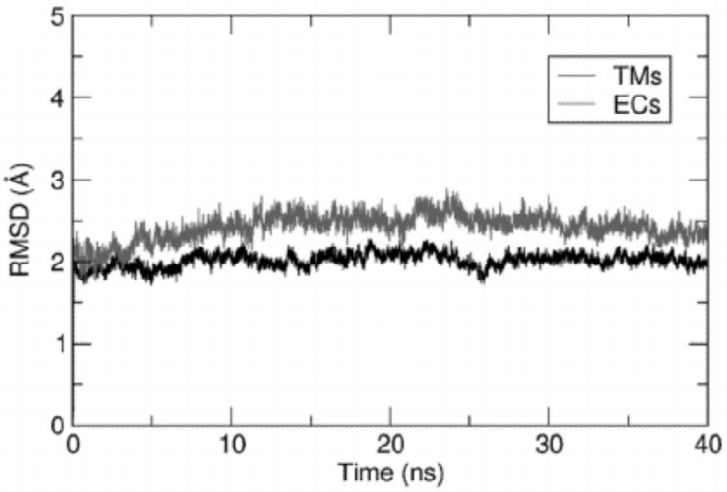

Figure 3.2: Plots of RMDS vs. time during the 40 ns **of equilibrium dynamics [19].** Black traces correspond to residues in the membrane region (residue from 19 to 40, 76 to 96, 132 to 153 and 190 to 210), whereas grey traces correspond to residues in the extracellular space (residue from 41 to 75 and 154 to 189).

After 15 ns, the RMSD remained substantially invariant for both structures, indicating that the models had equilibrated in this relatively short time span. Comparison of the hCx26 X-ray model (Figure 3.3A-C, blue) and the hCx26 MD model (Figure 3.3A-C, red) shows an average deviation of 2.0 Å, well within the resolution limit of the experimental data.

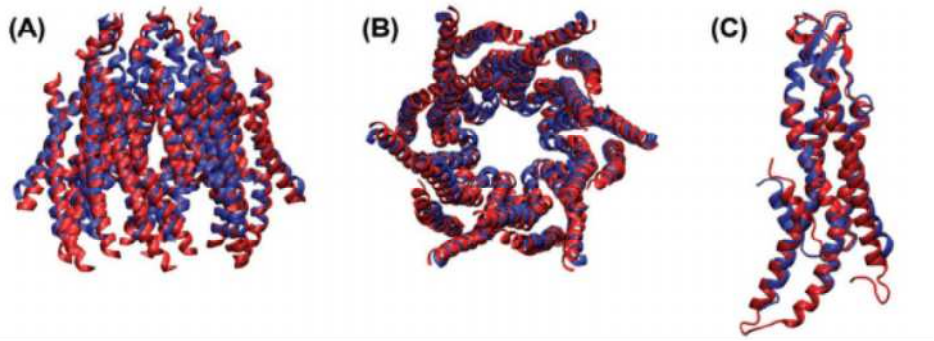

Figure 3.3: Comparison between the hCx26 crystal model and Zonta et. al. molecular dynamics (MD) models in cartoon representation [19]. The hCx26 crystal model is shown in blue and the Cx26 MD model in red. Panels A and B show only the helical regions of the connexons for clarity. Panel A is side views whereas B is views from the cytoplasmic side. Panel C depict single connexin.

3.1 A renewed model

In this Ph.D. project we worked with the connexon model described above. Part of the work consisted in the refinement of this model upgrading it to the last force field available, elongating the equilibrium dynamics to a minimun of 100 ns and remaking all the analysis and data obtained with the old model. In particular, for the last upgrade of the model we used Amber2016 force field, that exhibits considerably better agreement with the Nuclear magnetic resonance (NMR) data [119], and we performed a equilibrium dynamics of 500 ns. As in the previous analysis, to test the stability of the model we compute the RMSD from the initial configurations (Figure 3.4) for TM (black traces) and EC domains (blue traces), respectively.

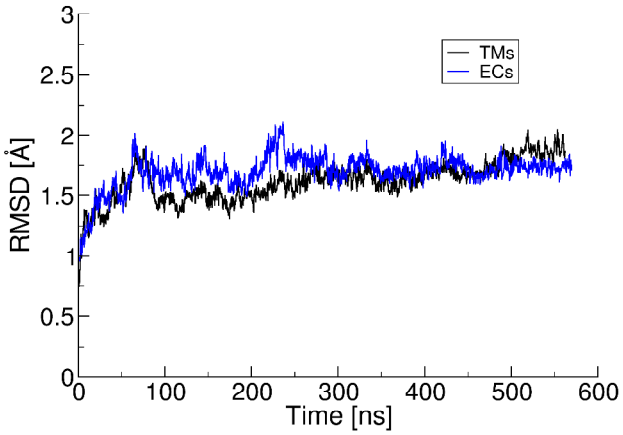

Figure 3.4: Plots of RMDS vs. time during the 500 ns of equilibrium dynamics. Black traces correspond to residues in the membrane region (residue from 19 to 40, 76 to 96, 132 to 153 and 190 to 210), whereas blue traces correspond to residues in the extracellular space (residue from 41 to 75 and 154 to 189)

With a dynamics of 500 ns, we have a broader view of the equilibrium process and we see that, with the new force field, the RMSD reach a steady state after 300 ns. All the model for the mutant connexon that we will study in the following part, are built starting from the Cx26WT model by mutating the amino acids that differ in the two sequences using the Swiss PDB-Viewer, a free software from the Swiss Institute of Bioinformatics [116]. The program allows to browse a rotamer library in order to change amino acids side chains, and to choose the best rotamer according to a score based on steric clashes and putative hydrogen bonds formation.

Chapter 4

Structural analysis of a deafness-related mutant

Performing equilibrium molecular dynamics is essential for the study of a computational model. These dynamics are extremely important in order to allow the system to reach a steady state providing information about the stability of the system for a fixed temperature. These equilibrium molecular dynamics can be achieved using different ensembles, the most commonly used are NPT, where the number of particles is fixed and pressure and temperature are kept constant, and NVT, where the number of particle and the volume of the system are fixed and the temperature is kept constant. There are well known equilibrium variables that can be computed from equilibrium molecular dynamics and are extremly useful for characterizing the behaviour of the system. One of the most used is the RMSD, (already introduced in the previous Chapter (Equation 3.1))) and is essential to understanding the stability of the system or how much the two configurations vary. During the discussion of this thesis, other variables will be introduced that will be used ad hoc for the single problem. All these variables are part of the structural analysis of the studied system and will be used with the aim of characterizing our model and distinguishing two proteins that differ for a single point mutation.

In this Chapter we aim to show the results obtained by a structural analysis performed on equilibrium molecular dynamics for the Cx26 hemichannel WT and C169 mutant. With this structural analysis, the differences that typify the two models and hypothesis on the effect of the mutation will be found.

4.1 The Cx26C169Y mutant

Cystein 169 is located on the EL2 of the connexin 26 and is one of the six extracellular cysteine residues which are conserved in all connexin isoforms. These six cysteines form three disulfide bridges, which are likely to play an important role in guiding the correct folding of the connexin protein and the docking of the two hexameric hemichannels in the extracellular region. In the closely related connexin 32 protein (Cx32), the substitution of Cystein 64, which forms the disulfide bridge with Cystein 168 (the analogous of Cystein 169 in Cx26), with a serine generates a mutant protein that fails to form gap junction channels, even though it is correctly targeted to the cell membrane [120]. Substitution of any one of the six cysteines to serine in Cx32 resulted in loss of channel conductance in paired Xenopus

oocyte experiments [121, 122]. The mutant Cx26C169Y is a single point mutation that substitutes Cysteine (C) in position 169 with a Tyrosine (Y). This mutation, first described by Azaiez et al. [123], provides an example in which the effects of a single point mutation have not been immediately understood. The lack of segregation with a hearing phenotype in some trios and large families prompted its classification as a polymorphism [124]. However, the C169Y allele has been recently singled out in a consanguineous Arabian family from the Middle East; based on the use of in silico predictor tools, C169Y has been assumed as causative [125]. This mutation was not clearly experimentally characterized and with our work we wanted to extend the analysis of this mutation in the attempt to clarify its possible role.

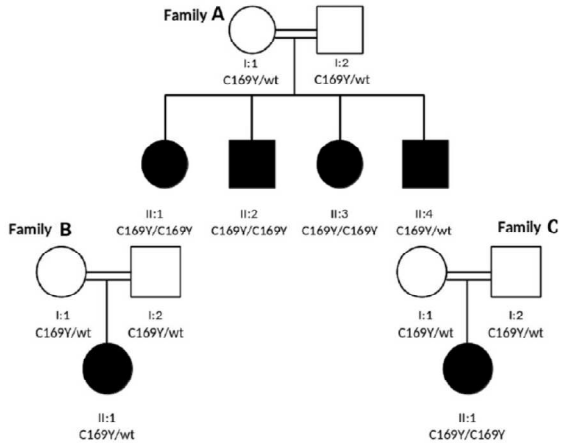

Figure 4.1: Pedigree of the families with indication of the phenotypes and the GJB2 genotypes [22]. Pedigree showing three families with C169Y variants. For Family **a**, affected individuals are: II:1 (C169Y/C169Y), II:2 (C169Y/C169Y) II:3 (C169Y/C169Y) and II:4; (C169Y/wt); Family **b**: the proband is II:1 (C169Y/wt); Family **c**: the proband is II:1 (C169Y/C169Y). Note: (C169Y/C169Y), homozygous; (C169Y/wt), heterozygous; wt, wild-type.

We started our analysis building the Cx26C169Y model starting from the Cx26WT as we explained in Chapter 3. For both Cx26WT and Cx26C169Y models, the entire system comprised $> 2 \times 10^5$ atoms and was equilibrated by a 100 ns molecular dynamics simulation in the NPT ensemble.

In the extracellular region of the Cx26WT protein, Cysteine 169 forms a (strong covalent) disulfide bond with Cysteine 64, which keeps the distance between the two sulfur atoms at 2.05 Å. In the Cx26C169Y protein, the C169Y substitution makes the formation of this bond impossible and produces an alteration in the distance between residues 64 and 169 (Figure 4.2).

The distance between the α carbons of these residues, averaged over the six connexin subunits of the connexon, was derived from 100 ns of equilibrium molecular dynamics and plotted as a function time in Figure 4.3 (left). Figure 4.3 (right) shows frequency histograms of distance distributions for the wild-type and the mutant connexon. The C169Y substitution modifies the mean value and the variance of these distributions, from 5.9 $\pm$ 0.2 Å for the wild-type to 6.6 $\pm$ 0.1 Å for the mutant. Although small, this difference is statistically significant ($P < 0.0001$, Student's t-test) and alters the structure of the hemichannel in the extracellular region (particularly the E2 loop). Visual inspection

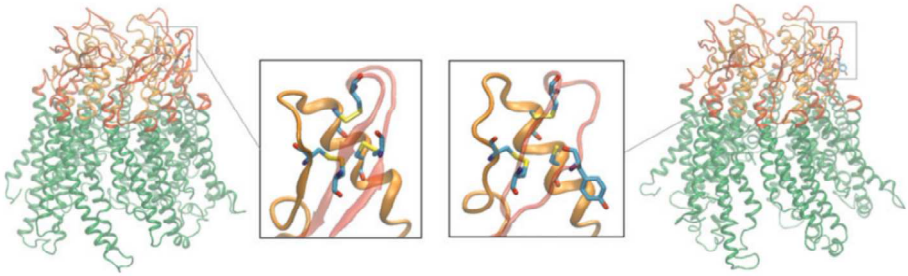

Figure 4.2: Cartoon representation of Cx26WT (left) and Cx26C169Y (right) hemichannels [22]. The six connexins composing the hemichannels are drawn in ribbon; the extracellular loops (EC1 and EC2) are shown in orange and red (respectively). **The insets** show details of a single connexin; residues $53-180$, $60-174$ and $64-169$, which in the wild-type structure are linked by disulfide bonds, are drawn in licorice representation.

of the molecular dynamics trajectories revealed a remarkable deformation affecting two of the proteins of the hexameric assembly. Albeit less pronounced, deformations were detectable also in the remaining four connexins.

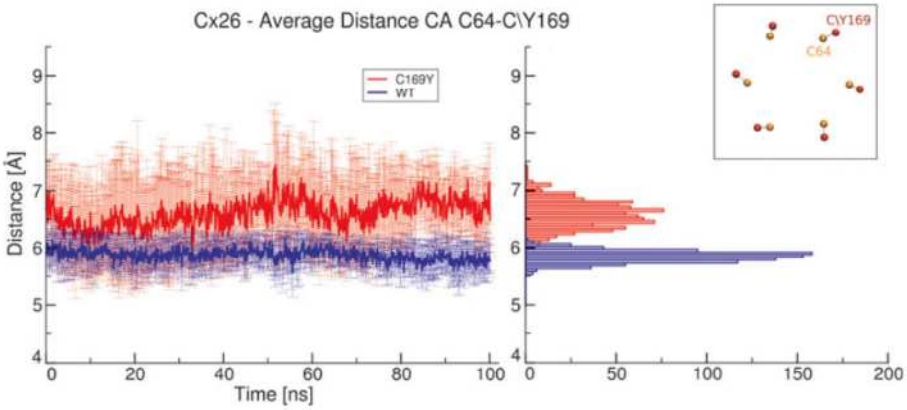

Figure 4.3: Distance between residues 64 and 169 during molecular dynamics simulation [22]. The graph on the **left** shows average distances between α carbons of the two residues **(inset)** for the Cx26WT hemichannel (blue) and the Cx26C169Y hemichannel (red) as a function of time. Frequency histograms for the distribution of distance values are presented in the right panel. The absence of the disulfide bridge in the mutant results in a broader distribution, which is also shifted toward larger values.

To keep track of this diversity, we analyzed the trajectory of each protomer independently. We started this analysis clustering the trajectory of the six connexins. Clustering atomic configurations using suitable metrics is a consolidated technique used to analyze long molecular dynamics trajectory and reduce data complexity while retaining the relevant information [126]. The clusters were obtained with the g_cluster tool of GROMACS 4.6 by restricting the analysis to the two extracellular loops (residues $41-75$ and $155-192$) of the six different connexins. Each cluster contained all the configurations for which the RMSD of the corresponding main-chain atoms was ≤ 1.1 Å. For the Cx26C169Y

model, the single most important cluster contained 69.8% of the MD trajectory. For the Cx26WT model, instead, we obtained two principal clusters representing 46.0 and 17.0% of the configurations, respectively. From these most important clusters of Cx26WT and Cx26V84L, we selected one configuration for the mutant and two configurations for the wild-type as the most representative of their respective trajectories (the mean values of the observables reported for Cx26WT are weighted averages of these two clusters, with weights proportional to the percentage of trajectory covered). Then we computed the RMSD (Equation 3.1) of the atoms in the main chain of the seven residues (Asparagine 54, Leucine 56, Glutamine 57, Lysine 168, Asparagine 176, Threonine 177, Aspartate 179) that are considered responsible for the extracellular docking of the two connexons [17], taking the corresponding coordinates of the 3.5 Å X-ray crystallographic structure as reference. Compared with Cx26WT, the positions of these crucial residues in Cx26C169Y depart significantly more from those taken as reference (Fig. 4.4). The difference is caused by the displacement of the E2 loop in three of the six connexins. Indeed, if we concentrate only on residues Asparagine 176 and Threonine 177, it is clear that the RMSD in three of the six mutant connexin exceeds 2.5 Å (Figure 4.4, red diamonds), whereas the maximum RMSD in the wild-type is ∼1.5 Å (Figure 4.4, blue squares). We conclude suggesting that such departure from the crystallographic positions hinders the correct docking of the connexons and prevents the formation of a full gap junction channel.

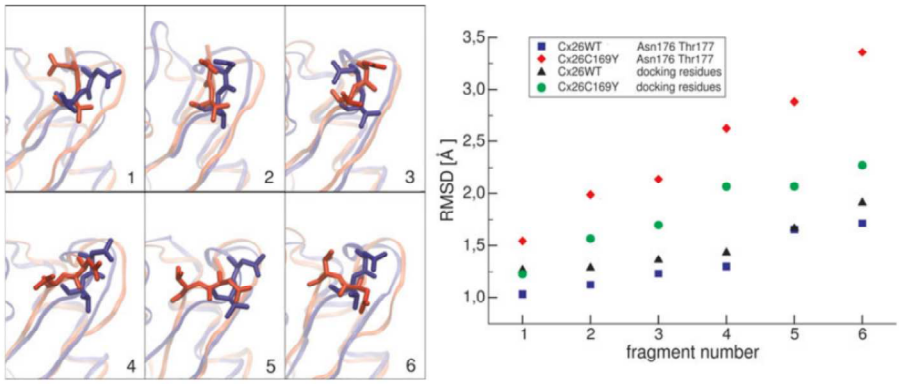

Figure 4.4: The C169Y mutation of Cx26 perturbs also residues that are considered critical for hemichannel docking and formation of a full gap junction channel [22]. The **six left panels** show the orientation of side chains of residues Asparagine 176 and Thr177 in the six connexins of the most representative confiurations of wild-type (blue) and mutant (red) hemichannels. Structural alteration in the extracellular loop due to the absence of one of the disulfie bridges alters the position of the side chains of these two critical residues in the mutant hemichannel, which are thought to be responsible of the formation a full gap junction channel. The six panels are ranked in order of increasing RMSD of α carbons of Asn176 and Thr177 from the crystal structure of [17]. The RMSD values for these two residues are reported in the graph of the **right** (blue squares for Cx26WT, red diamonds for Cx26C169Y), together with those of all the seven residues that have been identifid as responsible for the docking in [17] Asparagine 54, Leucine 56, Glutamine 57, Lysine 168, Asparagine 176, Threonine 177, Aspartate 179 (black triangles for Cx26WT, green circles for Cx26C169Y). The positions of residues Asparagine 176 and Threonine 177 are the most affected by the mutation.

To verify this hypothesis, we transiently transfected Hela DH cells with either wild-type or mutant constructs and performed immunostaining with antibodies against Cx26 (Figure 4.5). In cells overexpressing Cx26WT proteins, gap junction plaques were seen at points of cell-to-cell contact, with limited intracellular staining. In contrast, in HeLaDH cells overexpressing mutant Cx26C169Y proteins, the immunofluorescence signal exhibited a predominantly diffuse and cytoplasmic localization, with limited staining at the plasma membrane level. The analysis of confocal through-focus image sequences (z-stacks) highlighted the presence of mature junctional plaques connecting adjacent cells in the Cx26WT transfectants (Fig.2A–D). Plaques were not observed in the mutant transfectants (Fig. 2F–I). Altogether, these results suggest that a (fraction of the) Cx26C169Y hemichannels are correctly targeted to the plasma membrane, but fail to dock to each other in neighboring cells, thus preventing the formation of gap junction channels.

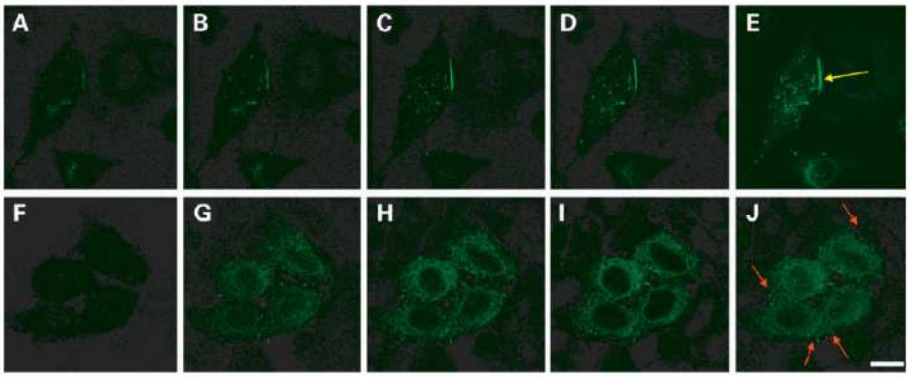

Figure 4.5: Cx26 immunostaining performed in Hela DH transfectants overexpressing Cx26WT (top), and Cx26C169Y (bottom) proteins [22]. Through focus confocal image sequence (z-stack) taken at 0.5 µm intervals of Hela DH cells expressing Cx26WT **(A-D)** and Cx26C169Y **(F-I)** proteins and their respective maximal projection rendering (**E** and **J**). Yellow arrow points to representative gap junction plaque, whereas red arrows indicate immunoreaction signals at the cell plasma membrane level, which are most likely due to unpaired connexons. Scale bar, 10 µm.

4.1.1 Comments

By the structural analysis of the equilibrium molecular dynamics we were able to predict that C169Y mutation hinders the docking of Cx26 hemichannels by altering protein structure in the extracellular domain. In particular, we predicted a significant displacement of two of the seven amino acids that are responsible for hemichannel docking, namely Asparagine 176 and Threonine 177. It is worth noting that this alteration is not identical in all six connexins making up this hemichannel (Figure 4.4) and, in some of the protomers, the structure remains virtually unaltered. We suspect that this discrepancy is due to the relative shortness of the simulated time span, and that a longer simulation would lead to similar configurations in all six connexins. For this reason, although a 100 ns molecular dynamics simulation is sufficient to re-equilibrate a protein structure in the proximity of a local energy minimum, detecting a structural rearrangement may require a longer simulation interval. Nonetheless, our results strongly suggest the extracellular

domain of Cx26 is compromised of the C169Y mutation. We were able to perform an experiment that corroborated the hypothesis proposed on the results obtained by molecular dynamics. Indeed our experimental data, based on immunofluorescence of the connexin proteins in HeLa DH cell transfectants (Figure 3.1), strongly suggests that the mutated protein is correctly trafficked to the plasma membrane but fails to form gap-junction plaques, confirming that the extracellular cysteine pattern is fundamental for the docking of opposing hemichannels.

Chapter 5

Conductance

Any electrophysiological analysis of the conduction process involves the application of Ohm's law. Precisely how Ohm's law is applied depends on the physical configuration of the channel, particularly as regards the composition of the bath solutions (Figure 5.1).

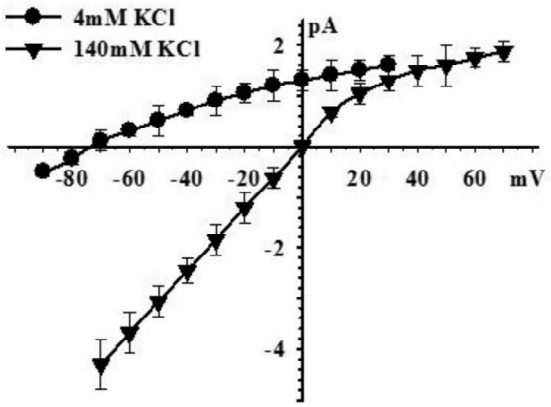

Figure 5.1: I-V curves [127]. Mean current-voltage relations for inside-out patches of Huh7ins cells exposed to an external K+ concentration of either 140 mM or 5 mM K+ (n = 6). Values represent means ± standard error mean.

We consider the bath solutions to contain identical KCl concentrations on both side of the membrane (that will be the configuration of our simulated systems) so that the only driving force for ion flow is the transmembrane electrical potential, V_m , and current flow through the open channel is described by the equation

$$I = ZV_m \tag{5.1}$$

where I is the total current flow through the channel in units of amperes ($1\,\mathrm{A} = 1\,\mathrm{C/s}$), V_m is the transmembrane electrical potential in volts, and Z is the single-channel conductance in units of Siemens ($1\,\mathrm{S} = 1\,\mathrm{A/V}$). The definition of Z is completely independent of the ion that is the actual charge carrier. The operational definition of Z is based solely on the movement of charge, and this distinguishes conductance from permeability, for which the definition is more likely to be based on the behaviour of a specific ion. By measuring I at different values of V we obtain the current-voltage relation ($I - V$ plot) for the channel,

which is the basis for the operational definition of the single-channel conductance. The definition of Z is most unambiguous when the $I - V$ plot can be described by a straight line, for which Z is the slope. Clearly, Z is a measure of how readily ions move through the channel and as such, is a concise summary of all of the physical processes involved in the entry of an ion into the channel from the aqueous solution, the translocation of the ion through the channel and the exit on the other side. One motivation for analysing the physical basis for ion conduction is the desire to use ions as probes that, by virtue of their conduction rate, reflect the properties of the pore; properties that can be modified, for example, by substituting one amino acid residue for another. This means that a channel made of mutant proteins can be distinguished by their conductance that becomes one of the fundamental properties characterizing mutant channels. It is useful at this point to consider the form of 5.1. The fact that I is zero when V is zero is most important. This is an expression of the fact that the channel is a purely dissipative or permissive element; current only flows in the presence of an applied driving force, in this case a voltage. The form of Eq. 5.1 should not be taken to indicate that the current-voltage relations of channels are expected to be linear, however. The current-voltage relation can be decidedly nonlinear even under symmetric ionic conditions, despite the fact that it is a thermodynamic necessity that the plot passes through the point $i = 0$, $V = O$ (on our simulated system we do not have different ions concentration between the two side of the connexon). For the time being we define Z as the slope of the $I - V$ plot at any point. Having done this we must contend with the fact that Z can be strongly voltage dependent, and we shall see that there are a variety of ways in which this can come about. It is important, however, that this phenomenon be clearly distinguished from voltage-dependent macroscopic conductance that can arise from voltage-dependent channel gating, i.e., a change in the probability of finding the channel in the open state. Here we generally refer to the conduction properties of a channel in a specific state ([111]).

In the following Sections we see different Molecular Dynamics methods for computing the conductance of a membrane channel. After every theoretical explanation, the applications of that method to our models is presented. In particular our models will be gap-junction membrane hemichannels made by Connexin 26 Wild Type and mutants based on the full-atoms model of Zonta et al. [19–21] we presented in the Section 3.

5.1 "Brute force" conductance calculation

From a computational point of view, it is possible, in principle, to compute the conductance of a hemichannel by imposing an electric potential difference (V) between the two side of the membrane and counting the number of ions that pass through the hemichannel. We will call this the *brute force method*. Each ion in our system have charge $\rho_i = \pm e$ ($+e$ for K^+ ions and $-e$ for Cl^- ions) and contributes to the current (I) that passes through the hemichannel in a fixed simulation time. Once we have the current and the electric potential difference, the conductance of the channel can be simply defined by

$$Z_{HC} = \frac{I}{V} = \frac{\sum_i n_i rho_i/\tau}{V} \tag{5.2}$$

where the label i indicate the atom type that contributes to the current and n_i is the number of ions with charge rho_i that pass through the pore in a simulation time τ.

In order to apply this method to a system like the membrane channel we are studying (with $>2 \times 10^5$ atoms), is necessary to set up a simulation with a strong electric potential difference or running it for a very long time. Indeed in the time-scale of 100 ns and with electric potential difference comparable with the one used in the experiment (around -90 mV on the membrane), we do not expect the passage of more than 10 ions.

The best way to impose an electric potential difference in a molecular dynamics simulation is to set a constant electric field across the whole system. As discussed in Ref. [128], the presence of a potential difference across a membrane unavoidably breaks periodicity. Nevertheless, the equivalence of the forces arising from the constant applied electric field across the boundary ensures that there is no discontinuity in the force acting on a given particle when crossing it. The net result of a particle crossing the periodic boundary is akin to passing through a virtual circuit with an embedded electromotive force (EMF), i.e., a battery [129]. This virtual EMF provides the work that gives rise to the bulk phase polarization (and slight charge imbalance if there are mobile ions) across the simulation cell, which causes the potential difference. To understand how the membrane potential difference relates to the periodic boundaries, it is helpful to observe how it is realized in various systems. As visualized in 5.2, a constant applied electric field generates a linear potential across the entire unit cell. However, what matters is the total potential difference across the membrane, which is the parameter we need to compute the conductance of our channel. A uniform medium such as an aqueous salt solution will naturally self organize to reduce as much as possible the magnitude of any net average electric field. This behaviour is akin to good conductors that expel all electric fields from their interior. The rearrangement of the bulk medium to a non-uniform distribution generates its own reaction field that, when summed with the external field, gives the resulting, total field. Because the change in potential must take place somewhere within the system, it becomes naturally concentrated at an immobile insulating membrane, regardless of its shape or size, with a characteristic decay away from it. Despite the non-periodicity of the total potential, the force experienced by a charged atom across the periodic boundary (computed from the first derivative of the total potential) is continuous [128].

Now we can examine the rate of ion permeation through the pore considering any atomic charge movement in the microscopic system associated with a detectable current going through the virtual EMF circuit [129]. It follows that the steady-state ionic flux through this model under an applied voltage can be calculated from the total displacement current [130],

$$I(t) = \frac{1}{L_z} \sum_{ions} q_i \dot{z}_i(t) \tag{5.3}$$

where $\dot{z}_i(t)$ is the velocity of particle i in the z-direction. Alternatively, it is possible to consider the integrated form of Eq. 5.3,

$$Q(t) = \frac{1}{L_z} \sum_{ions} q_i [z_i(t) - z_i(0)] \tag{5.4}$$

where $z_i(t)$ represent the continuous "unwrapped" coordinates of the atoms, i.e., not folded back into the periodic box. The average current, $I(t)$, can then be evaluated as the limiting value of $Q(t)/t$ as $t \to \infty$ [128, 129]. From this definition of the current, we can simply compute the conductance of the hemichannel with the Eq. 5.2. In the following

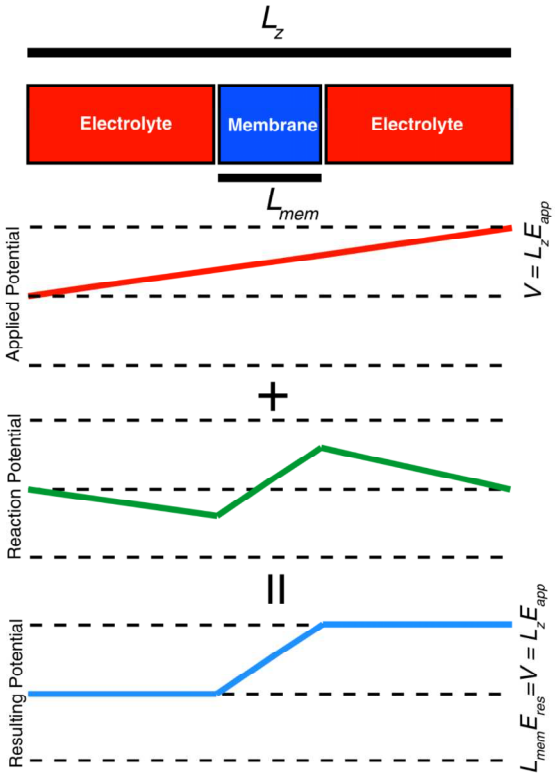

Figure 5.2: Schematic description of the constant electric field methodology. In the periodic system, the applied constant field is associated with a linear potential, which is combined with the reaction potential from the electrostatic forces treated via particle mech Ewald (PME) to generate the resulting total potential. Even though the total electrostatic potential is non-periodic, the reaction potential computed during the simulation (PME), as well as the forces (slope of curces) from both the applied and total potential are compatible with periodic boundary conditions [128].

Subsections we will present our results obtained applying this brute force method on two different models of a hCx26 hemichannel. Due to the time cost of the simulations, we applied this method using a single constant electric field value. This means that we do not have control on the dependence of Z_{HC} from the membrane potential V(we will speak more about this problem in the following Comments).

5.1.1 Application: the antibody abEC1.1

As a first example of the brute force method explained above, we show simulations done in the contest of a collaboration with ShanghaiTech University[1]. In these simulations we compute the conductance of a Connexin 26 Wild Type (Cx26WT) gap-junction hemichannel with and without the abEC1.1 antibody. This is a human antibody that binds the first extracellular loop of connexin 26 and perturbs hemichannel function. The antibody crystal structure has been determined and its mechanism of action has been identified (article under review [131]). For a better understanding of the results, first we will briefly introduce

[1]Shanghai Institute for Advanced Immunological Studies (SIAIS), ShanghaiTech University, Shanghai 201210, China

the structure of the antibodies.

Antibody structure. An antibody (Ab), also known as an immunoglobulin (Ig), is a molecule having a molecular weight of approximately 150 kDa, composed of two different kinds of polypeptide chain. One, of approximately 50 kDa, is termed the *heavy* or *H chain*, and the other, of 25 kDa, is termed the *light* or *L chain* (Figure 5.3). Each Ab molecule consists of two heavy chains and two light chains. The two heavy chains are linked by disulfide bonds and each heavy chain is linked to a light chain by an other disulfide bond. In any given immunoglobulin molecule, the two heavy chains and the two light chains are identical, providing two identical antigen-binding sites [132] (Figure 5.3). Each of the four chains has a *variable (V) region* at its amino terminus, which contributes to the antigen-binding site, and a *constant (C) region*, which determines the isotype. The isotype of the heavy chain determines the functional properties of the antibody. The variable region is further subdivided into *hypervariable (HV)* and *framework (FR) regions*. Hypervariable regions have a high ratio of different amino acids in a given position, relative to the most common amino acid in that position. Within both light and heavy chains, three hypervariable regions exist (HV 1, 2 and 3). Four FR regions which have more stable amino acids sequences separate the HV regions. The HV regions directly contact a portion of the antigen's surface. For this reason, HV regions are also sometimes referred to as *complementarity determining regions*, or *CDRs*. The FR regions form a beta-sheet structure which serves as a scaffold to hold the HV regions in position to the contact antigen [133]. The light chains are bound to the heavy chains by many noncovalent interactions and by disulfide bonds, and the V regions of the heavy and light chains pair in each arm of the Y to generate the two identical antigen-binding sites, which lie at the tips of the arms of the Y. The possession of two antigen-binding sites allows antibody molecules to cross-link antigens and to bind them much more stably. The trunk of the Y, or *Fc fragment*, is composed of the carboxy-terminal domains of the heavy chains. Joining the arms of the Y to the trunk are the flexible hinge regions. The Fc fragment and hinge regions differ in antibodies of different isotypes, thus determining their functional properties. However, the overall organization of the domains is similar in all isotypes [132].
Single-chain variable fragment (scFv) (see Figure 5.3) is a fusion protein of the variable regions of the heavy (V_H) and light chains (V_L) of immunoglobulins, connected with a short linker peptide of ten to about 25 amino acids [134]. The linker is usually rich in glycine for flexibility, as well as serine or threonine for solubility, and can either connect the N-terminus of the V_H with the C-terminus of the V_L, or vice versa. This protein retains the specificity of the original immunoglobulin, despite removal of the constant regions and the introduction of the linker [135].

Experimental results

In SIAIS (ShanghaiTech University) an antibody interacting with EL loop of Cx26, was identified by screening of a scFv combinatorial antibody library expressed in phage. With about 10^{11} unique members, this chemically synthesized immune system is about three orders of magnitude larger than the antibody repertoire in any individual [137].

Based on the crystal structure of hCx26 gap junction channels [17] and the related molecular dynamics models of hCx26 hemichannels [19–22], a hCx26 bait peptide corresponding

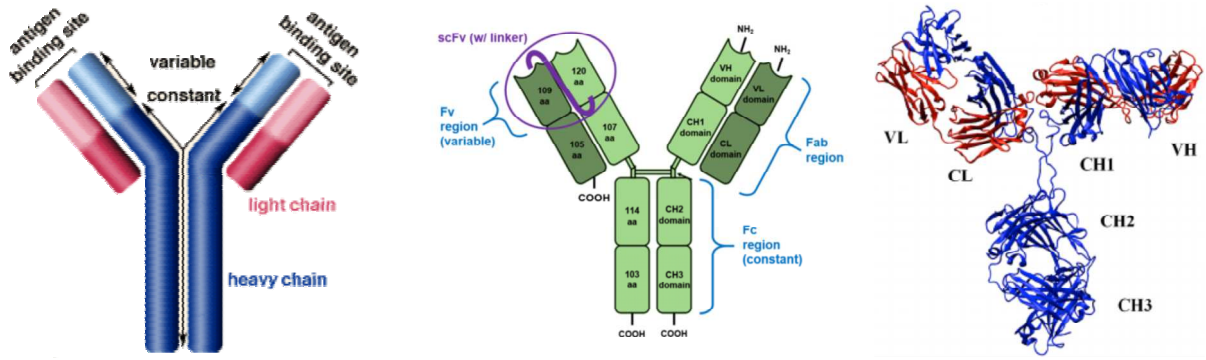

(a) [133]. **(b)** **(c)** [136].

Figure 5.3: Antibody basic structure.

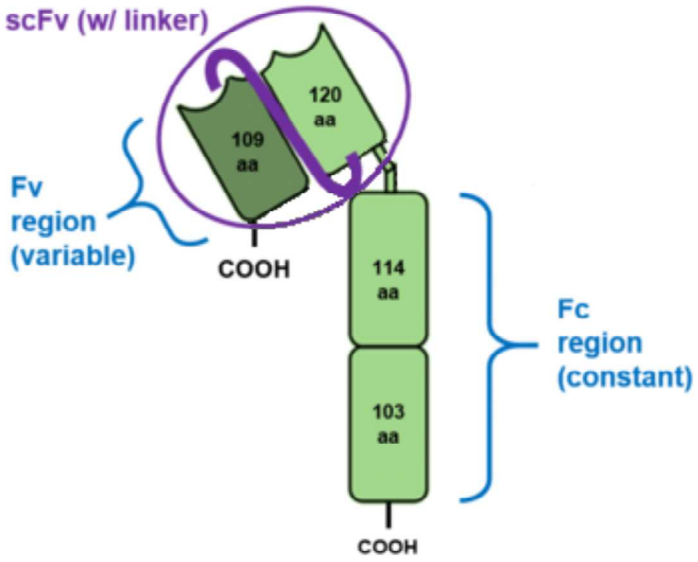

Figure 5.4: Structure of abEC1.1.

to residues 41 to 56 of EC1 (pepEC1.1, Figure 5.5), was synthesized. This peptide was used as an antigen to screen a combinatorial human antibody library expressed in phage [138]. After 2 rounds of panning, an increased enzyme-linked immunosorbent assay (ELISA) signal was observed for pepEC1.1 group compared to the control group (bovine serum albumin, BSA); the scFvs which specifically bound pepEC1.1 were enriched after 4 rounds of panning. 700 phage-infected clones were picked randomly from the third and fourth round of panning and tested for their ability to bind the peptide using phage ELISA. 150 phage clones were selected from the original 700 clones as positive binders ($peptide/control > 2$). Positive colonies were sequenced, complementarity determining region 3 (CDR3) were aligned and a phylogenetic tree was constructed. Based on the analysis of the phylogenetic tree, 3 different scFv sequences were converted into a scFv-Fc format [139] comprising the entire Fc region of human immunoglobulin G1 (IgG1). The binding affinity of these scFv-Fc recombinant antibodies for pepEC1.1 was quantified using surface plasmon resonance. The most promising scFv-Fc candidate, which has been named abEC1.1, was finally selected based on the analysis of the SPR kinetic data set (Figure 5.6A). The computed

ELISA results confirmed that abEC1.1 binds pepEC1.1 but fails to recognize a negative control peptide (Figure 5.6B). Western blot analysis of hCx26 protein purified from a Sf9 expression system showed a band between 25 kDa and 32 kDa (Figure 5.6C, left). Likewise, total cellular proteins obtained from HeLa DH transfectants expressing hCx26–Venus (a chimeric protein formed by hCx26 fused at its C-terminal end to the green fluorescent protein color mutant Venus; [14]) showed a band between 46 kDa and 58 kDa (Figure 5.6C, right), in agreement with the expected molecular weight of hCx26–Venus (52 kDa). Finally, considering abEC1.1 a promising candidate, we solved the crystal structures of its scFv domain. To determine whether abEC1.1 recognizes also hCx26 proteins assembled in a connexin hemichannel, confocal immunofluorescence microscopy was used on HeLa DH transfectants expressing hCx26–Venus. For these experiments, cells were fixed but not permeabilized and abEC1.1 was revealed by a secondary antibody directed to its Fc domain. Image analysis showed abEC1.1 immunoreactivity at the plasma membrane level in the form of punctuate staining, consistent with the western blot results (Figure 5.6C, right). The signal detected under identical immunostaining conditions from untransfected HeLa DH parental cells was considerably weaker and more diffuse. Conductance was not affected by application of an isotype control antibody (Figure 5.8A, black trace) that failed to bind pepEC1.1 and showed no immunoreactivity to HeLa DH transfectants expressing hCx26–Venus. These results suggest that abEC1.1 binds and blocks hCx26 plasma membrane hemichannels open at rest. Consistent with this conclusion, hemichannel currents elicited by a voltage clamp protocol in $0.2mM$ extracellular Ca^{2+} conditions were dramatically reduced after 15 min of abEC1.1 application (952 nM) through the puff pipette (Figure 5.8B).

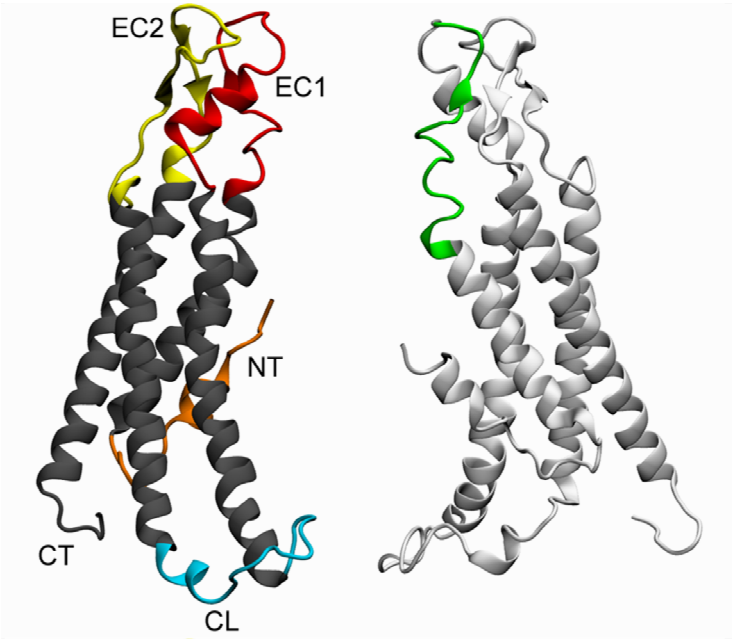

Figure 5.5: hCx26 structure. hCx26 topology representation: NT, N-terminus; CT, C-terminus; CL, cytoplasmic loop connecting transmembrane helix 2 (TM2) to TM3; EC1, EC2, extracellular loops connecting TM1 to TM2 and TM3 to TM4, respectively. The peptide sequence used as bait for the antibody discovery process (pepEC1.1) was derived from the EC1 segment colored in green.

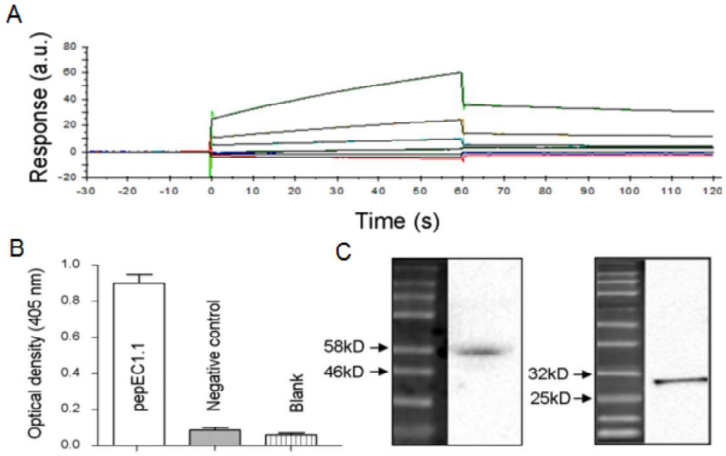

Figure 5.6: Selection of antibodies in phage. A) Kinetic characterization of the interactions between pepEC1.1 and abEC1.1; pepEC1.1 at different concentrations (0, 1.25, 2.5, 5, 10, 20, 40, 80 and 160 nM) was measured against immobilized abEC1.1 using surface plasmon resonance. The data set (blue traces) was fitted to a $2:1$ binding model (red traces) to estimate $k_{ON} = 5.79 \pm 10^4\ M^{-1}s^{-1}$ $k_{OFF} = 4.222 \pm 10^{-3}\ s^{-1}$ and $K_D = k_{OFF}/k_{ON} = 73\ nM$. **B-C**) Biochemical characterization of the selected antibody; after purification, the binding specificity of abEC1.1 was tested (**B**) by ELISA, against pepEC1.1 and (**C**) by western blot, against hCx26 proteins purified from a Sf9 expression system (left) or from proteins obtained from HeLa DH transfectants expressing hCx26–Venus (right). The negative control peptide in (**B**) corresponds to residues 172 to 184 of hCx26 (sequence: *AWPCPNTVDCFVSR*), which form part of EC2.

The selected antibody does not appear to be toxic to cells but reversibly inhibits hCx26 hemichannel currents as efficiently as Zn^{2+}, a non-specific connexin hemichannel blocker ([140, 141]) and strongly reduces the activity of gain-of-function hCx26 mutants implicated in KID/HID (unpublished data [131]). To answer the critical question whether abEC1.1 interferes with hCx26 hemichannel function, we conducted whole cell patch clamp recordings in HeLa DH transfectants expressing hCx26-Venus. Experiments were performed in low extracellular Ca^{2+} conditions (0.2 mM) that bias connexin hemichannels towards the open state (5.8) ([29, 142–144]). Upon delivery of abEC1.1 (952 nM) through a puff pipette, the whole cell membrane conductance of HeLa DH transfectants (Figure 5.8A, green trace) was significantly reduced to $40\% \pm 20\%$ of its initial value within 8 min ($P < 0.05$, $n = 3$).

Computational analysis

The atomistic model of scFV domain (Figure 5.7), derived from the crystal structure, was docked to the extracellular domain of our published model of hCx26 hemichannel embedded in the plasma membrane [19] using the ClusPro 2.0 server [145], and the antibody docking mode [146]. Since the antibody was experimentally characterized to block the hemichannel docking in the extracellular region of the hemichannel (it was proved that the normal behaviour of the hemichannels can be re-established after a washout with normal extracellular solution), among the ∼50 docking configuration generated by the software, we discarded all the configurations in which the antibody faced the Trans Membrane helices,

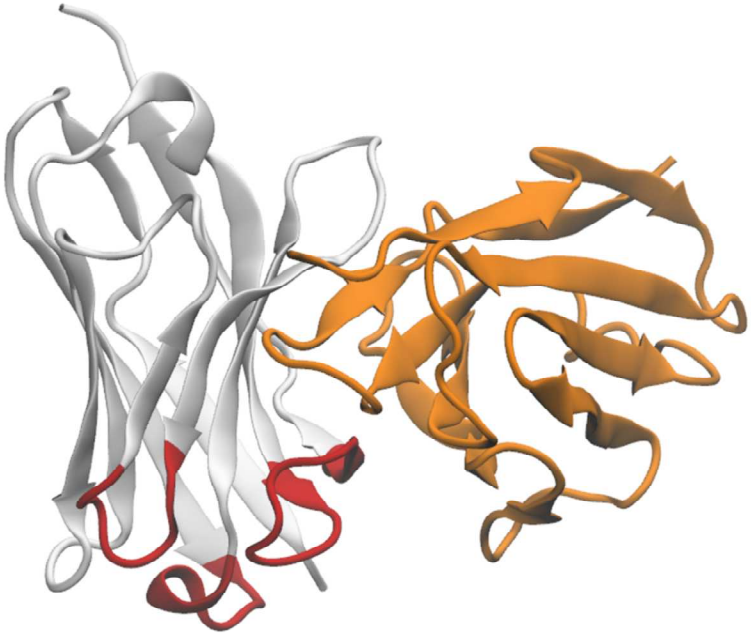

Figure 5.7: Crystal structure of abEC1.1 scFv domain determined by X-ray scattering. Gray, heavy chain; orange, light chain; red, complementarity determining regions in the Heavy Chain (from left to right: CRD1, CDR2, CDR3).

or the cytoplasmic mouth of the pore. Moreover we discarded all the configurations where the CDRs of the abEC1.1 heavy chains were not facing the EC1 loop of hCx26 (Figure 5.9a-c) obtaining only one configuration that met these requirements (Figure 5.9d).

After solvation, the total number of atoms was around 253000. We then performed an equilibrium molecular dynamics for 20 ns. This time window proved to be sufficient to reach a stable conformation for the mutual position of the antibody and the hemichannel and to single out amino acids critically involved in their mutual interaction (Figure 5.7 and 5.10). To corroborate the importance of the amino acids involved in the mutual interaction, we synthesized mutant antibodies where these amino acids were modified one by one. Experimental results with these mutants show that these new antibodies were no longer able to dock and they closed the hemichannel according to our model. A single antibody docks on three different protomers of the hexameric hemichannel, therefore we added a second antibody and docked it to the hemichannel in a symmetrical position. We thus obtained a new equilibrated configuration with the exit of the hemichannel pore surmounted by a pair of antibodies. Simulated electrophysiology experiments shown in 5.11 were performed starting from this latter configuration and from another control configuration in which the antibodies were absent. Based on the consideration exposed in the previous Section, we applied an external constant electric field equal to $E_z = 0.0022\,\mathrm{V/nm}$, that corresponds to a membrane potential of $V = E_z L_z = 40\,\mathrm{mV}$ (L_z represents the size of the box in the z direction that is also the electric field direction). We then followed ion dynamics for 150 ns in both configurations, using a constant volume ensamble [128].

With these simulations we determined that with two bound antibodies capping the extracellular mouth of the hCx26 hemichannel, the simulated ionic current passing through the pore was reduced to $42\% \pm 14\%$ of its control value (Figure 5.11) in agreement with

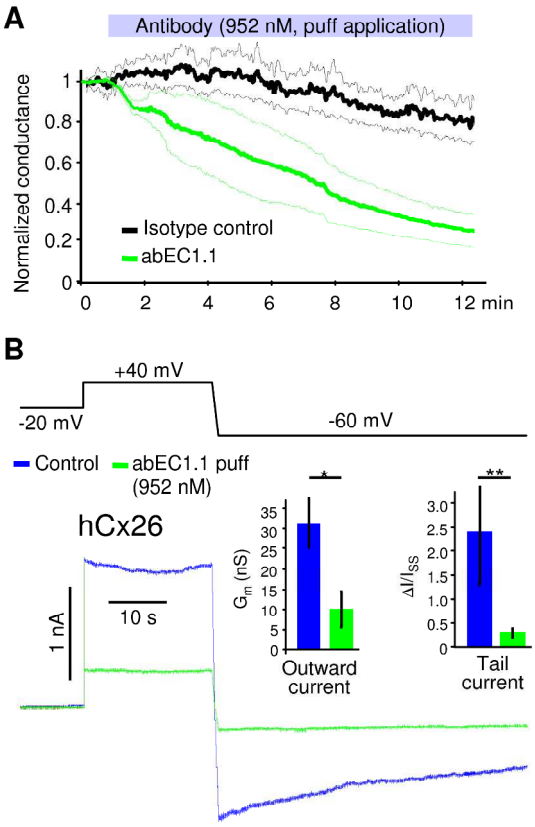

Figure 5.8: The abEC1.1 antibody reversibly blocks hCx26 hemichannel currents in HeLa DH transfectants. A) Membrane conductance, normalized to pre-antibody application levels, vs. time under whole-cell patch clamp conditions (at the cell resting membrane potential); shown are mean values (thick traces) ±s.e.m. (thin traces) for n=3 cells in each data set. B) Representative whole cell currents elicited by shown voltage commands (top, black trace) in a HeLa DH cell expressing hCx26. Histograms show mean values ±s.e.m. for n=6 cells.

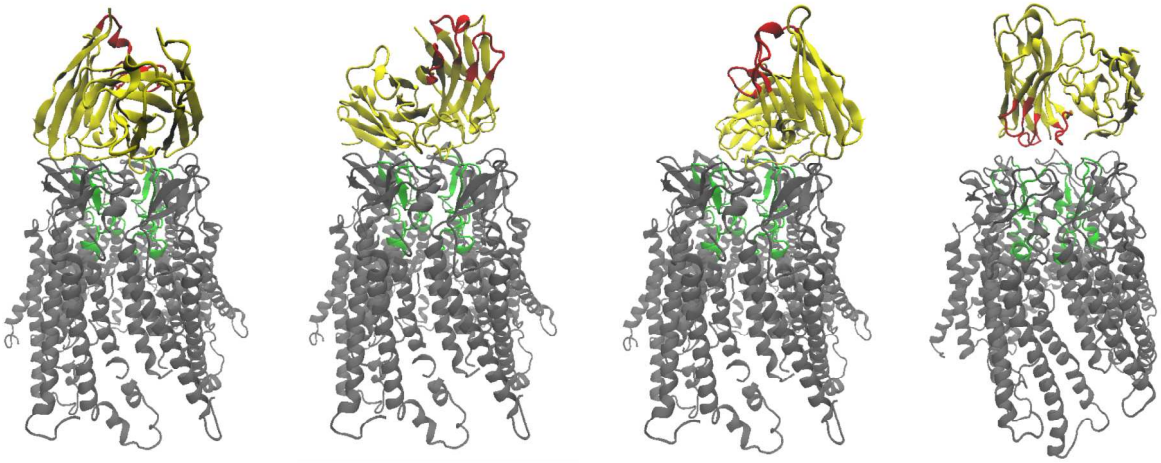

Figure 5.9: Different docking configurations obtained.

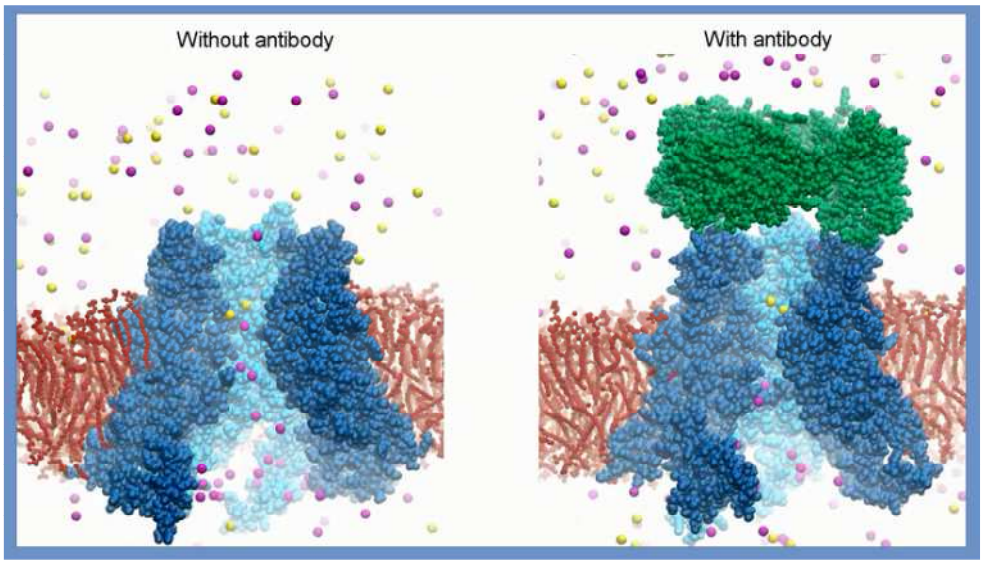

Figure 5.10: Visualization of the Connexin 26 hemichannel system with (right) and with out (left) antibody. In both the image are shown four of the six Connexin of the hemichannel (drown in blue and light blue) embedded by a phospholipid membrane (drown in red) and surrounded by K^+ and CL^- ions (drown in yellow and violet). In the right picture are also present two antibodies docked in the extracellular part of the hemichannel (drown in green).

the experimental results (Figure 5.8).

Our molecular model, based on crystal structure coordinates of both abEC1.1 and hCx26, rationalizes these results indicating that the observed effects are mediated by partial occlusion of the extracellular pore mouth by the concerted action of two bound antibodies. The small residual current that can still be measured in the presence of the antibodies is likely due to the passage of monatomic ions that escape through the imperfect seal at the outer pore mouth.

5.1.2 Comments

Using the brute force method explained in Section 5.1, we computed the ratio of the current flowing through a human Connexin 26 hemichannel with and without the abEC1.1 antibody. Nevertheless, we are not able to produce a quantitative measure of the current flowing through one hemichannel. This is because, although the resulting voltage is independent of the system size and solely depends on $E \cdot L_z$, there are a lot of different factors that lead to systematic errors. In particular non-equilibrium properties are more sensitive to the finite size of the system due to changes in the resistance and long-range dissipative effect. These lead to a clear dependence on the size of the system for the current that flows through a membrane pore. The value found for the currents are qualitatively in good agreement with the experimental results, but we cannot consider these values reliable. Indeed, we know from Ref. [128] that the conductance Z of the hemichannel model computed with this out-of-equilibrium simulations is dependent on the imposed membrane voltage V. Another problem is related to the time-scale of the simulation. For a full atom system with more than 2.5×10^5 atoms, we can reach simulation times of the order of 500 ns. This time-scale is extremely small compared to the record times in the patch clamp

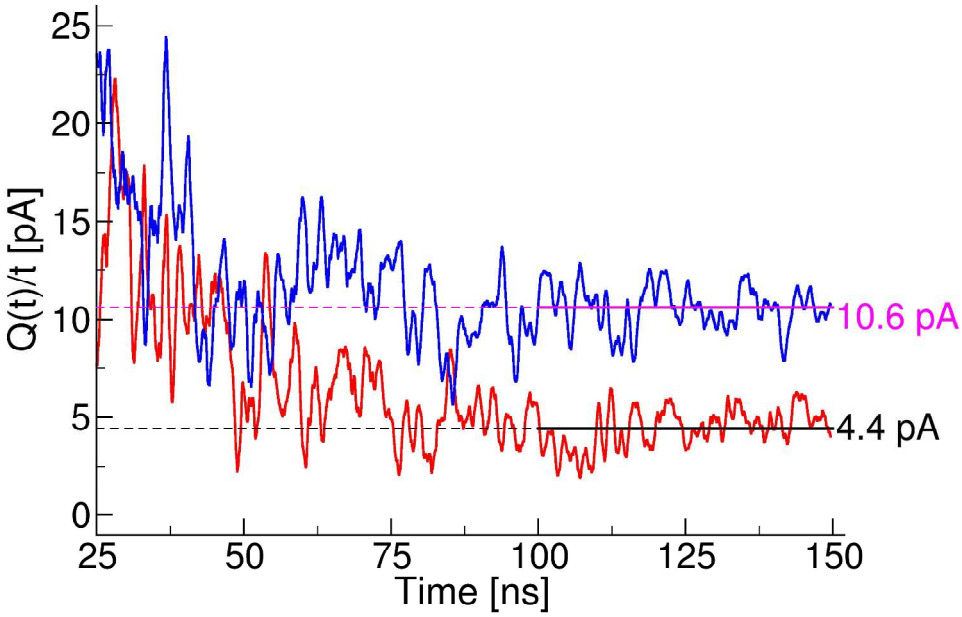

Figure 5.11: Simulated electrophysiology experiments in the presence or absence of abEC1.1 antibodies. The two traces represent the time course of function $\frac{Q(t)}{t} = \frac{1}{t}\left[\frac{1}{L_z}\sum_{ions} q_i[z_i(t) - z_i(0)]\right]$ the limit of which, for $t \to \infty$, is the unitary hemichannel current [128]. The red trace corresponds to the simulation in the presence of antibodies, while the blue trace is computed without them. In each case, the limit (shown in the graph as a orizontal line) was estimated by computing the average of function $Q(t)/t$ over the last 50 ns of the corresponding molecular dynamic simulation, when the function fluctuated around a steady plateau level.

electrophysiology experiments (on the order of ms).). Since the simulation time-scale is closely related with the number of atoms in the system, one possibility for reducing the time-scale problem is based on drastically reducing the number of atoms in our system. As we will see in the next Section, in order to reduce the number of atoms in our system we created a Coarse Grained (CG) model that counts $\sim$ 20000 atoms (1/10 of the full atoms model).

5.1.3 Computing currents using coarse grained model

One of the main unresolved problems in biological science is the time-scale and length-scale gap between computational and experimental methods of studying biological systems. Chemical and mechanical processes on an atomic level form the basis of all phenomena in living systems. However up to now these approaches have been practically limited to simulation times from 100 ns up to 1 µs depending on the number of atoms in the system. A possible way to extend molecular modelling and bridge it with experimental techniques is to use coarse-graining (CG) to represent a system by a reduced (in comparison with an all-atom description) number of degrees of freedom (Figure 5.12). One of the problem in

the AA models, is the huge amount of water molecules that we need in order to solvate the system. The usage of explicit water is essential to obtain a realistic environment, but in general we are not interested in the dynamics of the water particles. The use of CG model allowed to get rid of a big number of atoms (and then the number of degree of freedom) of the system. In particular, the biggest advantage is due to the dramatically reduced number of explicit water molecules in the system. Owing to the reduction in the degrees of freedom and elimination of fine interaction details, the simulation of a coarse-grained system requires less resources and runs faster than that for the same system in all-atom representation. As a result, an increase of orders of magnitude in the simulated time and length scales can be achieved.

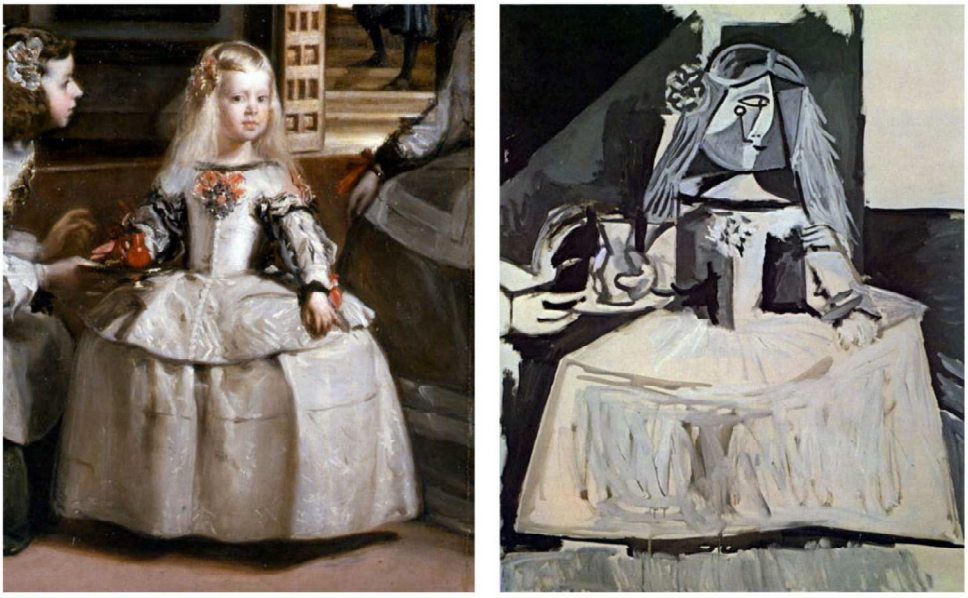

Figure 5.12: Las Meninas (infanta Margarita). These two paintings explain perfectly the concept of Coarse Grained. On the left we have the full of detail original painting of Velazquez that represent the All Atoms model, while on the right we have the Coarse Grained model represented by the Picasso version's of the painting where he got rid of redundant detail but we can still recognise the subject.

During the years, different CG force fields have been developed. The philosophies used to coarse atomistic details can be classified into *bottom-up* and *top-down* approaches. In the first case, interaction parameters for a given molecular representation are developed by fitting to higher level (usually atomistic) simulations. In the top-down approach, parameters are chosen to fit structural or energetic experimental data. In this work we will use *SIRAH* that is a top-down CG generic force field derived to fit structural properties. The force field contains parameters for explicit water, electrolytes, DNA and proteins. Molecular interactions are evaluated using a classical Hamiltonian, which facilitates its implementation in common molecular dynamics packages [147].

Thanks to the collaboration with Professor Sergio Pantano[2], starting from the All Atom (AA) model described in Chapter 3 we created a CG model of the hCx26 hemichannel inserted in a realistic environment made by membrane, water and ions based on the Sirah

[2]institute Pasteur de Montevideo, Montevideo, Uruguay

force field [148].

To validate the CG model, we compared its dynamics with that of the AA model. The results are shown in Figure 5.14, which compares various observables. The CG model is shown in Figure 5.14A (side and top views), whereas panels B and C display the normalized density of non-ionic chemical species (B) and ions (C) as a function of the axial (z) coordinate in (A) and defined as

$$n = \frac{N}{V}$$

where N is the total number of object in the volume V (for a easer visualization, this quantity was normalized to the maximum value). Panel D shows the Root-Mean-Square Deviation (RMSD) defined in Equation 3.1. We computed the RMSD from the initial configuration for the transmembrane (TM) helices and the whole protein complex vs. time (2.5 µs). The inset in panel D compares a 100 ns dynamics for the CG and AA models. Altogether, these data indicate that the overall behaviour of the CG model is comparable to the AA model.

Furthermore, structural characteristics are preserved in the transition to the CG representation. In particular, as shown in Figure 5.15, the pore inner diameter at the level of the six Lys41, which together form an electrical sieve for charged species [19], has the same distribution of values in the CG and AA models (data not published [149]).

After the CG model has been validated, we used it to compute the current flowing through the hemichannel for a time-scale of orders of magnitude higher than the one we reached with the AA model. Since our CG model is composed of $\sim$ 20000 atoms (1/10 of the full atoms model) and we can increase the simulation step up to 20 fs, we are able to reach time-scale of the order of 10 µs. Moreover, using a coarse grained force field is possible that the energy profile of the system became flattened (Figure 5.16) [150]. This means that the minima of the energy profile are easier to reach. Hopefully, since the force field is made to reproduce the real behaver of a biological system, these energy profile minima lead to the same configuration of the system. For this reason we would expect to reach real conformation that we would not be able to see using a AA model.

Similarly to what we have done in the Section 5.1.1, we introduced membrane potential in the form of an electrostatic field in the direction of the pore axis (z direction) and performed molecular dynamics on the CG connexon model over 10 to 15 µs with constant volume conditions. We performed two simulations in which we applied an electric field in the two opposite direction ($+z$ and $-z$) with magnitude 0.03 V/nm, corresponding (for a AA force field) to an estimated membrane potential of $\pm$120 mV, of the same order of magnitude of membrane potential in inner ear supporting cells (up to 90 mV [151]) that express Cx26 [152]).

During these simulations we noted ions passing through the channel, corresponding to a non-zero transmembrane current. We compute the current due to the passage of the ions using the current definition of Equation 5.7 (Figure 5.17). Interestingly, the trace in panel C reproduces qualitatively the flickering of a single channel patch clamp trace. However predicted current and conductance values are underestimated. This discrepancy can be ascribed to the inertia of the coarse grained ions, since they are always considered solvated and move together with several water molecules, thus that is they have a larger mass if

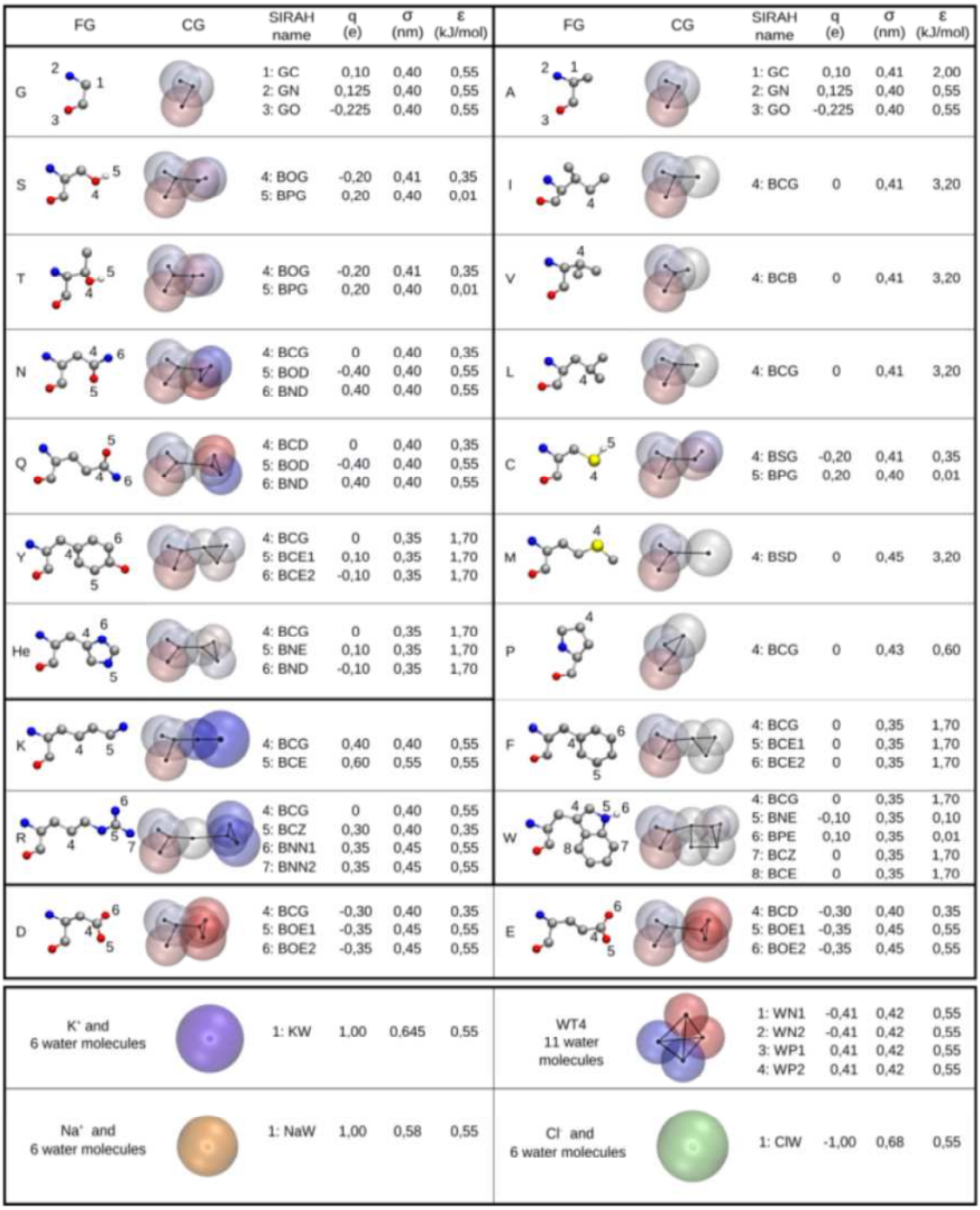

Figure 5.13: SIRAH representation of amino acids and solvent. The one-letter code, FG heavy atoms, CG representation, bead's names, partial charges, and vdW parameters are presented for each amino acid. Only hydrogen atoms used for the CG mapping are shown. Numbers near the FG atoms indicate the position for the corresponding CG beads. Backbone mapping is indicated only for glycine and alanine. FG atoms are colored by name, while CG beads of amino acid and WT4 are colored by charge range (negative, red; positive, blue). The sizes of all CG beads are at scale and correspond to their actual vdW radii [148].

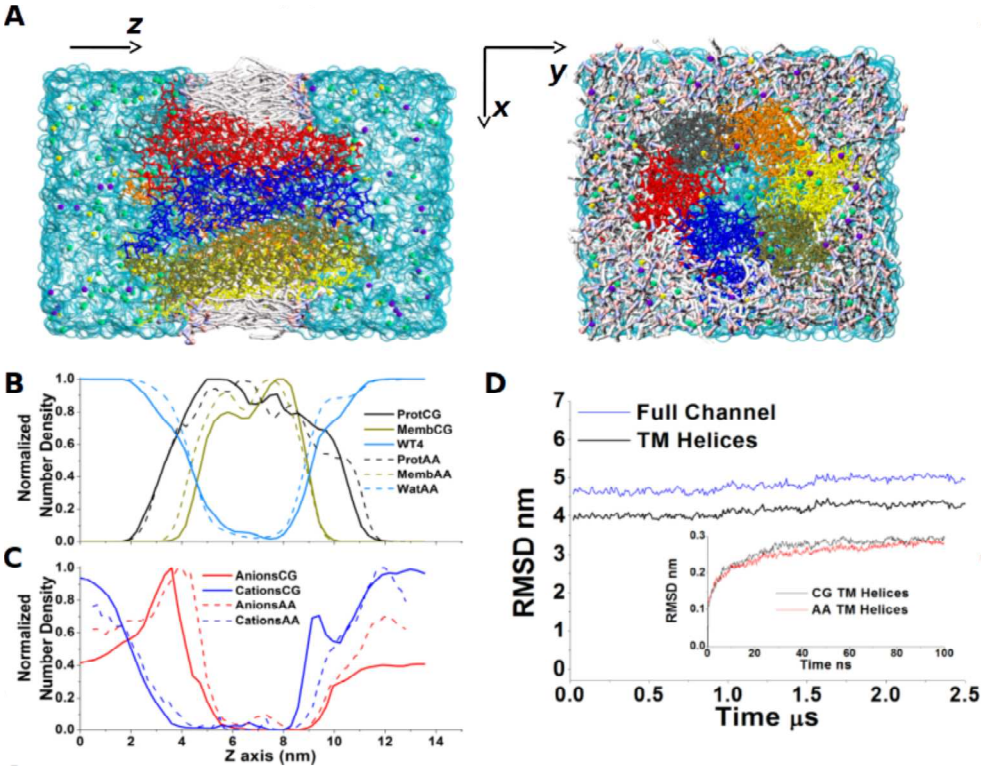

Figure 5.14: Comparison between AA and CG models. Continuous lines refer to the CG model, dashed lines to the AA model.

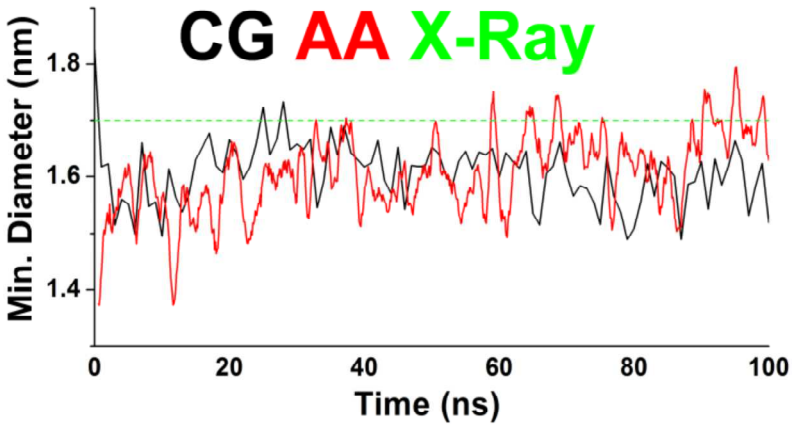

Figure 5.15: Comparison of the minimum diameter in AA model, CG model and X-Ray crystal structure.

compared with full atoms.

5.1.4 Comments

In addition to the conductance studies, from the analyses of these simulations we notice a change in the configuration of our hemichannel that occurs over 5 µs. This is an event that could not be seen with the AA model due to the time-scales involved. As can be seen from the panel A and C of Figure 5.17, ∼5 µs after the electric field was turned on, we observed

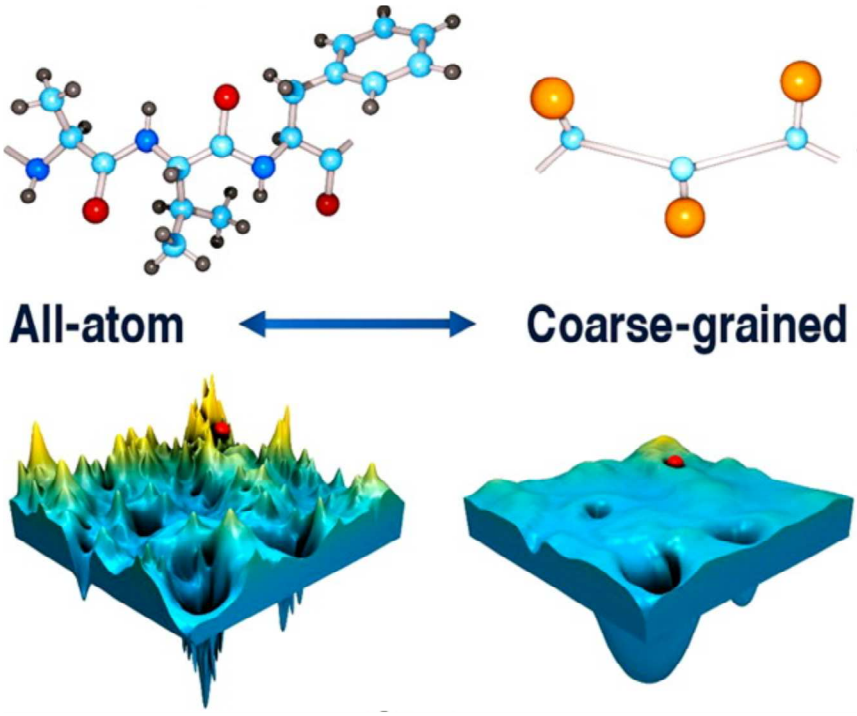

Figure 5.16: All-atom versus coarse-grained energy landscape [150]. The figure illustrates the effect of the smoothening of the energy landscape in a coarse-grained model as compared to an all-atom model. The flattening enables efficient exploration of the energy landscape in search for the global minima, while avoiding traps in the local minima.

a widening of the pore and consequently an increase in the passage of the ions through the hemichannel. Applying a negative potential (such as the ordinary resting cell membrane potential) promoted a progressive widening of the pore that reached steady state in about 5 µs. Under opposite polarity conditions, the structure relaxed to an intermediate pore widening state. Note that in all these simulations, Ca^{2+} was not included. The most remarkable changes were at the level of the residue 41 and the N-terminal helices. The former is the charged residue in the narrowest part of the pore and is considered responsible for the straight slope in the free energy potential for the passage of a molecule through the pore [20]]. The latter is considered an essential component for fast gating [80]], which is a very interesting aspect that we will analyse in future work. After the widening of the pore, a flux of ions was noted through the pore. The current detected in this way is lower than the one expected from the experiment. This can be due to the CG model of the ions that are composed of the classic AA ion plus the first solvatation shell. This make the ions slower than the corresponding ions in the AA model. flickering of the current trace was also noted. This can be explained by a visual inspection of the molecular dynamics trajectory. Indeed, during the maxima the hemichannel was full of ions ready to pass through the pore, while during the minima the channel was empty of ions and took time to be refilled.

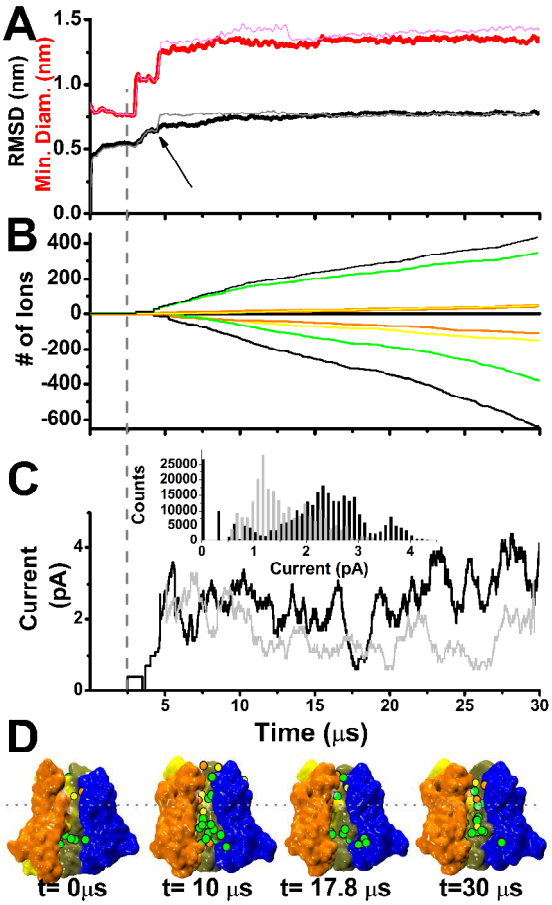

Figure 5.17: Currents in CG model. In this figure are presented two CG simulations in which, after 2.5 μsecond, we applied an electric field in the two opposite direction ($+z$ and $-z$) with magnitude 0.03 V/nm, corresponding (for a AA force field) to an estimated membrane potential of ± 120 mV, of the same order of magnitude of membrane potential in inner ear supporting cells (up to 90 mV [151]) that express Cx26 [152]). In panel **A** are presented the RMSD (black and grey) and Minimum Diameter (red and magenta) of the protein during the two simulations. The bold traces refer to the simulation with electric field in $-z$ direction. In panel **B** are presented the number of ions that pass through the channel (positive number for the simulation with electric field in $+z$ direction and negative number for the simulation with electric field in $-z$ direction). Green traces refer to Cl^- ions, red traces refer to K^+ ions, yellow traces refer to Na^+ ions and the black traces refer to the sum of the other three. In panel **C** are presented the current computed from the two simulations (black trace for the simulation with electric field in $+z$ direction and gry trace for the simulation with electric field in $-z$ direction). The projection of these traces along the ordinate axis form the histograms presented in the inset. In panel **D** are shown some snapshots of the simulations.

5.2 Steered Molecular Dynamics (SMD)

In order to avoid the time-scale problems in using the brute force method for computing the conductance of a gap junction channel, we tried a different method based on indirect computation of the conductance. These kinds of methods are based on the estimate of the

Free Energy profile for the passage of one ion through the pore (*i.e.* the energy barrier that has to be overcome by the ion in order to pass though the pore) [153, 154]. In this section one of the methods that can be used to compute the Free Energy profile for passage of one ion through the pore will be introduced. After the introduction of the method, two different interpretations that can be used to connect the Free Energy profile for the passage of one ion through the pore to the conductance of the hemichannel will be explained. At the end of the Section the application of these methods to one of our models of hCx26 connexon will be shown.

As mentioned above, *brute force* simulations for computing the conductance of a channel can be very time consuming and it is difficult to relate it with the experiment due to the differences in the time-scale and length-scale. For these reasons a different mode based on indirect methods that estimate the free energy profile for the passage of one ion through the hemichannel was also explored. However, the calculation of the free energy in the full configurational space can also be rather expensive in terms of computational resources, especially for large channels such as those we are interested in. For similar problems, one usually reduces the problem to a one dimensional approximation of the free energy, which is thus computed along a reaction coordinate, that in our case is the channel axis (set on z direction) [129, 155]. Free energy changes with respect to the reaction coordinate can be expressed in terms of the so-called potential of mean force (PMF), first introduced by Kirkwood in 1935 [156]. Let us consider a system of N particels with state defined by the 3 N-dimensional position $\mathbf{r}$ and momentum $\mathbf{p}$, and suppose we are interested in the free energy changes of the system with respect to some reaction $\xi(\mathbf{r})$. The PMF $\phi(\mathbf{r})$ is then defined by

$$exp[-\beta\phi(\xi')] = \int d\mathbf{r}d\mathbf{p}\delta[\xi(\mathbf{r}) - \xi']exp[-\beta H(\mathbf{r}, \mathbf{p})]$$

where $\beta = 1/k_B T$ and H represent the Hamiltonian function of the system. One of the methods widely used is the Steered Molecular Dynamics (SMD) biasing techniques. In SMD simulations, a force is applied to induce the process of interest, so that one can obtain important information on the process of interest while minimizing the computational cost. SMD thus allows us to quickly explore configurations along the path of interest, giving the possibility of inducing relatively large changes in the examined system on the nanosecond time scales accessible to actual computations. In SMD simulations, if we assume a single reaction coordinate x, the external time dependent force applied can be expressed as

$$F(x, t) = K(x_0 + vt - x)$$

This force corresponds to a molecule being pulled by a harmonic spring of stiffness K with its end moving with velocity v. Other kind of biases can also be induced, such as torsions or distance changes between two atoms or groups of atoms. SMD can provide important qualitative information in a variety of processes, such as small molecules passage through channels, unfolding and unbinding, thus revealing fundamental interactions on the process pathway. Quantitative information can also be extracted. PMFs can be extracted from non-equilibrium SMD simulations, using Jarzynski's equality [23]. The latter is a relation between equilibrium free energy differences and work done through non-equilibrium processes. Considering a process that changes a parameter λ of a system from λ_0 to λ_t at time t, the second law of thermodynamics states that the average of work W done on the system cannot be smaller than the difference between the free energies F corresponding to

the initial and final values of λ:

$$\Delta F = F(\lambda_t) - F(\lambda_0) \leq \langle W \rangle,$$

where the equality holds only if the process is quasi-static. Thus the average work for a non-equilibrium process provides only an upper limit for the free energy difference. However, Jarzynski derived the following equality

$$e^{-\beta \Delta F} = \langle e^{-\beta W} \rangle,$$

which holds regardless of the speed of the process, and has been tested against computer simulations and experiments. Hence, it is possible to obtain free energy profiles using non-equilibrium processes. However, this is still challenging, since the average of the exponential in Jarzynski equation is dominated by trajectories with small work value that arise only rarely. An accurate estimate of free energy hence requires suitable sampling of such rare trajectories. Therefore, although Jarzynski's equality holds for processes of any speed, practical applications are limited to slow processes for which the fluctuation of work is comparable with the temperature.

The relation between the PMF and the unitary conductance is not understood perfectly and a single interpretation does not exist. In this work we will use the SMD technique to compute the PMF and then we will interpret it using two different theories: the first is based on the Eyring transition rate theory while the second is a more precise method we derived based on the Smoluchowski equation.

5.2.1 The Eyring rate theory

In this section, the interpretation of the free energy profile will be briefly introduced in an analogous way to chemical reaction kinetic theory (saturating pore model) where the ion binds in the various minima of free energy (see Appendix C.1 for a more detailed explanation). Saturating pore models were first introduced in biology by Hodgkin and Keynes [157], and general theoretical methods were developed by Heckmann [158–161] and Läuger [162].

Let us consider the simplest saturable system, a channel with one binding site, X, that corresponds to a minimum of the free energy profile, and a permeating cation, S. If we replace all the subtleties of diffusion to and from the site by single rate constants k, the steps of permeation become :

$$X + S_o \underset{k_{-1}}{\overset{k_1}{\rightleftharpoons}} XS \underset{k_{-2}}{\overset{k_2}{\rightleftharpoons}} XS_i$$

where the rate constants are, in general, dependent on the voltage.

Eyring rate theory is a way to summarize the values of rate constants in binding models of permeation. Energy wells can represent binding sites, and the occupancy of sites can be specifically included in the rate equation for jumps in and out of each site. In general, the relation between the free energy of activation and the jump rate constant is defined by

$$k_f = k_0 exp(-\frac{\Delta G^{\ddagger}}{RT}) = k_0 exp(-\frac{\Delta H^{\ddagger}}{RT}) exp(\frac{\Delta S^{\ddagger}}{R}) \tag{5.5}$$

where the special symbols $S^{\ddagger}$, $H^{\ddagger}$ and $G^{\ddagger}$ stand for the standard entropy, enthalpy and Gibbs free energy of forming a mole of the activated complex from the reaction and the

"prefactor" k_0 is the frequency with which a transition-state complex would break down to products. If b_{-1} represents the value of k_{-1} at zero membrane potential ($E = 0$), then from the definitions given from the one-site model in Figure 5.18 we have:

$$b_{-1} = k_0 exp(-\frac{G_{12} - G_2}{RT}) \tag{5.6}$$

and so forth. The quantity δ in the Figure 5.18 represents the fraction of the total electrical potential drop, E, between the outside and the site. It is often called the *electrical distance* of the site from the outside. It should not be confused with the physical distance, which is far harder to determine.

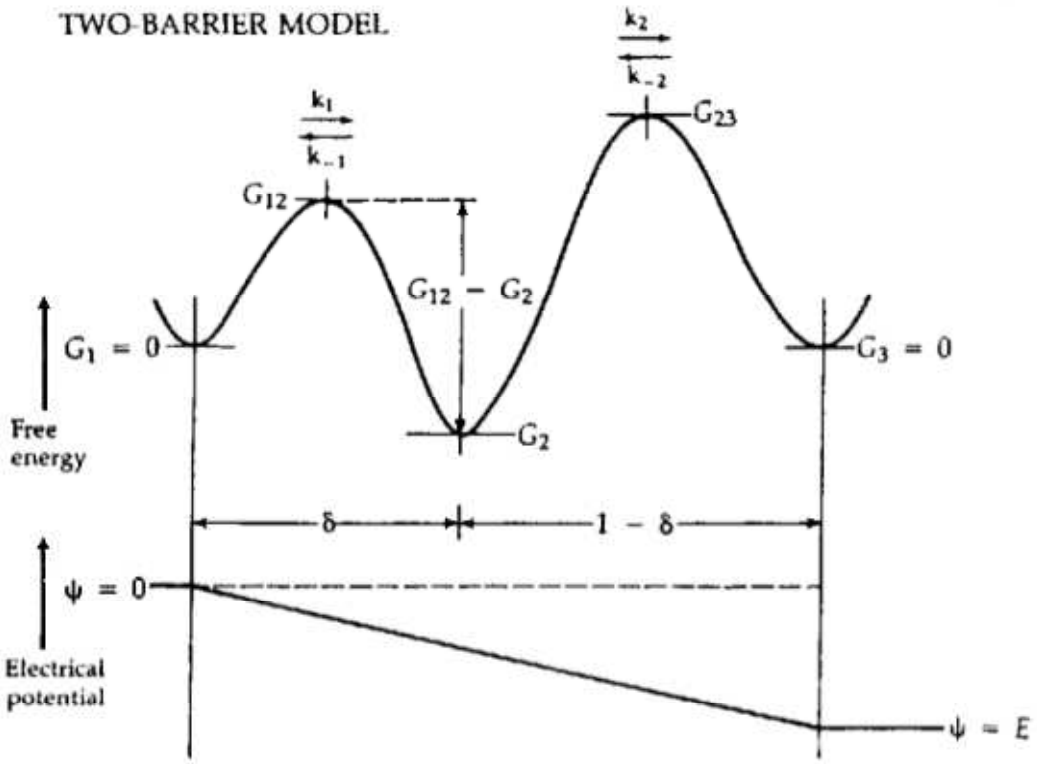

Figure 5.18: Simple Barrier Model of Pores Definition of quantities needed for a two-barrier, one-site model. The fluxes are described by four hopping rate constants, k_i. They may be calculated from the free-energy barriers of the transitions, which have a "chemical" component, G, and an electrical component proportional to the voltage drop traversed and the ionic valence. The free energies G_{12}, G_2, and G_{23} are defined relatively to the bulk solution.

Now we are interested in a simple estimation for the conductance. As previously said, conductance is a measure of conductivity, *i.e.* the ratio of the current flowing through a conductor and the difference in potential between the ends of the conductor.

Since the hopping rate is proportional to the flux in the correspondent direction and the latter is proportional to conductance, from equation 5.6 we can see the dependence of the conductance from the free energy profile at zero membrane potential. If we consider the hopping rates be independent, the total flux in one direction will be proportional to the product of the two rates and the conductance can be written as

$$\sigma = \alpha e^{-\frac{G_{12}-G_2}{RT}} e^{-\frac{G_{23}}{RT}} \tag{5.7}$$

where α is an appropriate constant.

In practical terms, the problem of calculating the constant α is rather complicated, and not fully understood yet, since it depends on the overall free energy profile, and not only on the free energy difference, however it is clear that the kinetic is completely dominated by the exponential part of equation 5.7 and, if one assumes that α depends weakly on the full free energy profile, this theory can be used to predict a ratio of conductance. In order to compute a singular value for conductance, we must adopt a different approach as will be seen in the next section.

Another important approximation introduced here, is the restriction to the single ion model. Even if junctional channels can host several ions simultaneously, a treatment in terms of multiple ion transition is complicated by the fact that these channels are much larger than selective ionic channels, and thus binding sites cannot in fact be defined. For these reasons, ions are rather mobile inside the channel, and the free energy profile will be instead computed for a single ion, in the presence of the mean interaction with all the other ions in the channel.

5.2.2 Using the Smoluchowski approach

A more precise value for conductance can be obtain by studying the diffusion of ions through the pore (described with free energy profile) using the Smoluchowski approach. Here we will present only a brief introduction to the used method and the result obtained skipping all the mathematical derivations that are fully explained in Appendix C.2. We start from a model to describe particle in a fluid that takes into account the inertial effect of Brownian particles. According to classical mechanics, the motion of a particle in a fluid would be described by Newton's second law

$$m\frac{d\vec{v}}{dt} = \vec{F}_T + \vec{F}_E(\vec{x})$$

where $\vec{v}$ is the velocity of the particles, $\vec{F}_E$ is the sum of external forces and $\vec{F}_T$ is the sum of the forces that each molecule of the fluid exerts on the particle. For simplicity we restrict to one dimension treatment. Using the hypothesis of strong friction, *i.e.* $\frac{d\vec{v}}{dt} \ll -\gamma\vec{v}$ (where γ is the friction coefficient) and supposing the fluid to be in a *stationary state*, we can write the Langevin equation that can be used to obtain the so called *Smoluchowski equation* (see Appendix C.2). The external force $F(x)$, in the diffusion space, is given by a potential $U(x)$, *i.e.* $F(x) = -\frac{dU(x)}{dx} \equiv -\dot{U}(x)$. Moreover, by identifying stationary state with thermal equilibrium, we can find a relation between the microscopic quantities (*e.g.* γ) with the macroscopic quantities D and T where D is the diffusion coefficient and T is the temperature of the thermal bath of our system.

Let us consider a stochastic process $\{X(t)\}_{t\geq 0}$ with realization $x(t)$. Since $X(t)$ is a random variable, it is reasonable to look at its probability density distribution $p(x,t|x_0)dx = \mathbb{P}\{x \leq X(t) \leq x + dx | X(0) = x_0\}$ defined on $\Omega = [r, \xi]$. We have to define the boundary conditions. We used r as reflection point (*i.e.* $\frac{\partial p}{\partial t}(x = r, t|x_0) = 0$) and ξ as an absorption

point (*i.e.* $p(x = \xi, t) = 0$). If the process starts at $x_0 = X(0)$, we define the *first passage time* (MFPT) of the process as the first time it will reach the boundary

$$\tau := \frac{1}{D} \int_{x_0}^{\xi} e^{\beta U(y)} dy \int_{r}^{y} e^{-\beta U(z)} dz. \tag{5.8}$$

where the MFPT has been identified with the time τ that one ion spends to pass through the channel.

Assuming that a single ion can occupy the channel, we can relate the flux J with the time τ as

$$J = \frac{1}{\tau},$$

so we can write the current I due to the passage of ions through the channel as

$$I = \frac{q}{\tau}$$

where q is the electric charge of a single ion.

If we have a single type of ion that creates the current(*e.g* K^+ like in many experimental conditions), the net current through the channel is due to the flux on the ions in one direction ($J_+ = \frac{1}{\tau_+}$) minus the flux in the opposite one ($J_- = \frac{1}{\tau_-}$). So we have

$$I = q(J_+ - J_-) = G\Delta V \tag{5.9}$$

where G is the conductance of the channel.

To compute the conductance we need a no zero current. Therefore the MFPT of one ion is calculated through the pore using the free energy profile plus a potential difference dependent on the position z, *i.e.* maximum in the first cell and then decreasing linearly until zero value in the second one.

Using this Smoluchowski approach we are able to compute the value of the conductance for the single channel bypassing the problem of the α constant of the Eyring theory. Furthermore we obtain a better approximation of the ratio value. We need to compute the mean first passage time of the ion using the free energy profile found with MD for the whole connexon channel. Using the mean first passage time we can compute the flux of one type of ions in one direction. Experimentally, measures of GJs conductance are done with a solution in which only one type of ions (*e.g.* K^+) moves through the pore. Whereby, in order to obtain a result comparable with experiments, we regard the passage through the GJ channel of only K^+ ions. Then we can use equation 5.9 to compute the current due to the net flux of K^+ ions through the pore. To have a value of I different from zero we must add a difference of potential ΔV between the two cells, given as a quantity with maximum value in the first cell and then decreasing linearly until zero value in the second one. The energy that needs to be added to the PMF in the point z is given by

$$U_{el}(z) = q\frac{\Delta V}{L}(L - z) \tag{5.10}$$

where L is the length of the channel.

In the next Subsection we will apply the SMD method and the two interpretation theory we have seen until here to our hCx26 hemichannel WT and M34T mutant model.

5.2.3 Application: the Cx26M34T mutant

The mutant Connexin 26 M34T has been experimentally well characterized and is known to be correctly synthesized and targetted to the plasma membrane in HeLa cells, but inefficiently forms intercellular channels that display an abnormal electrical behavior and retain only 11% of the unitary conductance of Connexin 26 Wild Type (Figure 5.19 [13]).

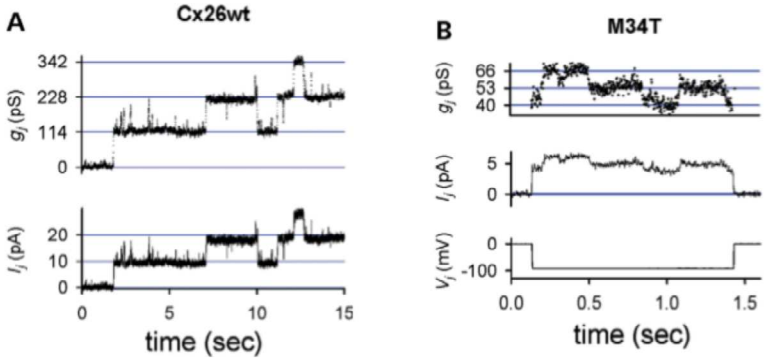

Figure 5.19: Electrical properties of Cx26WT and M34T mutant [13]. (A) Conductance changes (g_j, top trace) and corresponding discrete current transitions (I_j, bottom trace) due to gating of homotypic channels formed by human Cx26WT. Several opening and closing of gap junction channels were recorded with a transjunctional voltage (V_j) of $-95\,\text{mV}$ ($V_1 = -5\ mV$; $V_2 = -100\ mV$; $n = 4$). The calculated unitary conductance (γ) was 114 pS. **(B)** Conductance changes (g_j, top trace) and corresponding rapid current transitions (I_j, bottom trace) due to opening of homotypic channels formed by M34T mutant recorded under a sustained V_j of $-100\,\text{mV}$ ($V_1 = 0\ mV$; $V_2 = -100\ mV$; $n = 2$). The estimated γ was $\sim 13\ pS$.

This dysfunction of the mutant hemichannel makes it a perfect candidate for study the unitary conductance and comparing the results with the conductance study of the Wild Type hemichannel. First of all, we build the full atom model of the mutant hemichannel starting from the previously described molecular models (Chapter 3) based on the 3.5 Å X-ray data [17] and mutating the 34th amino acid of each connexin protomers. As done previously for Cx26WT, we embedded the Cx26M34T hemichannel in a plasma membrane represented by 494 Palmytoyl Oleoyl Posphatidly Choline molecules (POPC). The system then was solvated with full atom TIP3P water containing K^+ and CL^- ions at a concentration of $\sim 0.15\ M$ to neutralize the positive net charge of the connexon and to mimic a physiological ionic strength. The whole system comprised 205825 atoms for Cx26M34T model. We initially performed a short energy minimization run, followed by equilibrium molecular dynamics of 40 ns. The root mean squared deviation (RMSD) of the transmembrane domain stabilized after 15 ns and the short range interaction between membrane and protein.

To study the unitary conductance of the two hemichannels, we computed the PMFs for the passage of a K^+ ion through the WT and mutant hemichannels using a Steered Molecular Dynamics technique. In this type of simulation we need to keep the position of protein hemichannel as fixed as possible. For this reason we performed the simulation in constant volume condition in order to avoid the changing of the box size and the consequential rearrangement and movement of all the system that can lead to problem with the pulling code. To force the passage of a K^+ ion through the channel pore, we

connected it to one end of a linear spring with elastic constant k of 2000 kJ mol^{-1} nm^{-2} and zero resting length. The other end of the spring shifted along pore axis (z direction) from the cytoplasmic to the extracellular side of the hemichannel at a constant velocity of 0.5 nm ns^{-1}. The shifting spring was stiff enough to keep the K^+ in the proximity of the z axis, with a standard deviation of 0.034 nm. The simulations spanned a total of 8.6 nm in 17.2 ns for each system. The mean force F(x, y, z) exerted on the ion by he hemichannel amino acids was gauged by the instantaneous spring extension averaged over 40 ps time intervals. F(x, y, z) balanced effectively all other forces acting on the ion at each point along the K^+ trajectory, therefore the work profile

$$W_{HC}(z) = \int_0^z F_z(0, 0, \zeta) d\zeta \tag{5.11}$$

which is known as the PMF, has the meaning of a free energy profile for the permeation of a single K^+ ion through the hemichannel (HC) pore (Figure 5.20). To compare our result with the experiment, we derived the PMF for the full gap junction channel $W_{GJ}(z)$ (Figure 5.20, inset) by reflecting $W_{HC}(z)$ about a vertical axis passing through the z coordinate corresponding to extracellular end of the hemichannel [20].

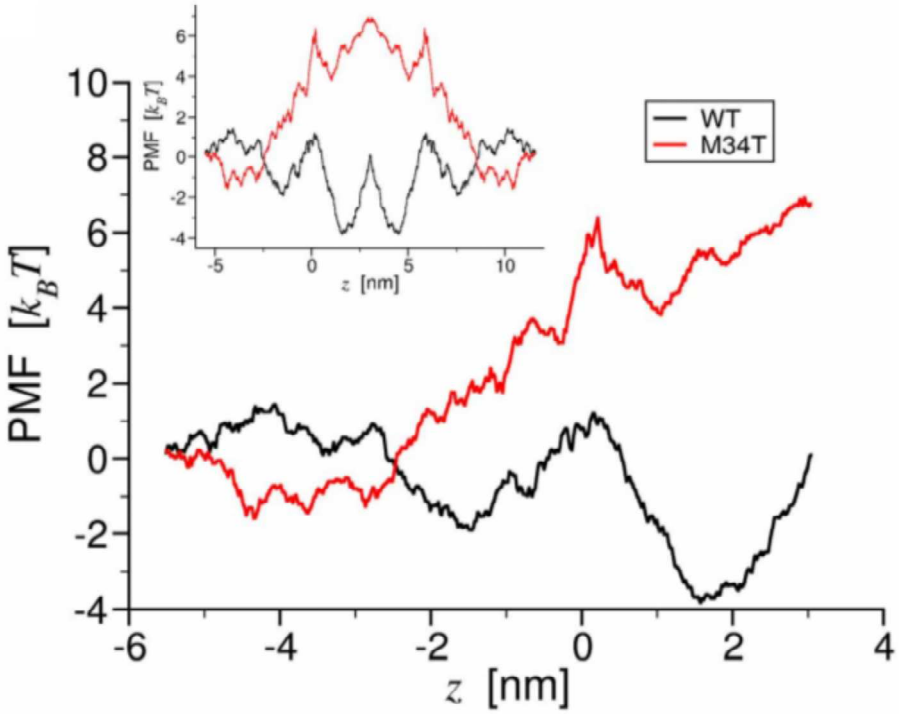

Figure 5.20: Potential of Mean Force of potassium ion permeation through Cx26WT and Cx26M34T. The figure shows the total PMF for a single K^+ ion permeating through the two different hemichannels as a function of the pore axial coordinate. The black trace corresponds to the wild type, while the red trace to the mutant. The inset shows the corresponding PMFs for the entire gap junction channel.

The two traces shown in Figure 5.20 are clearly different, and the energy barrier that the K^+ ion has to overcame in order to pass the channel is higher for the mutant channel than the WT. This is qualitatively in agreement with the experimental data, but if we

want to link quantitatively PMF and ionic conductance we need an interpretative theory for the PMF.

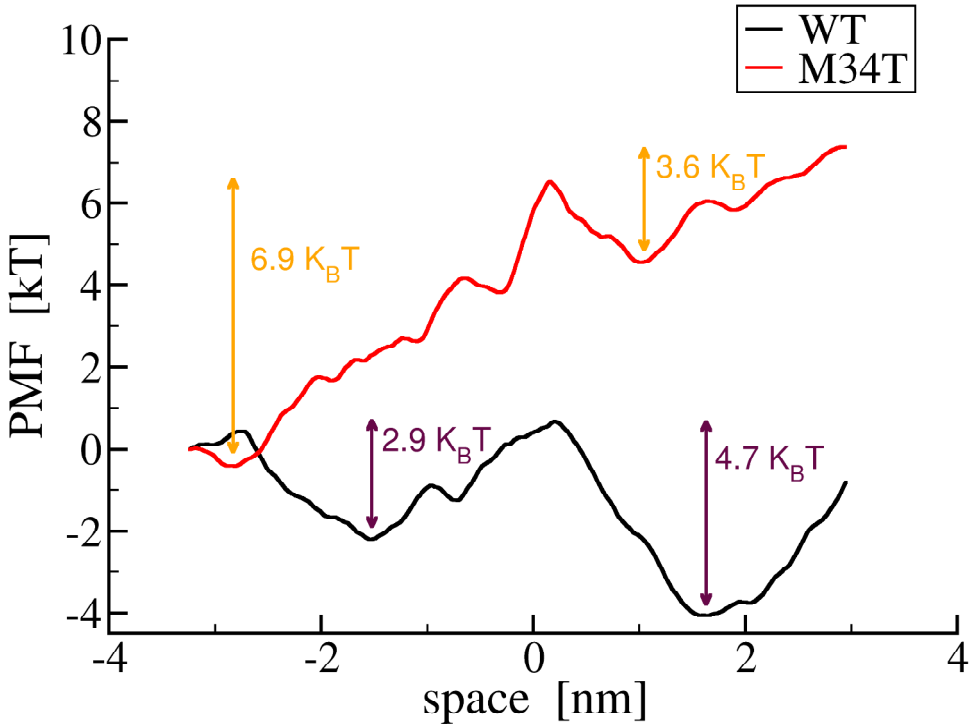

Figure 5.21: PMF of K^+ through Cx26WT and M34T mutant. In this picture was highlighted the potential wells delineated by our simulation along the pore axis of Cx26 WT and M34T mutant were highlighted. The largest difference between WT and M34T is present approximatively between z position $-2.5\,\mathrm{nm}$ to $0\,\mathrm{nm}$. In this position we can find the N-terminal helices of the six proteins and the residue 34.

In the assumption seen in the Section 5.2.1, we can apply equation 5.7 to our case. Changing the magnitude of free energy we can write

$$\sigma = \alpha e^{-\frac{\Delta G_1}{k_B T}} e^{-\frac{\Delta G_2}{k_B T}} \tag{5.12}$$

where ΔG_1 and ΔG_2 are the depth of the two potential wells highlighted in Figure 5.21 for Cx26 WT and M34T. To write equation 5.12 we assumed that the probability of hopping the first well is independent from the hopping of the second. This is a good approximation if we are not under saturation or competition conditions. However, since junctional channels are larger than selective ion channels, it is not obvious that binding sites actually exist and, apart from the narrower segment of the channel, more than one ion can be hosted in the same coordinate along the channel axis. For this reason, instead of introducing the interaction with other ions in terms of competition and saturation, we let them free to enter and exit the channel during the simulations. In this way, since their diffusion is higher than the pulled potassium ion (KPull), their interaction with the KPull is directly take into account in the calculation of the mean force, as the interaction of all other molecules

in the system. Using equation 5.12 to PMF profile of Cx26 WT and M34T, and assuming that the proportional constants are the same, we obtain

$$\frac{\sigma_{WT}}{\sigma_{M34T}} = \frac{e^{-\frac{\Delta G_1^{WT}}{k_B T}} e^{-\frac{\Delta G_2^{WT}}{k_B T}}}{e^{-\frac{\Delta G_1^{M34T}}{k_B T}} e^{-\frac{\Delta G_2^{M34T}}{k_B T}}} \simeq 18.17 \tag{5.13}$$

Experimentally it is found that the M34T mutant retained only 11% of the unitary conductance of the WT, so our result is of the same order.

To improve our results and compute a qualitative measurement of the current flowing through one hemichannel, we want to apply the Smoluchowski approach we have seen in the Subsection 5.2.2. Using Equation 5.10 we computed 10 points with ΔV that spans from 10 mV to 100 mV, reported in Figure 5.22. The slope of the straight lines obtained, gives us the conductance (G) of the channels. The results are presented in the second column of Table 5.1.

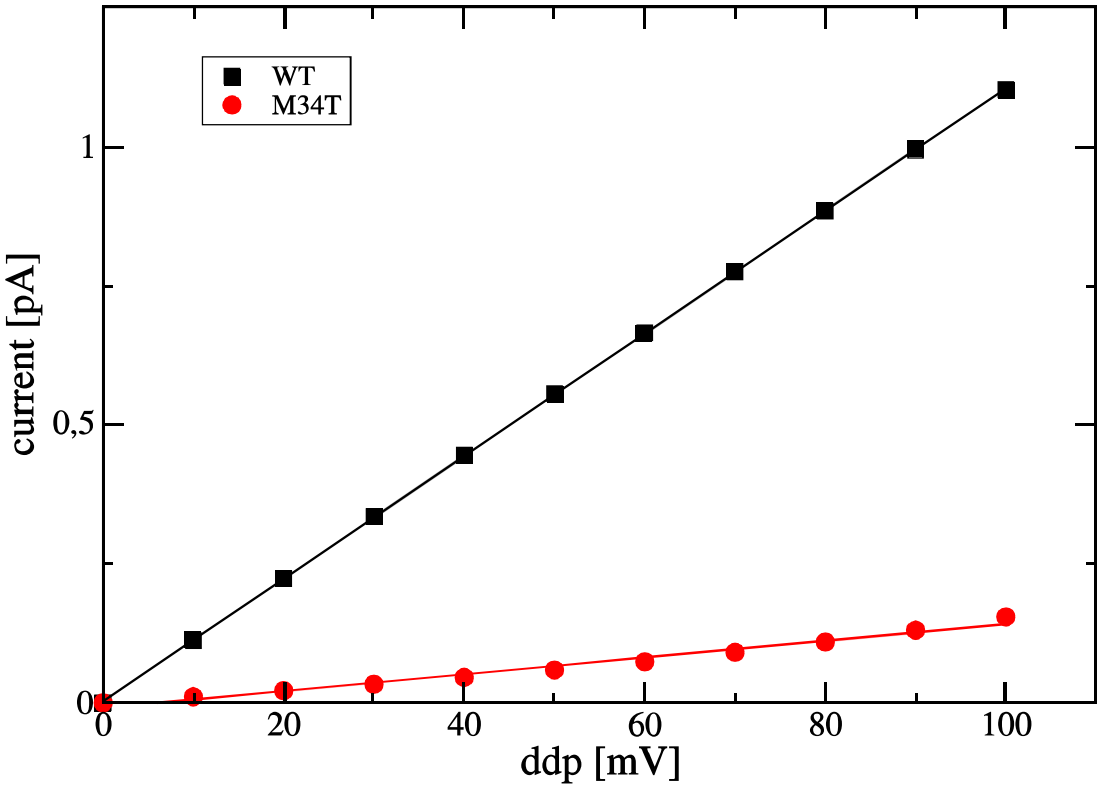

Figure 5.22: Conductance The different points represent current value through the pore compound with Smoluchowski approach for different values of ddp added to the PMF of the whole channels. The lines are the linear regression of the points and the slope of the curves give the conductance of the channels.

The results that we obtained are one order of magnitude smaller in comparison with the experimental results. In the article we published [21], we consider the approximation introduced on the calculation to find a way to improve our results. The correction that we introduced was reasonable, but after the study with the coarse grained model and the observation of a different state of the connexon, that can be linked to a more conductive

state of the hemichannel, we have to leave that correction and consider different causes for the differences between the experimental values and the results we have obtained.

	Single ion [pS]	Experimental value [pS]
WT	11.02	114
M34T	1.51	13
Ratio M34T/WT	9.6%	11.4%

Table 5.1: Comparison between conductance predicted by molecular dynamics simulation (Smoluchowski approach) and experimental values.

After the computation of the conductance for the mutant and WT hCx26 hemichannel, we want to discuss a possible molecular explanation for the differences, compatible with the experimental results, that we have found. Considering the two profiles in Figure 5.21 it is possible to note that the largest difference between WT and M34T is present approximatively between z position $-2.5\,\mathrm{nm}$ to $0\,\mathrm{nm}$. In this position we can find the N-terminal helices of the six proteins and the residue 34. According to the published X–ray model of the human Cx26WT gap junction channel [17], M34 interacts with W3 of the NTH belonging to an adjacent connexin. The six NTHs fold inside the pore and the M34-W3 hydrophobic interactions stabilize their position at the cytoplasmic mouth [17]. The absence of bond between residue 34 and residue 3 of the adjacent connexin, gives to N-terminal helices more freedom to move when compared to WT. Experiments and theoretical studies suggested that under application of external electric fields, Cx26 channel exhibits a mechanism of *gating* that seems to involve the N-terminal helices [80].

As mentioned in the Section 5.1.3, we have seen a similar configuration change involving the N-terminal helices and leads to a change in the conductance of the connexon applying an external electric fields on the Coarse Grained model. Moreover the low resolution crystallographic structure of similar mutant Cx26 M34A [163], shows a "plug" in the middle of the pore that was hypothesized to be created by an asymmetrical configuration of N-terminal helices. Our MD model of M34T mutant, does not display an actual occlusion of the pore, however this can be due only to the short Molecular Dynamics equilibrium trajectory we have produced (around 40 ns), and thus the correct equilibrium could not be achieved. There is also a more interesting possibility: that helices enter the channel only if excited by external forces, created, for instance, by the interaction with permeating molecules, or by external voltage differences like those created in patch clamp experimentally.

To investigate this possibility, we decided to stress the system at the N-terminal helices position in order to understand how the mutation affects the response to external stimuli. This was realized by applying an external mechanical force on N-terminal helices, *i.e.* applying a SMD on each helix of the hemichannel, which moves it from its initial position to the opposite side (Fig. 5.23). Similarly to the pulling seen at the beginning of this Subsection, we used an harmonic potential in the chosen direction with its equilibrium position constantly moving in time. The result is that the force exerted at a given time is described by equation 5.2. The force constant K is set to $100\,\mathrm{kJ\,mol^{-1}nm^{-2}}$, while the velocity v was taken $1\,\mathrm{nm/ns}$.

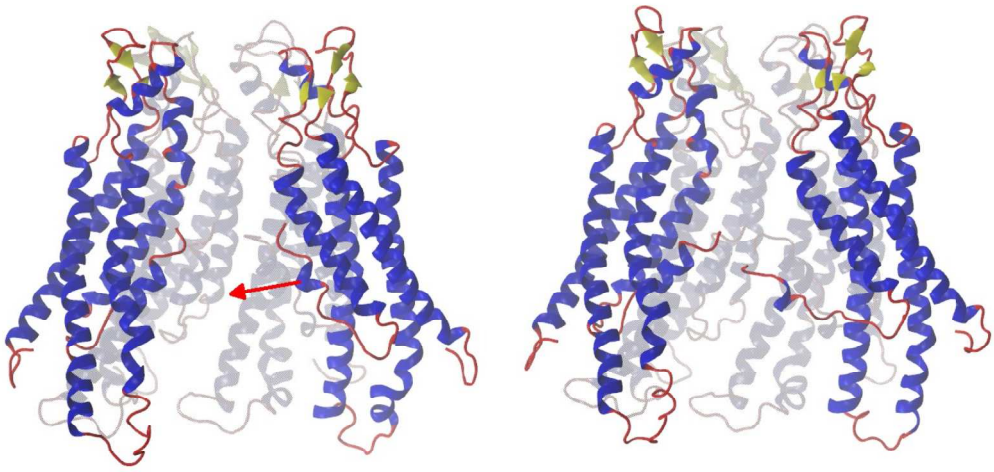

Figure 5.23: Example of start-end configuration in SMD of helix. The first frame shows the start configuration of SMD on N-terminal helix of the right protein. In the second frame can be observe the last configuration of the simulation can be observed. The arrow showa the pull Direction

In order to allow the pulled helix to detach from the transmembrane helical bundle and fully occupy the pore, at least 4 ns of simulation were required. Pull group positions and external forces were saved to disk every 100 fs of simulation time. Again the simulation was carried out at constant temperature and volume and with fixed COM at initial position.

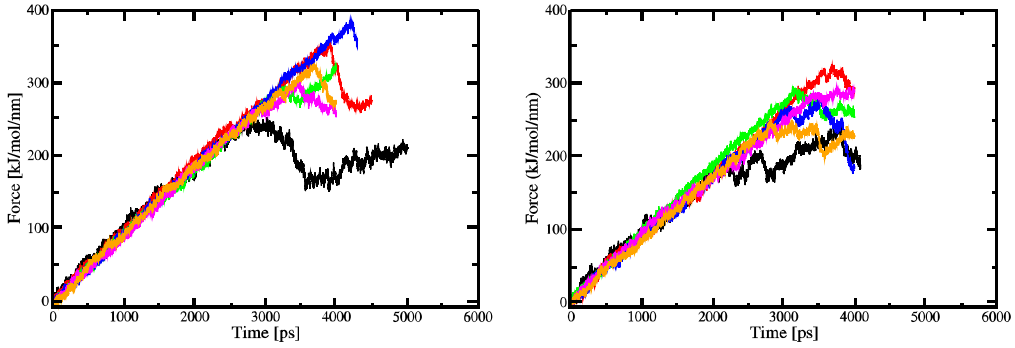

Figure 5.24: Pulling force on helices. In this graphics are plotted raw pull force data for of each trajectory corresponding to the six different helices (the six different color) for Cx26WT (*left* panel) and Cx26M34T (*right* panel).

Pulling force The observable that we followed during the dynamics was the force versus simulation time. With this parameter we want to see the different forces needed to knock off the pulled N-terminal helix from the initial position. Indeed, since we are applying an harmonic force, with one end anchored to the pulled helix, and the other moving towards the centre of the channel, the pull force constantly increases over time (on average), until the helix starts to move. At this point the force drops rapidly because the helix moves suddenly when its bound with the other helices is broken. The value of the force for which this effect happens can be regarded to as the detaching force. We expect that the helices of

M34T connexon, in comparison to WT, need a lower force to start to move in the pulled direction. In Figure 5.24 we have the six different pullings for WT and M34T. Both for WT and M34T, the fluctuations of force are quite large, due to the high thermal noise, moreover, there seems to exist an intrinsic variation of force profile, from helix to helix, due to the slightly different initial configuration of each helix.

Nevertheless, if we average the six different traces, and then compute another running average to reduce the thermal noise, we find that M34T actually moves at slower force. This is highlighted in the inset of Figure 5.25 where we can notice that the force value at which M34T distribution changes slope is about 100 kJ/mol/nm versus 300 kJ/mol/nm of WT. After this initial motion, the pulled helix is not able to collapse immediately towards the centre of the channel, but seems to linger around the new equilibrium position. However, a visual inspection of trajectory reveals that this effect is due to an interaction with a neighbouring helix, created by salt bridges between the positively charged amino group of *Met* 1 and negatively charged carboxylic group of *Asp* 2, which does not happen in WT, but systematically in the mutant because the M34T helices are quite free to move and interact easily between each other.

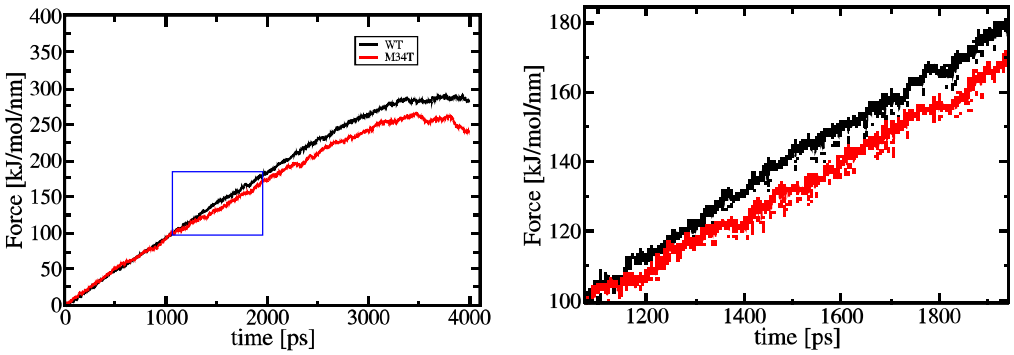

Figure 5.25: Filtered Average pulling force. The *left* plot shows the mean obtained from the six raw traces (Fig 5.24), after application of a further running average over 200 fs in order to reduce thermal noise. The blue box is zoomed in *right* panel, showing more clearly the point where the two traces separate. Error bars shown are standard deviation obtained from the running average. Visual inspection of trajectories revealed that, in the mutant, the detached helix interacts with a neighboring NTH, due to the more asymmetric shape of the pore mouth. This interaction obstacles the motion of the helix towards the centre, until the pulling force is large enough to break it.

Our data, then, indicate that N-terminal helices of the mutant are more mobile in equilibrium conditions and also respond faster to external stimuli.

5.2.4 Comments

As previously stated, at a cellular level the deafness–associated Cx26M34T mutant is correctly synthesized and targeted to the plasma membrane in HeLa cells, but forms intercellular channels inefficiently that display an abnormal electrical behaviour and retain only 11% of the unitary conductance of Cx26WT [13].

We obtained the free energy profiles for potassium permeation in a Wild Type and a M34T mutant hemichannel using Steered Molecular Dynamics, i.e. by forcing the ion to

move across the pore and calculating the potential of mean force (PMF) it was subjected to during this motion. Jarzinsky inequality assures us that the PMF can be regarded as a good approximation of free energy. Then we related this free energy directly to the conductance: using Eyring's transition state theory, we know that conductance must be proportional to the exponential of the total free energy gap. Assuming that the proportionality is constant and is related to the diffusion coefficient of the ion, and does not depend on the free energy profile itself, we can calculate the ratio between two conductances. We also used a second, more refined theory based on the Smoluchowski equation: we computed the mean first passage time (MFPT) using the free energy profile plus an energy given by a differential of potential dependent on the position z . Then, by assuming that only a single ion can occupy the channel at any one time, we related that time with the flux J of ions through the pore. The net flux of one ion type gives rise to a current that is linearly dependent to the difference of potential added to the free energy. The conductance ratio predicted by our models is $18:1$ and $10:1$ for Cx26M34T with the Eyring transition state theory and theory based on Smoluchowski equation, respectively. These results are both firmly in agreement with the experimental value $(11:1)$.

It is interesting to note that the most important difference between the two profiles arises around the position of methionine 34, indicating that what we observe is a genuine effect of the mutation. What happens at the molecular level, when methionine 34 is mutated into a threonine, is that the bond that kept together the N-terminal helices with the first transmembrane helix of the adjacent connexin is lost. This results in an increased mobility of N-terminal helices, which are no longer attached to the transmembrane helical bundle, and are therefore more able to protrude into the pore. In order to check this effect of the mutation, we performed a set of simulations. These simulations indicate that the NTHs in the Cx26M34T mutant are less bound to the channel wall (Figure 5.25) and we speculate that, for this reason, the gating mechanism is compromised, as proposed in [164].

In the next chapter we examine a different computational method to compute the PMF, and we will apply it to the passage of small molecules through a connexin channel. As we will see, using small molecules we increased the number of degrees of freedom of the system and the convergence of the PMF became more challenging.

Chapter 6

Permeability

The term permeability is widely used to describe the leakiness of a membrane to some substance. Conductance and ion permeability are both measures of the leakiness of a channel which can be related, but they are also two properties of the channel that can provide different kinds of information.

In the previous chapter we examined different methods of computing the conductance of a channel using the molecular dynamics techniques. It is very difficult to have quantitative results of a single channel conductance, but we can obtain reliable results for ratio of conductances. Now we want to use molecular dynamics simulations to study the permeability properties of a channel of interesting biological molecules. Here we will also use it to compute the permeability ratio, but we will try to obtain quantitative results.

In literature there are only two previous attempts to compute the permeability of Connexin hemichannel to large molecules using molecular dynamics simulations [20, 165].

The first attempt was made by Zonta *et al.* in 2013 for the passage of a *calcein* molecule (a widely used inorganic fluorescent tracer) through homomeric gap junction channels formed by wild type human connexin26 protomers. In this work they computed the PMF (see Figure 6.1) for the passage of the molecule through the pore, finding a huge barrier for the calcein molecule in a full charge state (as expected at neutral pH in the bulk) and a greatly reduced barrier for the calcein molecule in a fully protonated state (*i.e.* with zero total charge). Using the Eyring transition state theory to interpret the PMF, their simulations indicate that a calcein molecule with a presumptive physiological charge is unable to traverse the channel due to the size of the energy barrier it faces ($45.2 k_B T$). In contrast, the predicted transition rate for a calcein molecule with zero charge is compatible with the experimentally determined value. Based on this analysis they concluded that the structural model of the hCx26wt channel derived from the 3.5 Å X–ray data [17] is not permeable to calcein (even after MD relaxation) and the blockade is essentially electrostatic.

In the article by Luo *et al.* [165], the passage of two uncharged derivatized sugars was studied, one permeable (PA-disaccharide) and one impermeable (PA-trisaccharide), through a connexin26 channel model. In the results they show the PMFs for the passage of the molecules through the hemichannel (Figure 6.2, left) interpreting them in two different ways: using the Boltzmann factor and with a method based on Eyring transition state theory. With the Boltzmann factor the trisaccharide is ~ 125 times less permeable then the disaccharide, while with the second method the disaccharide is 100 times more likely to

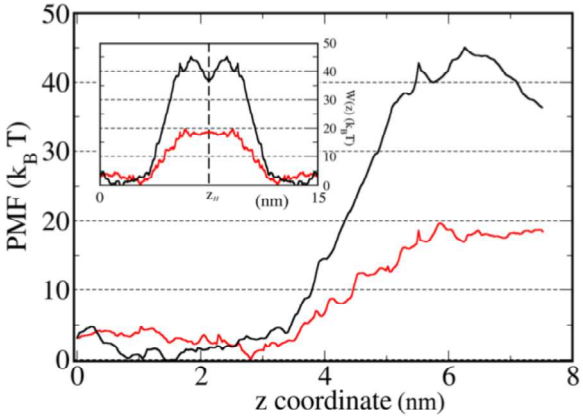

Figure 6.1: Comparison of PMFs for the permeation of charged (black) and uncharged calcein (red). The main graphs show PMF profiles for a human Cx26wt hemichannel. Inset: corresponding free energy profiles, W(z), for a complete gap junction channel obtained by reflecting the hemichannel PMFs about a vertical axis through the z_H abscissa [20].

pass through the restricted region of the channel than the trisaccharide. Both the results are in agreement with the experiments. Moreover we found out that permeating molecules tend to "widen" the lumen as they pass through and then that the permeating molecules may do work on the pore (Figure 6.2, right). With this study they conclude, in contrast with Ref [20], to have provided a qualitative validation of the Cx26 channel model in an open state. The PMFs they computed reproduces the permeant/nonpermeant properties of two molecules. The results highlight factors uniquely involved in permeation by molecule, as opposed to atomic ions. These include factors that arose from mechanisms of selectivity involving lower-energy interactions, "permeant" and sidechain flexibility, orientation, and anisotropy, wider pore.

In both these works, the PMF for the passage of the molecule was computed using methods based on *umbrella sampling* technique. Simulating rare processes such as the diffusion of a large molecule through a channel is very expensive in terms of computational time and there are no guarantees that the process will occur. Indeed direct simulation of molecule permeation through a gap junction channel is beyond the current computational power due to the time-scales involved (of the order of few ms). For a system as large as the one we are examining (with $>2 \times 10^5$ atoms) this falls outside the time window of the state of the art MD simulations (0.1 to 1 µs) notably. As mentioned in Chapter 5, different approaches have been developed to deal with these kinds of situations. In Section 5.2 we examined the SMD technique that we applied to the hCx26 hemichannel in order to compute the PMF for the passage of a K^+ ion. This method was accurate enough to have good results with the K^+ ion. In this chapter we investigate the passage of large molecules (IP_3, ATP and *glucose*) that, conversely to the atomic ions, have a lot of freedom, giving rise to the necessity of using a more accurate method of sampling. For this reason, following the two previous works [20, 165]], we are going to use the umbrella sampling technique [166, 167], one of the most widely used methods based on equilibrium simulations. In the following sections we will see a brief introduction to the Umbrella Sampling method and we will apply it to compute the PMFs for the passage of molecules

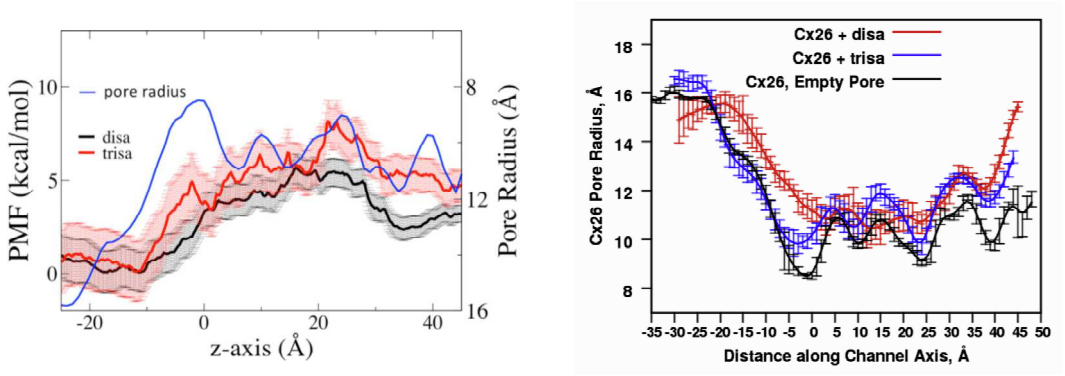

(a) (b)

Figure 6.2: PMFs and radius of Cx26 for the passage of disaccharide and trisaccharide. (left) The blue line is the unoccupied pore radius, plotted with decreasing width toward the top. The error bars are standard deviations calculated from 100 bootstrapped PMFs. The disaccharide and trisaccharide are denoted by "disa" and "trisa", respectively. (right) Radius of the pore at the position of the test molecules. The average radius of the pore at the position of the test molecule at each position with a COM xy restraint. For comparison, the Cx26 pore radius without the test molecules is shown. The error bars are standard errors of the mean. [165].

through a hCx26 hemichannel WT and V84L mutant.

6.1 The Umbrella Sampling technique (US)

The PMF [168] is an approximation of the free energy changes along one or more reaction coordinates. One of the most frequently used and effective methods for computing it is the umbrella sampling (US) technique [167, 169, 170].

The US biased simulations are generated using harmonic functions of the form $w_i(\xi) = 1/2k((\xi - \xi_i)^2$, centred on successive values of ξ_i. The biasing potential serves to confine the variations of the coordinate ξ: within a small interval around some prescribed value, helping to achieve a more efficient configurational sampling in this region (this is the reason why the biasing potential is called a window potential). Because the sampling is confined to a small region during a given biased simulation, only a small piece of the estimated PMF is sufficiently accurate to be useful. To obtain the PMF over the whole range of interest of ξ, it is necessary to perform a number of biased window simulations, each biasing the configurational sampling around a different region of ξ. In this way the molecule is forced to explore the space orthogonal to a fixed ξ_i value of the reaction coordinate.

Initial configurations for each window of umbrella sampling are extracted from a steered Molecular Dynamics trajectory of the molecule transition through the hemichannel (Figure 6.3). In this preliminary simulation, the molecule has to be dragged through the pore by an elastic force

$$F(z,t) = -K_{pull}[z - (z_0 + vt)] \tag{6.1}$$

from the cytoplasmic to the extracellular side. Here z, our chosen reaction coordinate, is positioned along the pore axis, K_{pull} is the stiffness of a harmonic spring one end of which moved with constant velocity v (pull rate) along z while the centre of mass of the molecule

is attached to the opposite spring end and also restrained to move along the pore axis.

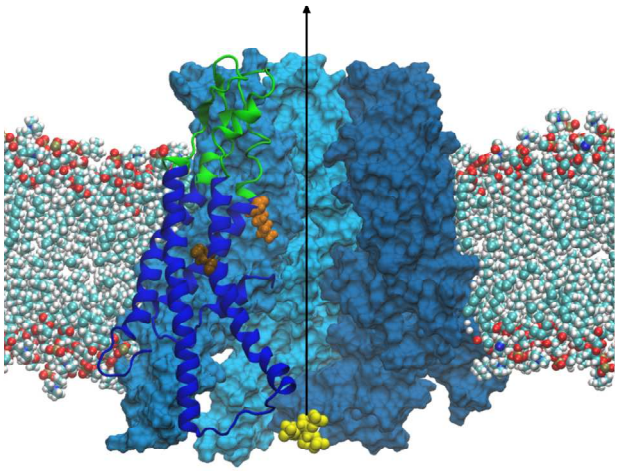

Figure 6.3: Starting configuration.

To obtain the PMF over the whole range of interest of ξ, 60 biased window simulations were performed, each biasing the configurational sampling around a different region of ξ spanning the 6 nm of length of the pore. We extracted the initial configuration from the SMD simulation as previously explained, and imposed a linear distance between every ξ_i and ξ_{i+1} of 1 Å. The harmonic function was expressed by a linear spring with zero resting length and elastic constant k of 2000 kJ mol^{-1} nm^{-2}. Ultimately, the results of the various windows were unbiased and then recombined together to obtain the final estimate $W(\xi)$.

6.2 Application: the Cx26V84L mutant

The mutant Connexin 26 V84L has been experimentally well characterized and, unlike other Cx26 mutations, it affects neither intracellular sorting nor electrical coupling, but specifically reduces permeability to the $Ca^{2+}-$mobilizing messenger Inositol trisphosphate (IP_3) (Figure 6.4 [14]). Moreover, recent studies suggest that it might also impair release of ATP through unapposed hemichannels [48].

In this Chapter we want to reproduce the experimental results for IP_3 molecule [14] and test the permeability of the hemichannel to ATP molecules using Molecular Dynamics technique. After that we also want to test if we can predict the passage impairment of a uncharged small molecule like glucose. As mentioned in Chapter 3, we started building the full atom model of the mutant hemichannel starting from the previously described molecular models (Chapter 3) based on the 3.5 Å X-ray data [17] and mutating the $84th$ amino acid of each connexin protomers. As done previously for Cx26WT, we embedded the Cx26V84L hemichannel in a plasma membrane represented by 494 Palmytoyl Oleoyl Posphatidly Choline molecules (POPC). The system then was solvated with full atom TIP3P water containing K^+ and CL^- ions at a concentration of ~ 0.15 M to neutralize the positive net charge of the connexon and to mimic a physiological ionic strength. The

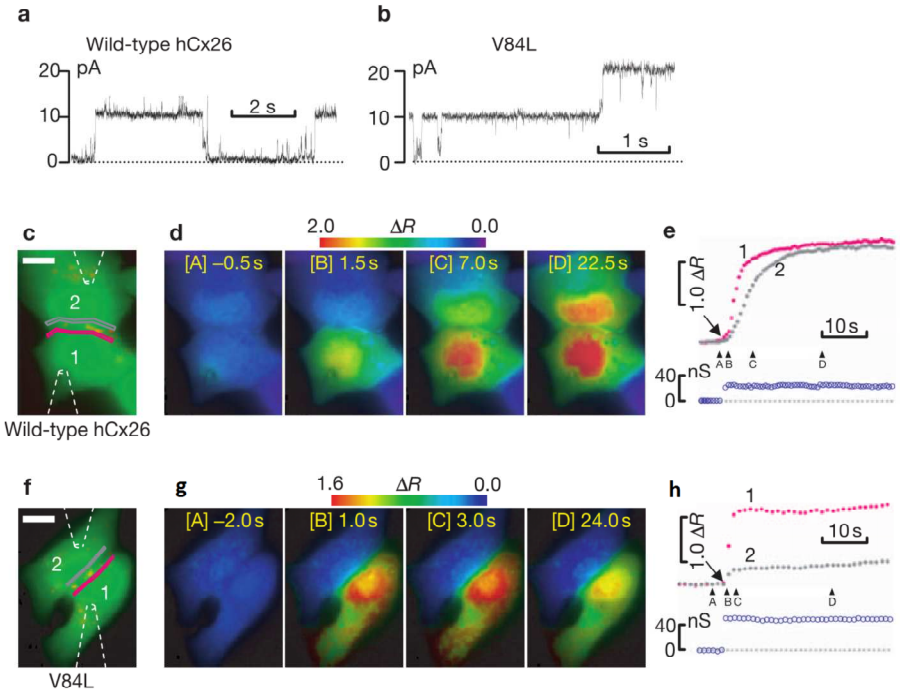

Figure 6.4: Electrical conductance and measurement of $Ins(1,4,5)P_3$ permeability [14]. **(a-b)** Representative recordings showing discrete step-like transitions in the junctional current I_j due to the gating of gap-junction channels during recovery from CO_2 acidification in HeLa-cell pairs transfected with wild-type hCx26 **(a)** and V84L mutant connexins **(b)**. Transjunctional voltage V_j was 90 mV in **a** and 95 mV in **b**. **(c)** Fluorescence-merge image of two adjacent cells loaded with fura-2-AM (in green) showing localization of the wild-type human Cx26-CFP fusion proteins to cell-cell junctions (in red). Intracellular delivery of $Ins(1,4,5)P_3$ (500 µM) into the donor cell (cell 1) started 8 s after the onset of the recording. **(d)** False-colour images **(c-f)** (also tagged within seconds of the onset of $Ins(1,4,5)P_3$ delivery) sampling the time course of fura-2 fluorescence ratio changes, ΔR. **(e)** Top, ΔR traces from the corresponding regions of interest on the two sides of the gap junction in **c**; bottom, junction conductance (g_j , in nS) monitored during image acquisition. Letters below arrowheads in **e** are matched to image tags in **d**. **(f-h)** Corresponding results from cells transfected with the V84L mutant.

whole system comprised 205923 atoms for Cx26V84L model. We performed a short energy minimization run, followed by a long equilibrium molecular dynamics of 500 ns. The root mean squared deviation (RMSD) of the transmembrane domain stabilized after $\sim$ 100 ns, while the whole system RMSD stabilized after $\sim$ 200 ns (in Figure 6.5 are presented the value of the RMSD for Cx26WT and Cx26V84L models).

In order to include the molecules we want to study in our molecular dynamics simulations, we need the structure and the parametrization, *i.e.* partial charge, bond stretching, angle bending, torsional twisting, van der Waals (see Appendix B), of these molecules. They are well known molecules and their structures are available online [171–173], but the parameters for Amber force field are not published. Starting from an optimized structure of the molecules, *Gaussian* software [174] was used to perform a quantum chemistry calculation and obtain the spatial position of the single atoms and the electronic charge distribution

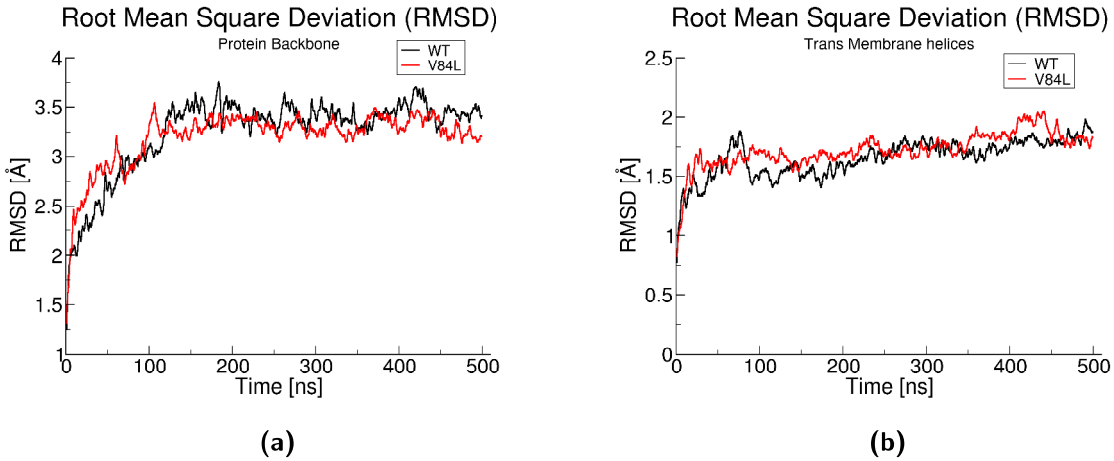

Figure 6.5: Plots of root mean square deviation ($RMSD$) vs time. The black traces correstomd to Cx26WT model, whereas red traces correspond to Cx26V84L model. **(left)** The traces are computed on the whole protein. **(right)** The traces are computed on residues in the membrane region (residue from 19 to 40, 76 to 96, 132 to 153 and 190 to 210).

of the molecule. With this information we were able to compute all the Aber forcefield compatible parameters we needed using the Amber package *Antechamber* [175, 176]. For compute the parameters of our molecules we used the *General Amber Force Field 2* (GAFF2) for the atom types and *Restrained Electrostatic Potential* (RESP). Using this protocol, we obtain reliable parameters for IP_3, ATP and *glucose* molecules that are compatible with the classical Amber force field we use for proteins, water and ions.

In order to study the permeability of the Cx26WT and Cx26V84L hemichannels to these molecules, we compute the Free energy barriers (represented by the PMFs) that the molecule needs to overcome using the Umbrella Sampling technique seen in the previous Section (see also Appendix C.3). As mentioned, to be able to perform this type of simulation we needed to build the windows in which we were going to fix our molecule along the chosen reaction coordinate. Since we were going to use the pore axis (that lies along the z axis of our system) as reaction coordinate ξ, to build the US windows we needed to pull the molecule through the pore axis using a SMD simulation.

We performed this simulation forcing the molecule at the centre of the pore and fixing the alpha-carbon of the TM3 and TM4 of the connexon in order to avoid dragging the pore during the simulation (see Figure 6.3). The elastic constant k of the linear spring used for the pull was set at $2000\,\mathrm{kJ\,mol^{-1}\,nm^{-2}}$ and zero resting length. The other end of the spring shifted along the pore axis at a constant velocity of $1.0\,\mathrm{nm\,ns^{-1}}$. The simulations spanned a total of 6.0 nm for each system in order to pull the molecule from the cytoplasmic mouth of the hemichannel to the extracellular side.

6.2.1 Unitary permeability to IP_3

The IP_3 molecule (Figure 6.6) is a secondary messenger molecule used in signal transduction and lipid signalling in biological cells. IP_3's main functions are to mobilize Ca^{2+} and to regulate cell proliferation and other cellular reactions that require free calcium [177]. In the nervous system, IP_3 serves as a second messenger [178]. Moreover, dysfunctions in the

IP_3-mediated Ca^{2+} release are be shown to be related to Alzheimer's and Huntington's disease.

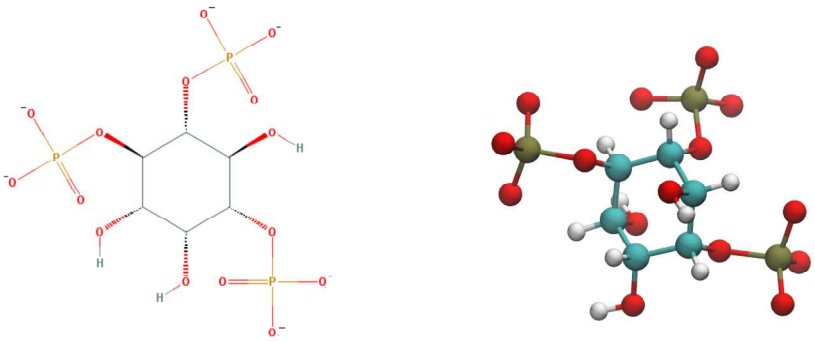

(a) (b)

Figure 6.6: Inositol trisphosphate (IP_3). IP_3 is an organic molecule with a molecular mass of 420.10 g/mol. Its empirical formula is $C_6H_{15}O_{15}P_3$. It is composed of an inositol ring with three phosphate groups bound at the 1, 4, and 5 carbon positions, and three hydroxyl groups bound at positions 2, 3, and 6.

After we inserted the IP_3 molecule in correspondence of the cytoplasmatic mouth of the Cx26WT and V84L hemichannels, we performed a SMD to generate the initial configuration for the windows of the US (as described in the Section above). Every window was simulated for 12 ns and we checked the convergence of the consequent PMF every 2 ns of simulation (Figure 6.7). As can be seen from the Figure 6.7, after 12 ns of simulation the PMF seems to converged.

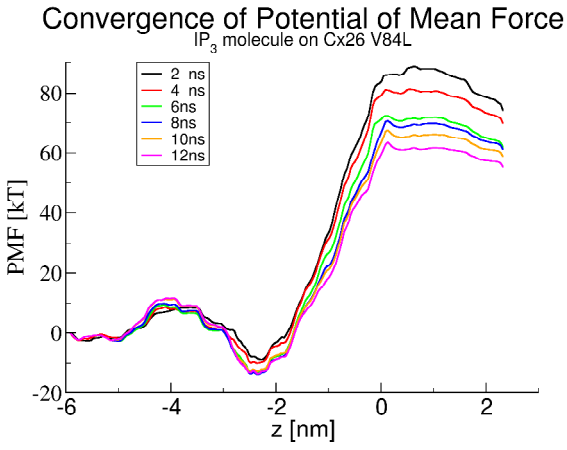

Figure 6.7: Convergence of PMF for the passage of IP_3 molecule.

To test this hypothesis, we performed a second US using the same starting configuration. The preliminary results for the PMF of the passage of an IP_3 molecule through a Cx26WT and Cx26V84L hemichannel, reported in Figure 6.8, show that for two simulations started from the same starting configuration, we obtain different results. From a visual inspection we saw that, for almost every windows of the US, in the first nano seconds of simulation,

the IP_3 molecule got trapped in a minimum of energy and was not able to sample all the possible configurations. This means that a longer simulation time would not be sufficient to improve the convergence of the PMF and we had to find a different way to improve the sampling of our simulations. As a preliminary result we simply repeated the US simulation twice for both Cx26WT and Cx26V84L hemichannels. Then, since the PMFs represent the energy that the IP_3 molecule has to spend in order to pass through the hemichannel, we decided to select the smallest PMFs for both Cx26WT and Cx26V84L hemichannel. These PMFs represent the more convenient path (that we were able to sample) for the passage of the IP_3 molecule.

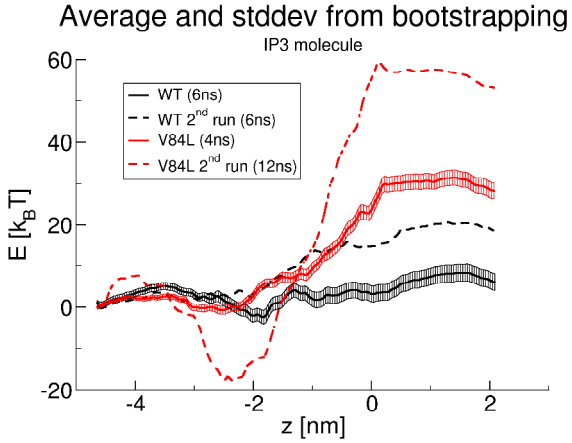

Figure 6.8: PMF for the passage of IP_3 molecule.

6.2.2 Unitary permeability to *ATP* and *glucose*

We start this section with a brief introduction the *ATP* and *glucose* molecules.

Adenosine triphosphate (*ATP*) (Figure 6.9) is a nucleoside triphosphate, a small molecule used in cells as a coenzyme. It is often referred to as the "molecular unit of currency" of intracellular energy transfer. ATP transports chemical energy within cells for metabolism. Most cellular functions (synthesis of proteins, synthesis of membranes, movement of the cell, cellular division) need energy in order to be carried out. The ATP is the molecule that carries energy to the place where the energy is needed. When ATP breaks into *ADP* (Adenosine diphosphate) and *Pi*, the breakdown of the last covalent link of phosphate (a simple $-P04$) liberates energy that is used in reactions where it is needed. Metabolic processes that use ATP as an energy source convert it back into its precursors. ATP is therefore continuously recycled in organisms: the human body, which on average contains only 250 *grams* of ATP, turns over its own body weight equivalent in ATP each day [179]. The structure of this molecule consists of a purine base (adenine) attached by the $9'$ nitrogen atom to the $1'$ carbon atom of a pentose sugar (ribose). Three phosphate groups are attached at the $5'$ carbon atom of the pentose sugar. It is the addition and removal of these phosphate groups that inter-convert ATP, ADP and AMP. When ATP is used in DNA synthesis, the ribose sugar is first converted to deoxyribose by ribonucleotide reductase. ATP was discovered in 1929 by Karl Lohmann [180], and independently by

Cyrus Fiske and Yellapragada Subbarow of Harvard Medical School [181], but its correct structure was not determined until some years later.

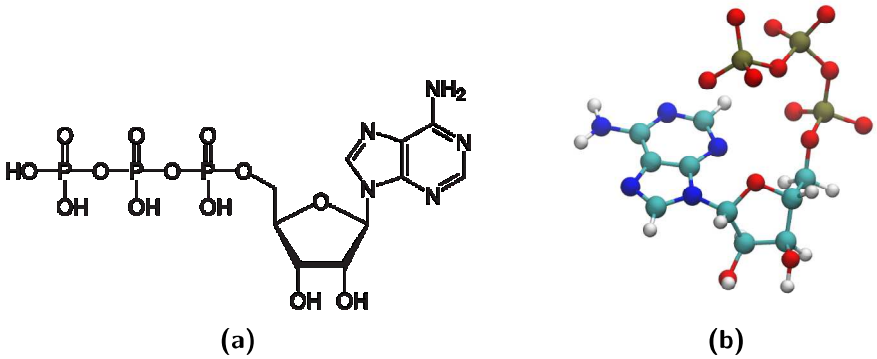

Figure 6.9: Adenosine triphosphate (ATP).

D-Glucose (Figure 6.10) is a sugar with the molecular formula $C_6H_{12}O_6$. Glucose circulates in the blood of animals as blood sugar. Glucose is made during photosynthesis from water and carbon dioxide, using energy from sunlight. The reverse of the photosynthesis reaction, which releases this energy, is an important source of power for cellular respiration. Glucose is stored as a polymer, in plants as starch and in animals as glycogen, for times when the organism will need it. With six carbon atoms, it is classed as a hexose, a sub-category of monosaccharides. D-glucose is one of the 16 aldohexose stereoisomers. The D-isomer (D-glucose), also known as dextrose, occurs widely in nature, but the L-isomer (L-glucose) does not. In 1747, Andreas Marggraf was the first to isolate glucose. It is on the World Health Organization's List of Essential Medicines, the most important medications needed in a basic health system.

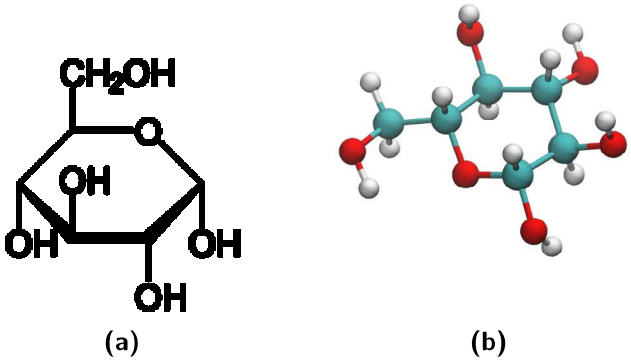

Figure 6.10: *Glucose* molecule.

Computational results

Now we want to show the preliminary results obtained for the passage of ATP and *glucose* through a Cx26WT and Cx26V84L hemichannels. From this simulations we would like to see the differences on the passage of the molecule (ATP or *glucose*) through the WT and

V84L mutant hemichannel. In the same way as the IP_3 molecule, we inserted the molecules in correspondence of the cytoplasmatic mouth of the Cx26WT and V84L hemichannels (for a total of four different models) and we performed a SMD to generate the initial configuration for the windows of the US. Also for these molecules, every window was simulated for 12 ns. The preliminary results obtained from these simulations are shown in Figure 6.11 and Figure 6.12 for ATP and *glucose*, respectively.

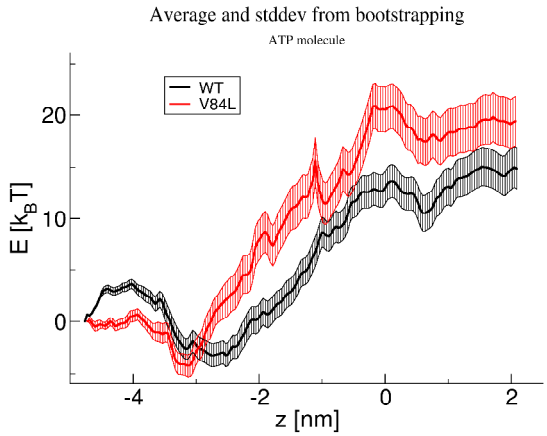

Figure 6.11: PMF for the passage of ATP molecule.

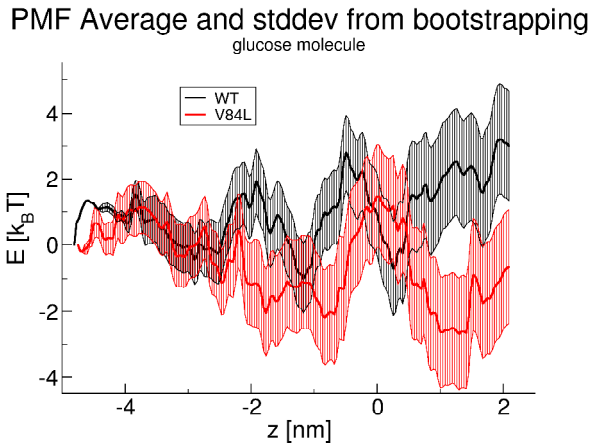

Figure 6.12: PMF for the passage of $D-Glucose$ molecule.

This preliminary results shown a big difference between the free energy profiles of the ATP molecule, whereas the two free energy profiles for the *glucose* are essentially the same.

6.2.3 Molecular insight

In order to understand the differences between the Cx26T and Cx26V84L models, we performed a molecular analyses of the equilibrium molecular dynamics. First, we found a significant difference in the diameter of the pore at the level of residues 84 (in the second

transmembrane helices, Figure 6.13) and residues 44 (in the first extracellular loop, Figure 6.14).

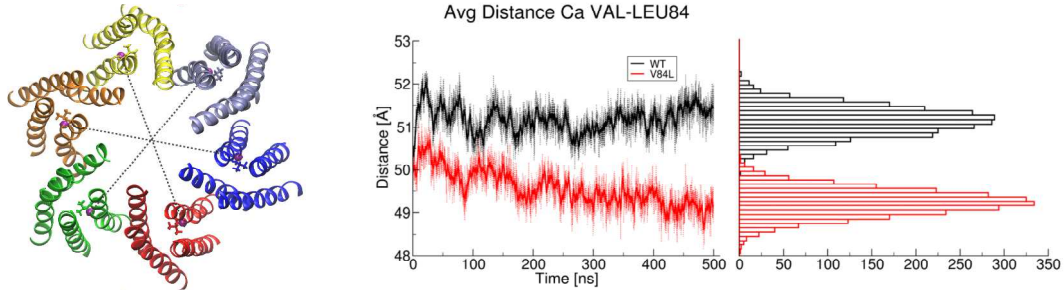

Figure 6.13: Diameter of the pore for residues 84. Pannel A shows a cartoon representation of Cx26 where we highlight TM1, TM2 and EL1 in blue, red and green, respectively. Residues 84 are shown in VdW representation. Pannels B and C reports the average distances between pairs C-alpha carbon of residues 84 in opposite connexin protein.

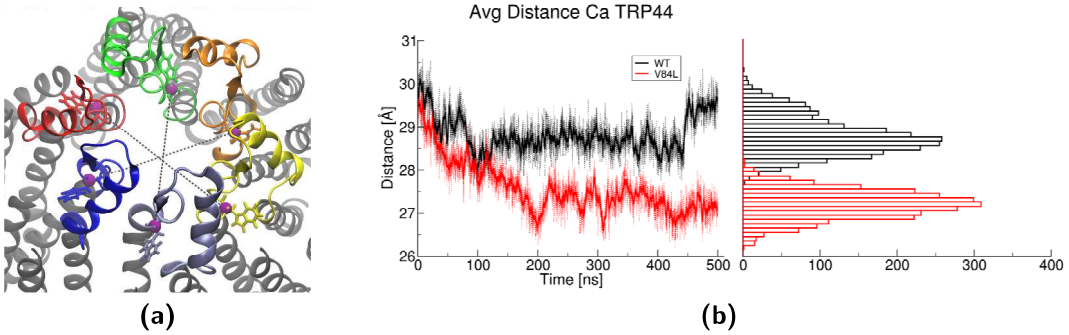

Figure 6.14: Diameter of the pore for residues 84 and 44. Pannel A shows a cartoon representation of Cx26 where we highlight TM1, TM2 and EL1 in blue, red and green, respectively. Residue 84 and 44 are shown in VdW representation. Pannels B and C reports the average distances between pairs C-alpha carbon of residue 84 and 44 in opposite connexin protein.

Then, computing the radius vs the axis of the two hemichannels (Figure 6.15) we obtained two profiles with a large difference in the cytoplasmatic mouth and other two small, but significant, differences at the level of the residues 44 and 60.

6.2.4 Comments

In this chapter we computed the unitary permeability of Cx26WT and Cx26V84L hemichannels to small molecules using the Umbrella sampling technique. The preliminary results we obtained show a problem with the convergence of the PMFs due to the sampling challenging.

In this chapter we computed the unitary permeability of small molecules in a Wild Type and V84L mutant hemichannel using the Umbrella sampling (US) technique. We are still working on this project and we have presented preliminary data that shows how challenging it is to obtain convergence in the free energy profiles. Using the US technique we are not sure about the convergence of the free energy profile computed, but we can

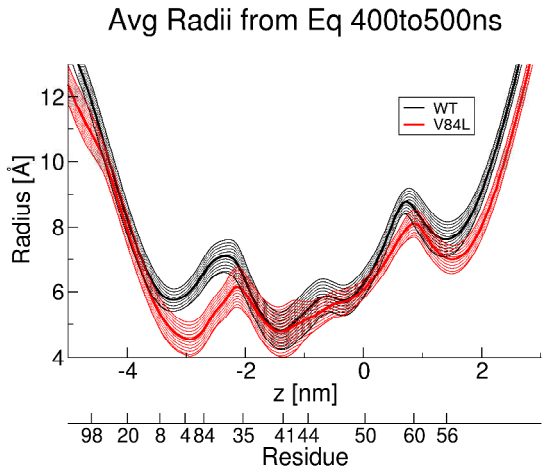

Figure 6.15: Radii of the Cx26 WT and V84L connexon conputed with hole2. Average radius of the Cx26 WT and V84L connexons.

say that it represents one of the possible paths that the molecule could cover during the passage through the hemichannel. Nevertheless, in all the profiles we computed, we found big differences in the unitary permeability to ATP molecules and IP_3 molecules and no differences in the unitary permeability of glucose. From a molecular insight performed in the equilibrium molecular dynamics, we were able to find significant differences between the Cx26WT and Cx26V84L hemichannel models. First, we found a significant difference in the diameter of the pore at the level of residues 84 (in the second transmembrane helices) and residues 44 (in the first extracellular loop). Then, computing the radius vs the axis of the two hemichannels we obtained two profiles with a significant difference in the cytoplasmatic mouth and other two small, but significant, differences at the level of the residues 44 and 60.

Part III

Discussion

In this thesis, we explored the possibility of computing measurable quantities, like conductance, unitary permeability and variables related with the equilibrium properties, for a family of membrane channels: the junctional channels composed of connexin proteins, starting from fully atomistic Molecular Dynamics simulations. In order to understand what the molecular mechanisms are that underlie the permeation in these complex system, we focused our attention on a junctional channel composed of Wild Types Cx26 (Cx26WT), a complex system made of an antibody docked on a Cx26WT hemichannel and three of its natural variations, the mutant C169Y, M34T, and V84L, which lead to pathogenical consequences at the organ of Corti, where Cx26 is expressed, resulting in genetic deafness.

Starting from the crystal structure and a previously published atomistic model, we generated analogous models for the Cx26WT and its mutants and equilibrated them by means of classical Molecular Dynamics simulations. Through the structure analysis of the equilibrium molecular dynamics we were able to predict that C169Y mutation hinders the docking of Cx26 hemichannels by altering protein structure in the extracellular domain. In that analysis we found an average displacement of two of the seven amino acids that are responsible for hemichannel docking, but in some protomers of the connexon, the structure remained virtually unaltered. We associated this discrepancy with the relative shortness of the simulated time span. In fact, we performed an equilibrium simulation 100 ns long that could be long enough to re-equilibrate a protein structure in the proximity of a local energy minimum and reach a stable configuration of the model, but not enough to see a complete configuration change that would lead the model to a different, more stable state in which all six connexins show the same configuration. Nonetheless, our results strongly suggest the extracellular domain of Cx26 is compromised by the C169Y mutation and we were able to predict, and then confirm with experimental data, the impaired docking of two mutant connexons.

We also studied out-of-equilibrium properties of the channel: conductance and unitary permeability. To study the conductance we compared two different methods: the first was based on a "brute force calculation"", and realized by imposing an external electrical forcefield E and simply counting the ions that passed through the channel in a certain period of time; the second, named steered molecular dynamics (SMD), was realized by forcing the ion to move across the pore and calculating the potential mean force (PMF) it felt during the motion. Jarzynski inequality assures us that the PMF can be regarded as a good approximation of free energy. To compute the unitary permeability of small molecules, however, we used the Umbrella Sampling (US) method, which were a set of simulations performed with the molecule fixed in different positions along the reaction coordinate (the axis of the pore) but, in order to improve the sampling, it was left free to move on the space perpendicular to the reaction coordinate. From this set of simulations we calculated the PMF for the passage of the molecule through the hemichannels.

Although a quantitative prediction of measurable quantities is very complex, due to the big differences in size scale and time scale between what can be simulated and the microscopic world of a living cell, the comparison between two systems that are very close from an atomistic point of view but result in very different behaviour,can shed some light on how permeation of ions actually happens at the level of a single channel.

We applied the SMD method to study the potassium permeation in a Wild Type and a M34T mutant hemichannel. The approach that we followed was to compare the free energy of the permeation of a potassium ion in the two different systems. The free energy can in fact be directly related to the conductance: using *Eyring* transition state theory, we

know that the conductance must be proportional to the exponential of the total free energy gap. Assuming that the proportionality is constant, is related to the diffusion coefficient of the ion, and does not depend on the free energy profile itself, we can calculate the ratio between two conductances. A more refined theory is based on the *Smoluchowski* equation: we compute the MFPT using the free energy profile plus an energy given by a differential of potential dependent on position z. Then, assuming that a single ion can occupy the channel, we can relate that time with the flux J of ions through the pore. The net flux of one ion type gives rise to a current that is linearly dependent on the difference of potential added to the free energy. The proportional constant between current and difference of potential is the conductance of the channel assuming that the ions pass one at a time. The conductance ratio predicted by our models is 18 : 1 and 10 : 1 for Cx26M34T with the Eyring transition state theory and theory based on Smoluchowski equation, respectively. These results are both in agreement with the experimental value (11 : 1). It is interesting to note that the most important difference between the two profiles arise around the position of methionine 34, indicating that what we observe is a genuine effect of the mutation. What happens at the molecular level, when methionine 34 is mutated into a threonine, is that the bond that held the N-terminal helices together with the first transmembrane helix of the adjacent connexin is lost. This results in an increased mobility of N-terminal helices, that are no longer attached to the transmembrane helical bundle, and that are free to protrude into the pore. To test this latter hypothesis, we performed a set of simulations where we imposed an external force that drove the helices inside the pore, both to the WT and the M34T mutant. These simulations indicate that the NTHs in the Cx26M34T mutant are less bound to the channel wall (Figure 5.25) and we speculate that, for this reason, the gating mechanism is compromised, as proposed in [164].

The "brute force" method was applied to two different systems. First we use it to compute the ratio (in agreement with the experimental data) of the current flowing through a human Connexin 26 hemichannel with and without a human antagonist antibody for Cx26 hemichannels, nevertheless, we were not able to produce a quantitative measure of the current flowing through one hemichannel. This is because, although the resulting voltage is independent of the system size and solely depends on $E \cdot L_z$, there are a lot of different factors that lead to systematic errors. In particular we are working with non-equilibrium properties that are more sensitive to the finite size of the system due to changes in the resistance and long-range dissipative effect [128]. This leads to a clear dependence on the size of the system for the current that flow through a membrane pore. Another problem is related to the time-scale of the simulation. For a full atom system with more than 2.5×10^5 atoms, we can reach simulation times of the order of 500 ns. This time-scale is extremely small compared to the record times in the patch clamp electrophysiology experiments (on the order of ms). For this reason we also applied the "brute force" method to a Coarse Grained (CG) model we built thanks to a collaboration with Institut Pasteur de Montevideo. The aim of use a CG model is to reach time-scale of simulations that are prohibitive with the all atom (AA) systems. In addition to the preliminary results on the conductance studies, from the analyses of these simulations we notice a change in the configuration of our hemichannel that occurs over 5 µs. This is an event that we could not see with the AA model due to the time-scales involved. After the electric field was turned on, we observed a widening of the pore and consequently an increase in the passage of the ions through the hemichannel. The most remarkable changes were at the level of the residue 41 and the N-terminal helices. The former is the charged residue in the narrowest

part of the pore and is considered to be responsible for the straight slope in the free energy potential for the passage of a molecule through the pore. The latter is considered to be an essential component for fast gating. This is a very interesting aspect that will be explored in future work.

Finally we computed the unitary permeability of small molecules in a Wild Type and V84L mutant hemichannel using the US method. We are still working on this project and we have presented preliminary data that show how challenging it is to obtain convergence in the free energy profiles. Using the US technique we are not sure about the convergence of the free energy profile computed, but we can just say that it represents one of the possible paths that the molecule can cover during the passage through the hemichannel. From a molecular insight performed in equilibrium molecular dynamics, we were able to find significant differences between the Cx26WT and Cx26V84L hemichannel models. First, we found a significant difference in the diameter of the pore at the level of residues 84 (in the second transmembrane helices) and residues 44 (in the first extracellular loop). Then, computing the radius vs the axis of the two hemichannels we obtained two profiles with a large difference in the cytoplasmatic mouth and other two small, but significant, differences at the level of the residues 44 and 60.

In conclusion, we found a good theory to compute the conductance of a channel for an ion starting from their free energy profile. Then we applied this model to a GJ of connexins 26 WT and M34T and achieved a conductance ratio in close agreement with the experimental data and we found an explanation for the difference of conductance between the two channels.

Moreover, we validated a computational method to compute the conductance starting from an out-of-equilibrium molecular dynamics simulation using it to compute a conductance ratio (in close agreement with the experiment) between Cx26WT and a complex system made of Cx26WT and a human antagonist antibody for Cx26. We applied this method also to a CG model of Cx26WT obtaining a change in the configuration of our hemichannel that occurred after 5µs. We hypothesise that this represents a more conductive configuration of the hemichannel that we were not able to see with all-atom model due to the time-scale involved. This is a very interesting result that will be analysed in future experiments.

In closing, the computing of the unitary conductance with molecular dynamics is extremely challenging and we are currently analysing the results. The preliminary results show a problem with the convergence of the energy profiles for the passage of the molecules. Nevertheless, in all the profiles we computed, we found big difference in the unitary permeability to ATP molecules and IP_3 molecules and no differences in the unitary permeability of *glucose*.

Part IV

Appendices

Appendix A

Structure and classification of polipeptides

A.1 Proteins and amino acids

Proteins are a class of biochemical molecules involved in many cellular processes, playing fundamental roles in transport, structure, enzymatic activity and more. They are natural eteropolymers consisting of amino acid units that form the basis for the major structural components of animal and human tissue.

Amino acids, the monomeric units, are composed by an amino group, the so-called $\alpha - Carbon$ atom (C^{α}), a *carboxylic group* (in which carbon and oxygen will be labeled respectively as C^{I} and O from now on) and a *residue*. Residue are a family of chains which link to the $\alpha - Carbon$ and characterize the specific kind and properties of the amino acid. Thus, classification of amino acids is based on the residue and on its chemical-physical properties. Although there are hundreds of know amino acids, just a little part of them (about twenty) is actually found in proteins.

Proteins synthesis takes place in ribosomes, where the genetic information stored in DNA is copied to a messenger RNA (mRA). The amino acids are attached to transfer RNA (tRNA) molecules, which enter one region of the ribosome and bind to the messenger RNA sequence. The attached amino acids are then joined toghether. The ribosome move along the mRNA, ""reading" its sequence and producing a chain of amino acids. Three bases in the DNA codify for a single amino acid. Although a three bases code can potentially produce sixty-four different strings, the code is redundant, i.e. several code stand for the same amino acid. This is believed to play a role in making DNA code less sensitive to random mutation. Only twenty amino acids are coded into the genetic code, as drawn in table A.1. Although it is possible to find some ""non-standard" residues in proteins due to modifications occurring after code translation in the ribosome and which may depend on amino acid type and position, we will limit any further analysis and discussion on the twenty standard amino acids. They are listed in figure A.2. In the two most widely used standards, each amino acids is associated with a one letter or three letter code.

They are usually divided in four classes depending on polarity an charge:

1. Negatively charged amino acids:

    - Aspartate (Asp, D)

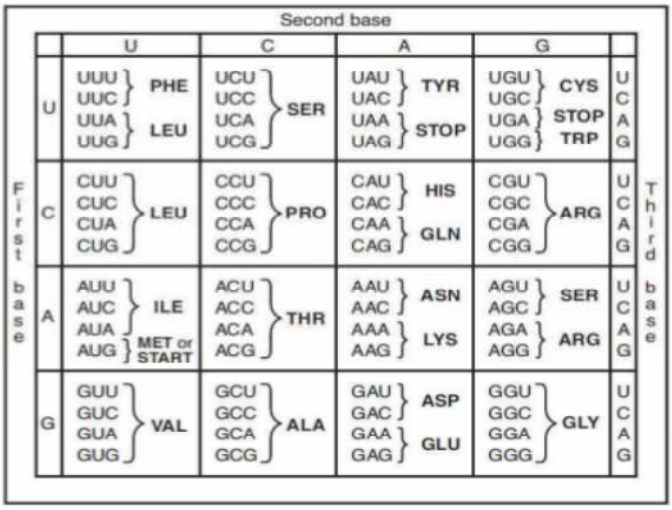

Figure A.1: Genetic code table RNA codons and amino acids for which they code

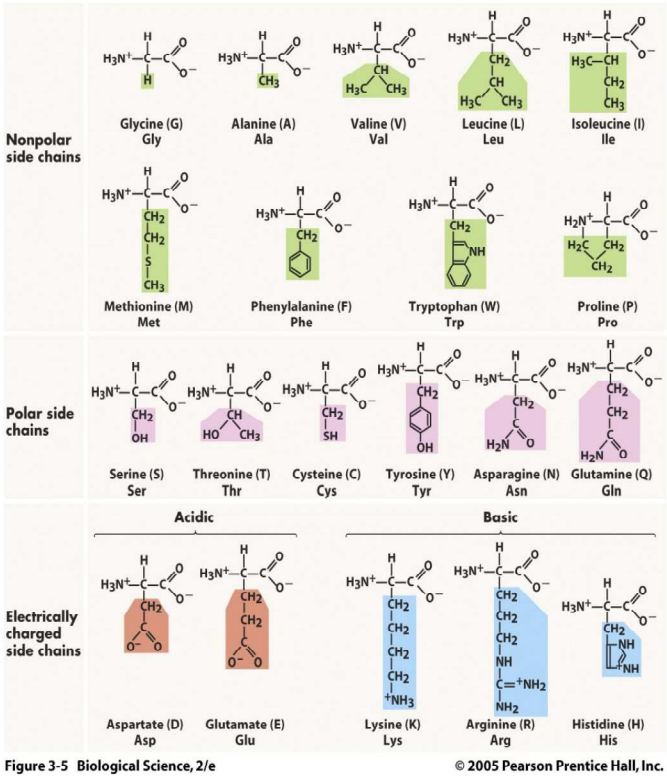

Figure A.2: The twenty standard amino acids The residues are highlight with colors that differ for different properties.

- Glutamic acid (Glu, E)

2. Positively charged amino acids:

- Lysine (Lys, K)
- Arginine (Arg, R)
- Histidine (His, H)

3. Polar amino acids:
    - Asparagine (Asn, N)
    - Cysteine (Cys, C)
    - Glutammine (Gln, Q)
    - Serine (Ser, S)
    - Tyrosine (Tyr, Y)
    - Thrconinc (Thr, T)
4. Apolar amino acids:
    - Alanine (Ala, A)
    - Phenalanine (Phe, F)
    - Glycine (Gly, G)
    - Isoleucine (Ile, I)
    - Leucine (Leu, L)
    - Methionine (Met, M)
    - Proline (Pro, P)
    - Tryptophan (Trp, W)
    - Valinc (Val, V)

With the exception of glycine, all amino acids are chiral molecules. Of note, in all biological proteins only L-form is present.

The amino group of one amino acid can react with the carboxylic group of another amino acid releasing a water molecule and forming a bond which is called *peptide bond*. The C^{α}, C^{I} and N thus form a chain, and they are named *backbone* of the protein.

The energy of the bond formation depends on the amino acids involved, and it appears to exist a sort of nucleation on the formation, thus making easier to bind a amino acid to a chain rather than to a single amino acid. Typical values are on the order of a fraction to some Kcal/mol [182].

Appendix B

Classical Molecular Dynamics

Each Molecular Dynamics simulation requires as input a set of initial coordinates and, optionally, initial velocities of all particles involved. Coordinates are often obtained by X-ray crystallographic data, or by quanto-mechanics simulations. If the starting configuration is far from equilibrium, the forces may be excessively large and the MD simulation may fail. In those cases, a robust *energy minimization* is required.

When the input is read, the interaction potential is calculated as a function of atom positions. Then the forces are calculated as the gradient of the potential, thus making possible to numerically solve the Newton's equation of motion for a small step of time. Once the new coordinates have been calculated is possible to recalculate the potential and reiterate the process to obtain another step. In figure B.1 the process is described schematically.

In classical molecular dynamics every atom is considered as a single object. There are many different programs developed to deal with this kind of simulations, but the way interactions are treated is often very similar. Interactions are parametrized according to a so-called *force field*. Different force fields parametrize them in different ways, and are developed according to different methods.

Interactions are usually classified as bonded and non-bonded. The non-bonded are basically electromagnetic and Van der Waals interactions. On the other side, the bonded interactions consist of a bond stretching, a bond angle, a dihedral (or torsional angle) and an improper dihedral term. Improper dihedrals are meant to keep some groups (e.g. aromatic rings) planar, or to prevent molecules from flipping over to their mirror images. Bonded interaction parameters are depicted schematically in figure B.2.

In this work the AMBER [113] and GROMACS [112] program suites and the amber03 force field were used. The different suites have been chosen only for technical reasons: some simulations technologies are more easily implemented in one or another package. What is important is not to change the force field, which determine the dynamics.

The basic force field implemented in AMBER has the following form, which is about the simplest functional form that preserves the essential nature of molecules in condensed phases:

THE GLOBAL MD ALGORITHM

1. Input initial conditions
Potential interaction V as a function of atom positions
Positions r of all atoms in the system
Velocities v of all atoms in the system
⇓

repeat 2,3,4 for the required number of steps:

2. Compute forces
The force on any atom

$$F_i = -\frac{\partial V}{\partial r_i}$$

is computed by calculating the force between non-bonded atom pairs:

$$F_i = \sum_j F_{ij}$$

plus the forces due to bonded interactions (which may depend on 1, 2, 3, or 4 atoms), plus restraining and/or external forces. The potential and kinetic energies and the pressure tensor are computed.
⇓

3. Update configuration
The movement of the atoms is simulated by numerically solving Newton's equations of motion

$$\frac{d^2 r_i}{dt^2} = \frac{F_i}{m_i}$$

⇓

4. if required: Output step
write positions, velocities, energies, temperature, pressure, etc.

Figure B.1: Molecular dynamics algorithm

$$\begin{aligned} V(r) = & \sum_{bonds} K_b(b - b_0)^2 \\ & + \sum_{angles} K_\theta(\theta - \theta_0)^2 \\ & + \sum_{dihed} (V_n/2)(1 + cos[n\phi - \delta]) \\ & + \sum_{nonb} (A_{ij}/r_{ij}^{12}) \overset{83}{-} (B_{ij}/r_{ij}^6) + (q_i q_j / r_{ij}) \end{aligned} \tag{B.1}$$

As one can note from the equation, the bonds and angles terms are treated in a harmonic approximation, while a Lenard-Jones potential is used for the Van der Waals interaction. As long as one does not have the need to take account of very specific effects such as atomic polarization this form is either sufficiently accurate and computationally efficient.

The parameters as K_b, b_0, etc. are derived mostly from quanto-mechanics calculations, and are refined to fit at best some experimental verified properties (for example to give the correct α-helix to coil ratio in test proteins).

In addition to the interactions in the force-field, it is possible to define some constraints on the atoms positions, distances, angles or dihedral.

B.1 Boundary conditions

Since the size of the simulated system usually does not exceed a few nanometers per direction one must consider what happens at the boundaries. The classical way to minimize edge effects in a finite system is to apply periodic boundary conditions. The atoms of the system to be simulated are put into a space-filling box, which is surrounded by translated copies of itself. Thus there are no boundaries of the system; the artifact caused by unwanted boundaries in an isolated cluster is now replaced by the artifact of periodic conditions. If the system is crystalline, such boundary conditions are desired (although motions are naturally restricted to periodic motions with wavelengths fitting into the box). In the case of non-periodic systems, such as liquids or solutions, the periodicity by itself is an artifact that causes errors. However, errors induced are usually expected to be less severe than ones resulting from an unnatural boundary with vacuum.

Non-bonded short ranged interactions are calculated using the minimum image convention, i.e. only the closest images of a particle are considered.

Moreover, periodic boundary conditions make possible the use of fast grid searching algorithms, with a significant gain in performance.

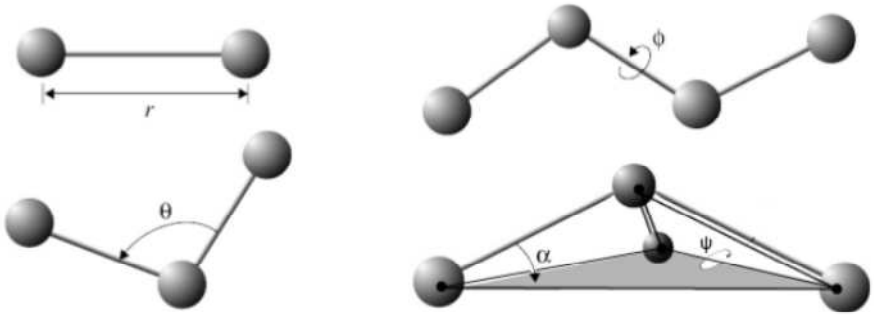

Figure B.2: Bonded interactions parameters. Here, r represents the bond stretching parameter, θ the bond angle, ϕ the torsional angle and ψ the improper dihedral parameter. The latter is the angle between the two planes shown by the black line. In some force fields, this out-of-plane situation is parametrized by the distance of the central atom from the plane defined by the three surrounding ones instead of the angle above.

B.2 Kinetic energy and temperature

The temperature is given by the total kinetic energy of the N-particle system:

$$E_{kin} = \frac{1}{2}\sum_{i=1}^{N} m_i v_i^2$$

From this equation the absolute temperature T can be computed using:

$$\frac{1}{2} N_{df} k_B T = E_{kin}$$

where $k_B = 1.38065 \cdot 10^{-23} J \cdot K^{-1}$ is the Boltzmann's constant and N_{df} is the number of degrees of freedom which can be computed from:

$$N_{df} = 3N - N_c - N_{com}$$

where N_c is the number of constraints imposed on the system and $N_{com} = 3$. The three additional degrees of freedom represented by N_{com} must be removed because the three center-of-mass velocities are constants of the motion, which are usually set to zero. This because there is usually no net external force acting on the system and the center-of-mass velocity should remain constant. In practice, however, the update algorithm introduces a very slow change in the center-of-mass velocity (due to the finite precision of the floating point numbers), and therefore in the total kinetic energy of the system. If such changes are not quenched, an appreciable center-of-mass motion can develop in long runs, and the temperature will be significantly misinterpreted.

B.3 Temperature coupling

While direct use of molecular dynamics gives rise to the micro canonical ensemble (or NVE: constant particle number, constant volume, constant energy), most of the times the canonical ensemble (NVT: constant particle number, constant volume, constant temperature) is more appropriate to simulate realistic biological systems. In order to perform NVT simulations, temperature is controlled by a virtual thermostat. There are several temperature coupling algorithms:

- Berendsen weak coupling scheme [114]: each particle velocity is rescaled every step by a single scaling factor. This is the computationally less expensive coupling, although it can introduce some artifacts. There are two major issues using the Berendsen thermostat. First, it does not assure that temperature is the same in every part of the system. Second, some subtle problems arise, since it has the tendency to convert all the kinetic energy of the system to center of mass motion, thus violating the equipartition theorem (this phenomenon has been named the "flying ice-cube" [183]).
- Andersen coupling [184]: velocities are randomized to a distribution corresponding to the desired temperature at a fixed interval of steps, such as the particles undergo to "imaginary collisions". Here, a too high a collision rate will slow down the speed at which the molecules explore configuration space, whereas too low a rate means that the canonical distribution of energies will be sampled slowly.

- Langevin dynamics: a small viscous term and a temperature-dependent noise term is added to the newton equation of motion, i.e. $m_i\ddot{x}_i = F_i(t) - m_i\gamma\dot{x}_i + R_i$ with R_i satisfying $\langle R_i(t)R_j(s)\rangle = 2\gamma k_B T m_i \delta_{ij}\delta(t-s)$. Here, γ is the friction constant. When $1/\gamma$ is large compared to the time scales present in the system, one could see stochastic dynamics as molecular dynamics with stochastic temperature-coupling. This is a more robust but slower method.

B.4 Pressure computation

To compute pressure tensor the virial is used, and a derivation follows.

Consider a system of N interacting point masses. The position of the i-th point mass is indicated as $\boldsymbol{x}_i$ and its linear momentum as $\boldsymbol{p}_i = m_i\dot{\boldsymbol{x}}_i = m_i\boldsymbol{v}_i$. The system is a small portion of fluid, small enough for all macroscopic gradients to be zero, and large enough to represent a homogeneous phase.

Let us then consider the quantity

$$\langle \frac{d}{dt}\sum_i \boldsymbol{x}_i \otimes \boldsymbol{p}_i \rangle$$

where the symbol $\otimes$ indicates a direct product of two vectors, i.e.

$$(\boldsymbol{x}_i \otimes \boldsymbol{p}_i)^{\alpha\beta} = \boldsymbol{x}_i^{\alpha} \cdot \boldsymbol{p}_i^{\beta}.$$

and $\langle\cdot\rangle$ indicates an ensemble average, or a time average over a time span long enough to smooth out fluctuations, and short enough to assume that the macroscopic flow is stationary. The existence of such a time scale is a central assumption of the theorem. The sum is over all particles in our control volume, i.e. particles leaving the control volume are from that moment on left out of the sum, and particles entering the control volume will from that moment on contribute to the sum. Since in this case $\sum_i \boldsymbol{x}_i \otimes \boldsymbol{p}_i$ is a bounded quantity, with a well defined average, the average of its time variation must be zero.

Indicating with $\boldsymbol{f}_i$ the force acting on the i-th particle, and knowing that $\frac{d}{dt}\boldsymbol{p}_i = \boldsymbol{f}_i$, we can write

$$\begin{aligned} \langle \frac{d}{dt}\sum_i \boldsymbol{x}_i \otimes \boldsymbol{p}_i \rangle &= \langle \sum_i \boldsymbol{v}_i \otimes \boldsymbol{p}_i \rangle + \langle \sum_i \boldsymbol{x}_i \otimes \boldsymbol{f}_i \rangle \qquad \text{(B.2)} \\ &\Downarrow \\ 0 &= 2\bar{\mathcal{T}} + \bar{\mathcal{W}}. \qquad \text{(B.3)} \end{aligned}$$

Here $\mathcal{T} = \frac{1}{2}\sum_i \boldsymbol{v}_i \otimes \boldsymbol{p}_i$ is the *kinetic tensor* and $\mathcal{W} = \sum_i \boldsymbol{x}_i \otimes \boldsymbol{f}_i$ is the *virial tensor*, while the bar indicates averaging.

We assume that forces acting on the system can be divided between an internal component from the mutual interaction of particles inside the volume and an external one due to the interaction with all the particle outside and external fields. We can then write

$$\boldsymbol{f}_i = \boldsymbol{f}_i^{int} + \boldsymbol{f}_i^{ext}$$

and thus divide the virial tensor on the respective components $\bar{\mathcal{W}} = \bar{\mathcal{W}}^{int} + \bar{\mathcal{W}}^{ext}$.

Let us now consider $\mathcal{W}^{ext}$. Let us assume we can divide the external forces in a volume component and a surface one. We can thus write

$$\mathcal{W}^{ext} = \int_{\Omega} \boldsymbol{x} \otimes \boldsymbol{b}\rho \, dV + \oint_{\partial\Omega} \boldsymbol{x} \otimes \boldsymbol{t} \, dA \tag{B.4}$$

where $\boldsymbol{b}$ is the body force per unit mass acting on the whole control volume Ω and $\boldsymbol{t}$ is the force acting on the infinitesimal surface dA. In terms of the stress tensor $\boldsymbol{\sigma}$,

$$\boldsymbol{t} = \boldsymbol{\sigma}\hat{\boldsymbol{n}}$$

where $\hat{\boldsymbol{n}}$ is the vector normal to dA.

Inserting the last relation into B.4 and applying divergence theorem, we thus obtain

$$\bar{\mathcal{W}}^{ext} = \int_{\Omega} \boldsymbol{x} \otimes \boldsymbol{b}\rho + \bigtriangledown_x \cdot (\boldsymbol{x} \otimes \boldsymbol{\sigma}) \, dV \tag{B.5}$$

$$= \int_{\Omega} \boldsymbol{\sigma}^T + \boldsymbol{x} \otimes (\boldsymbol{b} + \bigtriangledown_x \cdot \boldsymbol{\sigma}) \, dV \tag{B.6}$$

Now we assume that there are no external body forces and the derivative term of the stress tensor is negligible. Moreover, we define the average stress tensor

$$\boldsymbol{\sigma}_{av} = \frac{1}{V} \int_{\Omega} \boldsymbol{\sigma} \, dV$$

yielding

$$\boldsymbol{\sigma}_{av} = -\frac{1}{V} \left[2\bar{\mathcal{T}} + \bar{\mathcal{W}}^{int} \right]^T .$$

Now, denoting $\boldsymbol{f}_{ij}$ the force acting on atom i because of atom j, we can write

$$\bar{\mathcal{W}}^{int} = \sum_i \boldsymbol{x}_i \otimes \boldsymbol{f}_i^{int}$$

$$= \sum_i \boldsymbol{x}_i \otimes \sum_j \boldsymbol{f}_{ij}$$

$$= \sum_{i,j} \boldsymbol{x}_i \otimes \boldsymbol{f}_{ij}. \tag{B.7}$$

Recalling that $\boldsymbol{f}_{ij} = -\boldsymbol{f}_{ji}$ we obtain the following identity

$$\sum_{i,j} \boldsymbol{x}_i \otimes \boldsymbol{f}_{ij} = \frac{1}{2} \left(\sum_{i,j} \boldsymbol{x}_i \otimes \boldsymbol{f}_{ij} + \sum_{i,j} \boldsymbol{x}_j \otimes \boldsymbol{f}_{ji} \right)$$

$$= \frac{1}{2} \sum_{i,j} (\boldsymbol{x}_i - \boldsymbol{x}_j) \otimes \boldsymbol{f}_{ij}$$

$$= \sum_{i<j} (\boldsymbol{x}_i - \boldsymbol{x}_j) \otimes \boldsymbol{f}_{ij} \tag{B.8}$$

Stress tensor is thus calculated from the difference between kinetic tensor $\mathcal{T} = \frac{1}{2} \sum_i m_i \boldsymbol{v}_i \otimes \boldsymbol{v}_i$ and the virial $\mathcal{W}^{int}$, using the formula

$$\boldsymbol{\sigma}_{av} = -\frac{1}{V} \left(\sum_i m_i \boldsymbol{v}_i \otimes \boldsymbol{v}_i + \sum_{i<j} \boldsymbol{f}_{ij} \otimes (\boldsymbol{x}_i - \boldsymbol{x}_j) \right)$$

where V is the volume of the computational box.

This is one easy way to compute the stress tensor from microscopical quantities of the system. The scalar pressure can be immediately derived from it, corresponding to trace($\boldsymbol{\sigma}_{av}$)/3. For this reason the stress tensor $\boldsymbol{\sigma}_{av}$ will be also indicated as the pressure tensor $\boldsymbol{P}$.

B.5 Pressure coupling

In most cases, NTP (constant particle number, constant temperature and constant pressure) simulations are more appropriate than NVT ones, being the limited volume of the box just an artifact. To simulate the correct pressure in NTP runs, a virtual barostat to control it is thus necessary.

The most commonly used method is Berendsen weak-coupling algorithm [114]. With this algorithm, the coordinates and the box vectors are rescaled at every step, which have the effect of a kinetic relaxation of the pressure towards a reference temperature P_0 [114]:

$$\frac{d\mathbf{P}}{dt} = -\frac{\mathbf{P} - \mathbf{P}_0}{\tau_p}.$$

The scaling of the vectors is made using a scaling matrix $\boldsymbol{\mu}$, defined as

$$\mu_{ij} = \delta_{ij} + \frac{\Delta t}{3\tau_p}\beta_{ij}\left(P_{ij} - P_{0\,ij}\right)$$

where $\boldsymbol{\beta}$ is the isothermal compressibility of the system, which is usually a diagonal matrix. Since it affects only the noncritical (for dynamic purposes) relaxation time constant τ_p, it is not strictly necessary to know it and a rough estimate for the system should suffice.

The rescaling can be made isotropically using a diagonal matrix with diagonal elements that equal trace($\boldsymbol{P}$)/3 instead of $\boldsymbol{P}$. Also, it can be sometimes useful to use semi-isotropic pressure scaling, where xy coordinates scale isotropically but independently from z. In case of anisotropic rescaling it can be necessary to re-impose box vectors orthogonality after the transformation.

B.6 Electrostatics

Computing non-bonded forces is the major issue regarding the speed of simulation and the scaling with the size of the system. Since the nature of non-bonded forces, every particle can in principle interact with *all* the other molecules, and a direct calculation for N atoms would take at least $N^2/2$ operations. The case of Van der Waals interactions is quite easy to solve introducing a cut-off, i.e. only interaction between atoms within a given distance are calculated. Due to the fast trend to zero of the Lennard-Jones potential, a reasonably well chosen cut-off distance lead to definitely negligible artifacts.

However, this is not the case for the $1/r$ Coulomb potential, for which long range effects could be important. Cut-offs can of course still be used, but they could lead to more severe artifacts and the choice of cut-off distance becomes a more delicate issue.

To optimize calculation of electrostatic potential in case of periodic boundary conditions Particle Mesh Ewald method can be used. It is based on Ewald summation [185], which

central idea is to divide the electrostatic potential into two components, the short-ranged and the long-ranged one:

$$U_{el} = U_{sr} + U_{lr}$$

The short ranged part sums up quickly in direct space, whereas the long ranged one sums up quickly in reciprocal space. Regarding the reciprocal part, PME algorithm interpolates charges distribution on a discrete grid, making possible the use of fast fourier transform (FFT) algorithms [115]. This method allows for short cut-off distance for the direct sum (between 8 and 12 Å) and sums in reciprocal spaces are truncated generally after few terms. The algorithm is indeed extremely fast and lead to very small errors.

Because of the periodicity assumed in Ewald summation periodic boundary conditions should be imposed. Moreover, the system needs to be neutral, or it could lead to infinite sums.

B.7 Water models

Simulating a single protein can offer insights about interactions between its atoms, but interactions with the surrounding environment would be neglected. Indeed, solvation effects are generally as important as internal interactions.

In vacuo simulations can be used to energetically minimize models to fix clashes or to do very short equilibration runs, however production runs should include a way to simulate solvation.

Water models can be either *explicit* or *implicit*.

Explicit models introduce effective water molecules in the system. Since water has important and very typical properties and behaviour, explicit modeling in terms of "classical" atoms is not a trivial problem and a wide range of models have been proposed. The choice of the correct one for the system depends on simulation requirements. For example simulating ice rather than liquid water will require two different models or modified parameters to correctly fit key properties. Explicit water models can be classified from the number of atoms, the inclusion of polarization effects and flexibility of the molecule. Most used models in MD are three point ones (expecially TIP3P [186]). It uses three atoms in a fixed geometry to which is given a charge to simulate water dipole moment. Only the oxygen atom interacts via Van der Waals potential. Other models can include additional "dummy" atoms (i.e. atom with no mass that interact only by coulomb potential) to better reproduce the electrostatic distribution around the molecule, or introducing additional potential terms to simulate polarization. However, this results in dramatically increased simulation workload, from which the preference for three point models.

Implicit water models compute the energetic effects of inserting the molecule in a continuous, high dielectric medium instead of introducing explicit water molecules. Computing solvation free energy would require in principle to solve the Poisson-Boltzmann(PB) equation [187], however its computational cost is very high. Approximated methods to solve PB equation like Generalized Born model have been developed, making implicit water a viable alternative to explicit methods. Implicit methods have the advantage of eliminating the need for the equilibration of water around the solute, and the absence of viscosity, which allows the protein to more quickly explore configuration space.

Appendix C

Sampling methods and analyses

C.1 Eyring rate theory

In this section of the Appendix, we will interpret the free energy profile in a way analogous to chemical reaction kinetic theory and we will approache with discrete models (saturating pore model), in which the ion binds in the various minima of free energy itself. Saturating pore models were first introduced in biology by Hodgkin and Keynes [157], and general theoretical methods were developed by Heckmann [158–161] and Läuger [162].

Let us consider the simplest saturable system, a channel with one binding site, X, that corresponds to a minimum of the free energy profile, and a permeating cation, S. If we replace all the subtleties of diffusion to and from the site by single rate constants, the steps of permeation become :

$$X + S_o \underset{k_{-1}}{\overset{k_1}{\rightleftharpoons}} XS \underset{k_{-2}}{\overset{k_2}{\rightleftharpoons}} XS_i$$

where the rate constants are, in general, dependent on the voltage. From chemical kinetics, the steady-state rate expression for current in the outward direction is:

$$I_S = zq_e \frac{k_{-1}k_{-2}[S]_i - k_1k_2[S]_o}{k_{-1} + k_2 + k_1[S]_o + k_{-2}[S]_i}.$$

When ions are present only on the outside, the current simplifies to

$$I_S = -zq_e \frac{k_2}{1 + (k_{-1} + k_2)/(k_1[S]_o)} \tag{C.1}$$

which is identical to the saturation function

$$I(E) = \frac{I_{max}(E)}{1 + k_s(E)/[S]_o}. \tag{C.2}$$

Since all the rate constants are functions of voltage and of ion species, I_{max} and k_S are also. Furthermore, if one repeats the derivation of equation C.2 assuming that ions are present only on the *inside*, one gets a similar equation but with different values for I_{max} and k_S.

When two kinds of ions, A and B, are present, we get not only saturation but also competition. Ions A and B compete for the binding site X, so that when one ion is present

at high concentration, the other is excluded. The net current with ions on both sides become

$$I_A + I_B = \frac{([A]_i/k_{Ai})I_{maxAi} + ([B]_i/k_{Bi})I_{maxBi} - ([A]_o/k_{Ao})I_{maxAo} - ([B]_o/k_{Bo})I_{maxBo}}{1 + [A]_i/k_{Ai} + [B]_i/k_{Bi} + [A]_o/k_{Ao} + [B]_o/k_{Bo}} \tag{C.3}$$

where the subscription on I_{max} and k shows whether the values for internal or external ions are meant. For more ions C, D, E, and so on, more identical terms can be added to the numerator and the denominator. In a more realistic pore, there may be a series of binding sites x_1, x_2,...,x_n along which the ion is relayed. Nevertheless, provided that only one ion is permitted in the pore at a time, equations C.1, C.2 and C.3 are again obtained, a result like the one for the kinetics of enzymes that bind only one substrate molecule at a time. No matter how many intermediate steps there are, the overall reaction still follows Michaelis-Menten kinetics.

Eyring rate theory is a way to summarize the values of rate constants in binding models of permeation. Energy wells can represent binding sites, and the occupancy of sites can be specifically included in the rate equation for jumps in and out of each site. The relation between the free energy of activation and the jump rate constant is defined by

$$k_f = k_0 exp(-\frac{\Delta G^{\ddagger}}{RT}) = k_0 exp(-\frac{\Delta H^{\ddagger}}{RT}) exp(\frac{\Delta S^{\ddagger}}{R}) \tag{C.4}$$

where the special symbols $S^{\ddagger}$, $H^{\ddagger}$ and $G^{\ddagger}$ stand for the standard entropy, enthalpy and Gibbs free energy of forming a mole of the activated complex from the reaction and the "prefactor" k_0 is the frequency with which a transition-state complex would break down to products. If b_{-1} represents the value of k_{-1} at zero membrane potential ($E = 0$), then from the definitions given from the one-site model in Figure C.1 we have:

$$b_{-1} = k_0 exp(-\frac{G_{12} - G_2}{RT}) \tag{C.5}$$

ad so forth. The quantity δ in the Figure C.1 represents the fraction of the total electrical potential drop, E, between the outside and the site. It is often called the *electrical distance* of the site from the outside. It should not be confused with the physical distance, which is far harder to determine. If the energy maxima lie at an electrical distance halfway between neighboring minima (assumption of a "symmetrical barrier"), then the voltage dependence of the rate constants can be written as

$$X + S_o \underset{b_{-1}exp(\delta V_S/2)}{\overset{b_1 exp(-\delta V_S/2)}{\rightleftharpoons}} XS \underset{b_{-2}exp((1-\delta)V_S/2)}{\overset{b_2 exp(-(1-\delta)V_S/2)}{\rightleftharpoons}} X + S_i \tag{C.6}$$

These equations fully specify the voltage and concentration dependence of the fluxes.

Now we are interested in a simple estimation for the conductance. As we said, conductance is a measure of conductivity, *i.e.* the ratio of the current flowing through a conductor and the difference in potential between the ends of the conductor. For a circuit, the conductance is the reciprocal of its resistance.

Since the hopping rate is proportional to the flux in the correspondent direction and the latter is proportional to conductance, from equation C.5 we can see the dependence of

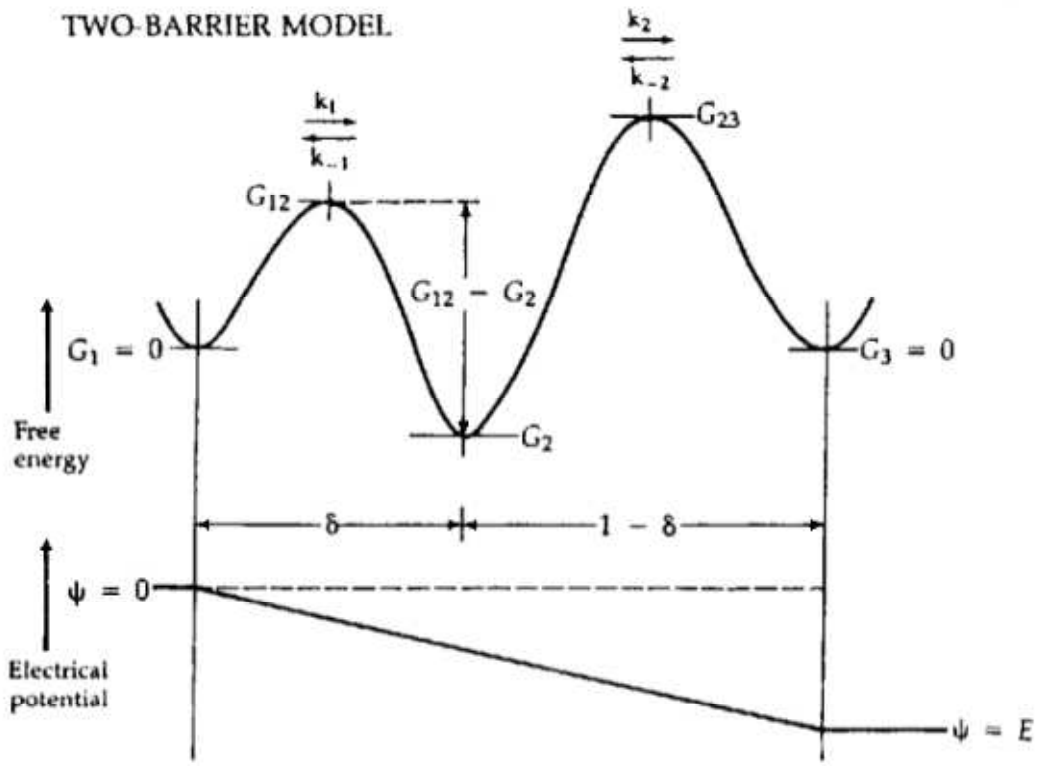

Figure C.1: Simple Barrier Model of Pores Definition of quantities needed for a two-barrier, one-site model. The fluxes are described by four hopping rate constants, k_i. They may be calculated from the free-energy barriers of the transitions, which have a "chemical" component, G, and an electrical component proportional to the voltage drop traversed and the ionic valence. The free energies G_{12}, G_2, and G_{23} are defined relatively to the bulk solution.

the conductance from the free energy profile at zero membrane potential. If we consider the hopping rates be independent, the total flux in one direction will be proportional to the product of the two rates and the conductance can be written as

$$\sigma = \alpha e^{-\frac{G_{12}-G_2}{RT}} e^{-\frac{G_{23}}{RT}} \tag{C.7}$$

where α is an appropriate constant.

In practice, the problem of calculating the constant α is rather complicated, and not fully understood yet, since it depends on the overall free energy profile, and not only on the free energy difference. However it is clear that the kinetic is completely dominated by the exponential part of equation C.7 and, if one assume that α depends weakly on the full free energy profile, this theory can be used to predict a ratio of conductance. In order to compute a singular value for conductance, we must adopt a different approach as we will see in the next section.

Another important approximation we are introducing is to restrict ourselves to the single ion model. Even if junctional channels can host several ions simultaneously, a treatment in terms of multiple ion transition is complicated by the fact that these channels are much larger than selective ionic channels, and thus binding sites can not in fact be defined. For these reasons, ions are rather mobile inside the channel, and the free energy

profile will be instead computed for a single ion, in the presence of the mean interaction with all the other ions in the channel.

C.2 Smoluchowski approach

A more precise value for conductance can be obtain by studying the diffusion of ions through the pore (described with free energy profile) using a Smoluchowski approach. We start from a model to describe particle in a fluid that take into account the inertial effect of Brownian particles. According to classical mechanics, the motion of a particle in a fluid would be described by Newton's second law

$$m\frac{d\vec{v}}{dt} = \vec{F}_T + \vec{F}_E(\vec{x})$$

where $\vec{v}$ is the velocity of the particles, $\vec{F}_E$ is the sum of external forces and $\vec{F}_T$ is the sum of the forces that each molecule of the fluid exerts on the particle. The latter can be described as a sum of a deterministic term $-m\gamma\vec{v}$ that describes viscosity friction, and a non-deterministic term $\vec{F}_R(t)$ that describes the collision effects with fluid.

Now we add the hypothesis of strong friction, *i.e.* $\dfrac{d\vec{v}}{dt} \ll -\gamma\vec{v}$ (where γ is the friction coefficient) obtaining

$$\frac{d\vec{x}}{dt} = \frac{1}{m\gamma}\left[\vec{F}_R(t) + \vec{F}_E(\vec{x})\right].$$

Since the Langevin force $\vec{F}_R(t)$ is a random variable it is necessary to define its statistics. Since the friction effect has already been taken into account and $\vec{F}_R(t)$ considers just the random effects of the collisions of the fluid molecules with the particle at rest *i.e.* in a isotropic and homogeneous space, the average of $\vec{F}_R$ over the realizations must be zero

$$\left\langle \vec{F}_R(t) \right\rangle = \frac{1}{N}\sum_{i=1}^{N} \vec{F}_i(t) = 0 \qquad \forall\, t \quad \text{and} \quad N \gg 1.$$

As a consequence, the effects of the collisions, described by $\vec{F}_R(t)$ are, on average, zero and the only systematic force acting on the particle would be friction one.

The correlation function of the force $\vec{F}_R(t)$ between the time t_1 and t_2 is defined operatively as

$$C_F(t_1, t_2) \equiv \left\langle \vec{F}_{t_1}\vec{F}_{t_2} \right\rangle = \frac{1}{N}\sum_{i=1}^{N} \vec{F}_{t_1}\vec{F}_{t_2}.$$

Since the fluid is supposed to be a *stationary state*, the average at two different times $\left\langle \vec{F}_{t_1}\vec{F}_{t_2} \right\rangle$ depends only on the difference $t_1 - t_2$ and one can write

$$C_F(\tau) = \left\langle \vec{F}_t\vec{F}_{t+\tau} \right\rangle \sim \exp(-\tau/\tau_c)$$

where τ_c is the correlation time of the Langevin force $\vec{F}_R$ related to the collisions with the surrounding fluid. In other words for $\Delta t \gg \tau_c$ collision events occurring around t can be

considered statistically independent from the ones occurring around $t + \Delta t$. So we can assume *two time-scales*, *i.e.* the collision time τ_c is much shorter than the evolution time of the velocity $\vec{v}$. This means that $\vec{F}_R(t_1)$ and $\vec{F}_R(t_2)$ are independent random variables for $|t_1 - t_2| \gg \tau_c$. Finally, we can say that the random force considered follows the statistics of a *white noise*.

For simplicity we restrict to one dimension and suppose that $\vec{F}_t$ is a *Gaussian process*. For a finite interval we can write

$$F_t = \sigma \Delta \hat{W}(t)$$

where $\sigma^2 \equiv \langle F_t^2 \rangle$ is a increment of a Wiener process, *i.e.* a real stochastic process, null for $t = 0$, with null mean and independent, stationary and Gaussian increments.

Finally, regarding finite increments, we can write Langevin equation as

$$\Delta x(t) = \frac{F(x(t))}{\gamma m} \Delta t + \frac{\sigma}{\gamma m} \Delta \hat{W}(t). \tag{C.8}$$

Let us consider a stochastic process $\{X(t)\}_{t \geq 0}$ with realization $x(t)$. Since $X(t)$ is a random variable, it is reasonable to look at its probability density distribution $p(x, t|x_0)dx = \mathbb{P}\{x \leq X(t) \leq x + dx | X(0) = x_0\}$ defined on $\Omega = [r, \xi]$.

We have to define the boundary conditions. We used r as reflection point (*i.e.* $\dfrac{\partial p}{\partial t}(x = r, t|x_0) = 0$) and ξ as an absorption point (*i.e.* $p(x = \xi, t) = 0$).

For the diffusion application, we limit our discussion to $p(x, t|x_0)$ that satisfies the *Fokker-Planck equation*

$$\frac{\partial}{\partial t} p(x, t|x_0) = \hat{L}_{FP}(x, t) p(x, t|x_0) \tag{C.9}$$

where $\hat{L}_{FP}(x, t)$is the *Fokker-Planck differential operator*

$$\hat{L}_{FP}(x, t) = -\frac{\partial}{\partial x} D^{(1)}(x, t) + \frac{\partial^2}{\partial x^2} D^{(2)}(x, t)$$

with

$$D^{(1)}(x, t) = \lim_{\Delta t \to 0} \frac{1}{\Delta t} \int_{\mathbb{R}} dx'(x' - x) p(x', t + \Delta t | x, t) \qquad \textbf{drift term}$$

$$D^{(2)}(x, t) = \frac{1}{2} \lim_{\Delta t \to 0} \frac{1}{\Delta t} \int_{\mathbb{R}} dx'(x' - x)^2 p(x', t + \Delta t | x, t) \qquad \textbf{diffusion term}.$$

A distribution which is a solution of the forward Fokker-Planck equation, is also a solution of the backward Fokker-Plank equation

$$\frac{\partial}{\partial t} p(x, t|x_0) = \hat{L}_{FP}^{\dagger}(x_0) p(x, t|x_0)$$

where $\hat{L}_{FP}^{\dagger}(x_0)$ is the adjoint of the Fokker-Planck operator.

Using equation C.8, we can compute drift and diffusion terms and obtain the so called *Smoluchowski equation*

$$\frac{\partial p(x, t|x_0)}{\partial t} = -\frac{\partial}{\partial x} \left[\frac{F(x)}{\gamma m} p(x, t|x_0) \right] + \frac{\sigma^2}{2\gamma^2 m^2} \frac{\partial^2}{\partial x^2} p(x, t|x_0). \tag{C.10}$$

The external force $F(x)$, in the diffusion space, is given by a potential $U(x)$, *i.e.* $F(x) = -\dfrac{dU(x)}{dx} \equiv -\dot{U}(x)$. Moreover, by identifying stationary state with thermal equilibrium, we can find a relation between the microscopic quantities σ and γ with the macroscopic quantities D and T where D is the diffusion coefficient and T is the temperature of the thermal bath of our system. We can then rewrite Smoluchowski equation as

$$\begin{aligned}\frac{\partial p(x,t|x_0)}{\partial t} &= D\frac{\partial}{\partial x}\left\{\exp\left[-\frac{U(x)}{k_BT}\right]\frac{\partial}{\partial x}\exp\left[\frac{U(x)}{k_BT}\right]\right\}p(x,t|x_0)\\ &= \hat{L}_{FP}(x,t)p(x,t|x_0)\end{aligned} \tag{C.11}$$

If the process starts at $x_0 = X(0)$, we define the *first passage time* T of the process as the first time it will reach the boundary. It is possible to compute the Mean First Passage Time (MFPT) $T^{(1)}$, *i.e.* the first moment of the first passage time, that is

$$\hat{L}^{\dagger}_{FP}(x_0)T^{(1)}(x_0) = -1$$

where, in our case,

$$\hat{L}^{\dagger}_{FP}(x_0) = D\exp\left[\frac{U(x)}{k_BT}\right]\frac{\partial}{\partial x_0}\left\{\exp\left[-\frac{U(x)}{k_BT}\right]\frac{\partial}{\partial x_0}\right\}$$

therefore we obtain

$$\tau := T^{(1)}(x_0) = \frac{1}{D}\int_{x_0}^{\xi} e^{\beta U(y)}dy\int_{r}^{y} e^{-\beta U(z)}dz. \tag{C.12}$$

where we have identified the MFPT with the time τ that one ion spends to pass through the channel.

Assuming that a single ion can occupy the channel, we can relate the flux J with the time τ as

$$J = \frac{1}{\tau},$$

so we can write the current I due to the passage of ions trough the channel as

$$I = \frac{q}{\tau}$$

where q is the electric charge of a single ion.

If we have a single type of ion that creates the current(*e.g* K^+ like in many experimental conditions), the net current through the channel is due to the flux on the ions in one direction ($J_+ = \frac{1}{\tau_+}$) minus the flux in the opposite one ($J_- = \frac{1}{\tau_-}$). So we have

$$I = q(J_+ - J_-) = G\Delta V \tag{C.13}$$

where G is the conductance of the channel.

To compute the conductance we need a no zero current. Therefore we calculate the MFPT of one ion through the pore using the free energy profile plus a potential differences dependent on the position z, *i.e.* maximum in the first cell and then decreasing linearly until zero value in the second one.

Using this Smoluchowski approach we are able to compute the value of the conductance for the single channel bypassing the problem of the α constant of the Eyring theory. Moreover we obtain a better approximation of the ratio value. As we have seen, we need to compute the mean first passage time of the ion using the free energy profile found with MD for the whole connexon channel.

Using the mean first passage time we can compute the flux of one type of ions in one direction. Experimentally, measures of GJs conductance are done with a solution in which only one type of ions (*e.g.* K^+) moves through the pore. Whereby, in order to obtain a result comparable with experiments, we regard the passage trough the GJ channel of only K^+ ions. Then we can use equation C.13 to compute the current due to the net flux of K^+ ions through the pore. To have a value of I different from zero we must add a difference of potential ΔV between the two cells, given as a quantity with maximum value in the first cell and then decreasing linearly until zero value in the second one. The energy that needs to be added to the PMF in the point z is given by

$$U_{el}(z) = q\frac{\Delta V}{L}(L - z) \tag{C.14}$$

where L is the length of the channel.

In the next Subsection we will apply the SMD method and the two interpretation theory we have seen until here to our hCx26 hemichannel WT and M34T mutant model.

C.3 Umbrella Sampling technique

The calculation of free-energy differences is a central task in computational science. The free energy difference is the driving force of any process, such as a chemical reaction. Transition state theory [188–190] can be used to calculate reaction rates from energy barriers, more exactly free-energy barriers [191]. The free energy contains the entropy, a measure for the available space. To map the available space in a system bigger than a few atoms, extensive sampling is required [192]. Techniques are regularly being reviewed in the literature, with a few recent ones given in J Comput Chem and in a themed issue of J Comput Chem in 2009 [193]. Applications range from the solid state, catalytic reactions, biochemical processes to rational drug design. The canonical partition function Q of a system can be calculated via an integral over the whole phase space, *i.e.*, configuration space and momentum space. If the potential energy E is independent of the momentum, the integral over the latter is a multiplicative constant to Q, which can be ignored. Then, Q is obtained as

$$Q = \int exp[-\beta E(r)]d^N r \tag{C.15}$$

with $\beta = 1/(k_B T)$, k_B being the Boltzmann's constant, T being the absolute temperature, and N being the number of degrees of freedom of the system. The free (Helmholtz) energy A is related to Q via $A = -1/\beta\ lnQ$. The canonical partition function involves a constant number of particles, constant volume, and a constant temperature. If the pressure, rather than the volume, is kept constant, the Gibbs free energy (usually denoted as G) is obtained. Apart from the change in the ensemble, the following formalisms and derivations are equivalent for A and G. In the condensed phase, which is relevant for most applications, the systems are hardly compressible; so A and G are numerically very similar. In chemical

reactions, one is generally interested in free-energy differences between two states. If the two states differ by geometry (like a reactant and product of a reaction) then the integration in Eq. C.15 is done over a part of the coordinate space for each state. In many cases, a reaction coordinate (ξ), a continuous parameter which provides a distinction between two thermodynamic states, can be defined. Any order-parameter is possible, even a change in the energy expression (the Hamiltonian). The reaction coordinate can be one or more dimensional. Often, ξ is defined on geometric grounds, such as distance, torsion, or the difference between root mean square deviations from two reference states. With ξ defined, the probability distribution of the system along ξ can be calculated by integrating out all degrees of freedom but ξ :

$$Q(\xi) = \frac{\int \delta[\xi(r) - \xi] exp[(-\beta E) d^N r]}{\int exp[(-\beta E) d^N r]} \tag{C.16}$$

$Q(\xi)\ d\xi$ can be interpreted as the probability of finding the system in a small interval $d\xi$ around ξ . Consequently, this allows the calculation of the free energy along the reaction coordinate; $A(\xi) = -1/\beta\ lnQ(\xi)$. $A(\xi)$ is also called potential of mean force (PMF). If ξ is a general, *i.e.*, non-Cartesian, coordinate, or a set of those, a Jacobian term enters Eq. C.16. As long as the integration is performed in Cartesian coordinates, $Q(\xi) = \int \delta[\xi(r) - \xi] exp(-\beta E) d^N r/Q$. In computer simulations, the direct phase-space integrals used in Eqs. C.15 and C.16 are impossible to calculate. However, if the system is ergodic, *i.e.*, if every point in phase space is visited during the simulation, $Q(\xi)$ is equal to

$$P(\xi) = lim_{t\to\infty} \frac{1}{t} \int_0^t \rho[\xi(t')] dt' \tag{C.17}$$

that is, the ensemble average $Q(\xi)$ becomes equal to the time average $P(\xi)$ for infinite sampling in an ergodic system. In Eq. C.17, t denotes the time and ρ simply counts the occurrence of ξ in a given interval (of infinitesimal width in the exact equation and of finite width when calculating a histogram). So, in principle, $A(\xi)$ can be directly obtained from molecular dynamics (MD) simulations by monitoring $P(\xi)$, the distribution of the system along the reaction coordinate. Note that the terms distribution, distribution function, frequency, probability density, and possibly a few more are sometimes used in the literature of chemistry and physics in different contexts. Through out this article, the term distribution $P(\xi)$ refers to the normalized frequency of finding the system in the vicinity of a given value of ξ . If $P(\xi)$ was obtained from an exact ensemble average rather than a sampled quantity, $P(\xi)$ would refer to a probability density. However, simulations are only run for finite time. Regions in configuration space around a minimum in $E(r)$ are typically sampled well, whereas regions of higher energy are sampled rarely. For rare events, those with an energy barrier significantly larger than $k_B T$, direct sampling is infeasible. To obtain a profile $A(\xi)$, however, also those high-energy regions, those rare events, are required. Different techniques have been developed to sample such rare events. One can broadly distinguish three different families of methods: (1) methods that sample the system in equilibrium, (2) nonequilibrium sampling techniques, and (3) methods that introduce additional degrees of freedom, along which the free energy is calculated. The third family includes λ-dynamics and metadynamics [193].

On the one hand, the path is split into windows. Each window covers only a small part of the range of ξ . The windows are sampled individually. In postprocessing, the results of

the different windows are combined to result in a global free-energy profile $A(\xi)$. On the other hand, one can run multiple simulations. In each of those, the system is driven from one state of interest (A) to the other state (B), taking a different path each time. The postprocessing in this case includes averaging over the different simulations. To drive a system over an energy barrier, one can either (1) modify the energy expression in order to reduce the barrier, or (2) restrict the sampling space to all degrees of freedom, but the reaction coordinate describing the transition over the barrier. The former is known as biased MD or umbrella sampling [193]. Because this is the main focus of the present review, it will be discussed in detail in Umbrella Sampling: Method. In umbrella sampling, the reaction coordinate is not constrained, but only restrained and pulled to a target value by a bias potential. Therefore, the full momentum space is sampled. Usually, umbrella sampling is done in a series of windows, which are finally combined either with the weighted histogram analysis method (WHAM) [194].

Umbrella sampling was developed by Torrie and Valleau based on related previous work [193]. A bias, an additional energy term, is applied to the system to ensure efficient sampling along the whole reaction coordinate. This can either be aimed at in one simulation or in different simulations (*windows*), the distributions of which overlap. The effect of the bias potential to connect energetically separated regions in phase space gave rise to the name umbrella sampling. In this section, the formalism of recovering unbiased free-energy differences from biased simulations will be discussed. The next section describes different forms of bias potentials used in the literature. The bias potential w_i of window i is an additional energy term, which depends only on the reaction coordinate:

$$E^b(r) = E^u(r) + w_i(\xi) \tag{C.18}$$

The superscript "b" denotes biased quantities, whereas the superscript "u" denotes unbiased quantities. Quantities without superscripts are always unbiased. In order to obtain the unbiased free energy $A_i(\xi)$, we need the unbiased distribution, which is, according to Eq. C.16:

$$P_i^u(\xi) = \frac{\int exp[-\beta E(r)]\delta[\xi'(r) - \xi]d^N r}{exp[-\beta E(r)]d^N r} \tag{C.19}$$

MD simulation of the biased system provides the biased distribution along the reaction coordinate P_i^b. Assuming an ergodic system,

$$P_i^b(\xi) = \frac{\int exp{-}\beta[E(r) + \omega_i(\xi'(r))]\delta[\xi'(r) - \xi]d^N r}{\int exp{-}\beta[E(r) + \omega_i(\xi'(r))]d^N r}$$

Because the bias depends only on ξ and the integration in the enumerator is performed over all degrees of freedom but ξ ,

$$P_i^b(\xi) = exp[-\beta\omega_i(\xi)]\frac{\int exp[-\beta E(r)]\delta[\xi'(r) - \xi]d^N r}{\int exp{-}\beta[E(r) + \omega_i(\xi'(r))]d^N r}$$

Using Eq. C.19 results in

$$\begin{aligned} P_i^u(\xi) &= P_i^b(\xi)exp[\beta\omega_i(\xi)]\frac{\int exp{-}\beta[E(r) + \omega_i(\xi(r))]d^N r}{\int exp[-\beta E(r)]d^N r} \\ &= P_i^b(\xi)exp[\beta\omega_i(\xi)]\frac{\int exp[-\beta E(r)]exp{-}\beta\omega_i[\xi(\overrightarrow{r})]d^N r}{\int exp[-\beta E(r)]d^N r} \\ &= P_i^b(\xi)exp[\beta\omega_i(\xi)]\langle exp[-\beta\omega_i(\xi)]\rangle. \end{aligned} \tag{C.20}$$

From Eq. C.20, $A_i(\xi)$ can be readily evaluated. $P_i^b(\xi)$ is obtained from an MD simulation of the biased system, $w_i(\xi)$ is given analytically, and $0F_i = -(1/\beta)\ ln\langle exp[-\beta\omega_i(\xi)]\rangle$ is independent of ξ:

$$A_i(\xi) = -(1/\beta)lnP_i^b(\xi) - w_i(\xi) + F_i \tag{C.21}$$

This derivation is exact. No approximation enters apart from the assumption that the sampling in each window is sufficient. This is facilitated by an appropriate choice of umbrella potentials $w_i(\xi)$. As long as one window spans the whole range of ξ to be studied, Eq. C.21 is sufficient to unbias the simulation. $A(\xi)$ is in any case only defined up to an additive constant; so in this case, F_i can be chosen arbitrarily. If the free-energy curves $A_i(\xi)$ of more windows are to be combined to one global $A(\xi)$ the F_i have to be calculated. They are associated with introducing the bias potential and connect the free-energy curves $A_i(\xi)$ obtained in the different windows:

$$\begin{aligned} exp(-\beta F_i) &= \langle exp[-\beta\omega_i(\xi)]\rangle \\ &= \int P^u(\xi)exp[-\beta\omega_i(\xi)]d\xi \\ &= \int exp{-}\beta[A(\xi) + \omega_i(\xi)]d\xi \end{aligned} \tag{C.22}$$

with $P^u(\xi)$ being the global unbiased distribution. The F_i cannot directly be obtained from sampling. Methods to Analyze Umbrella Sampling Simulations will deal with methods to calculate them, *i.e.*, to combine the results of different windows in umbrella sampling. Ideally, the bias potential is chosen such that sampling along the whole range of the reaction coordinate ξ is uniform. Therefore, the optimal bias potential is $w_{opt} = -A(\xi)$. This would lead to a truly uniform distribution $P_i^b(\xi)$. However, $A(\xi)$ is obviously not known; it is what we aim to calculate with umbrella sampling. Therefore, two main families of bias potentials have emerged: harmonic biases in a series of windows along ξ , and an adaptive bias, which is adjusted to match $-A(\xi)$ in only one window spanning the whole range of ξ .

C.3.1 Harmonic Bias Potentials

To ensure sampling in all regions of ξ, the range of interest of ξ is split into a number of windows. In each window, a bias function is applied to keep the system close to the reference point ξ_i^{ref} of the respective window i. Often, a simple harmonic bias of strength K is used:

$$\omega_i(\xi) = K/2(\xi - \xi_i^{ref})^2 \tag{C.23}$$

After the simulations, the free-energy curves are combined with techniques discussed in Methods to Analyze Umbrella Sampling Simulations (typically *WHAM* or umbrella integration). The form of the bias given in Eq. C.23 is appealing because it contains only few parameters: K (which in principle can be window dependent), the number of images, and ξ_i^{ref}. The latter are usually chosen uniformly distributed along ξ. The higher the number of images, the smaller is generally the statistical error relative to CPU time [193]. However, the CPU time needed for equilibration, on the contrary, increases with the number of images. The MD simulations of the images are completely independent and thus, can run in parallel. The choice of K, the strength of the bias, is the only critical decision. It has to be made before simulations are run. By contrast, additional windows

could always be inserted if the first series of windows results in too large gaps between the distributions. Overall, K has to be large enough to drive the system over the barrier. Too large K, however, will cause very narrow distributions $P_i^b(\xi)$. Sufficient overlap between the distributions is required for WHAM, whereas it is not required, but still advantageous in umbrella integration [193]. Increasing K at constant time step also leads to increasing errors in the numerical integration of the equations of motions. If the time step is too large (or K is too large), configurations with high energies will be overrepresented. For umbrella integration analysis, analytic expressions for the statistical error can be derived, which allow an estimate of an ideal K based on quantities, which can often be estimated prior to sampling. It has also been suggested that the location of the next window to be sampled (ξ_{i+1}^{ref}) can be chosen from the location and the widths of the previous window to match their estimated half maxima [193]. An alternative is to use data from the experiment to define the most promising bias parameters [193].

C.3.2 Umbrella Sampling analyse: Weighted Histogram Analysis Method (WHAM)

Numerous methods have been proposed for an estimation of F_i, [193] a promising one being the WHAM [194]. It aims to minimize the statistical error of $P^u(\xi)$. The global distribution is calculated by a weighted average of the distributions of the individual windows:

$$P^u(\xi) = \sum_i^{windows} p_i(\xi) P_i^u(\xi) \tag{C.24}$$

The weights p_i are chosen in order to minimize the statistical error of P^u :

$$\frac{\partial \sigma^2(P^u)}{\partial p_i} = 0$$

under the condition $\sum p_i = 1$. This leads to [194]:

$$p_i = \frac{a_i}{\sum_j a_j}\ , \qquad a_i(\xi) = N_i exp[-\beta\omega_i(\xi) + \beta F_i] \tag{C.25}$$

with N_i being the total number of steps sampled for window i. The F_i are calculated by Eq. C.22:

$$exp(-\beta F_i) = \int P^u(\xi) exp[-\beta w_i(\xi)] d\xi. \tag{C.26}$$

Because P^u enters Eq. C.26 and F_i enters Eq. C.24 via Eq. C.25, these have to be iterated until convergence. For many bins, this convergence can be slow.

In general, it is preferable to sample many windows for shorter times than fewer windows for longer [193]. This leads to a smaller statistical error because of the better overlap between the windows and is better parallelizable.

Bibliography

[1] Nalin M. Kumar and Norton B. Gilula. The gap junction communication channel. *Cell*, 84:381–388, 1996.

[2] Furshpan E. J. and Potter D. D. Low-resistance junctions between cells in embryos and tissue culture. *Current Topics in Development of Biology*, 3:95–127, 1968.

[3] Watanabe A. The interaction of electrical activity among neurons of lobster cardiac ganglion. *Japanese Journal of Physiology*, 8:305–318, 1958.

[4] Michael V.L. Bennett. Gap junctions as electrical synapses. *Journal of Neurocytology*, 26:349–366, 1997.

[5] Robertson J. D. The occurrence of a subunit pattern in the unit membrane of club endings in mauthner cell synapses in gold fish brains. *Journal of Cell Biology*, 19:201–221, 1963.

[6] Paul D.L. Molecular cloningof cdna for rat liver gap junction protein. *Journal of Cell Biology*, 103:123–134, 1986.

[7] Oviedo-Orta E., Hoy T., and Evans W. H. Intercellular communication in the immune system: differential expression of connexin40 and 43, and perturbation of gap junction channel functions in peripheral blood and tonsil human lymphocyte subpopulations. *Immunology*, 99:578–590, 2000.

[8] Cancelas J. A., Koevoet W. L., de Koning A. E., Mayen A. E., Rombouts E. J., and Ploemacher R. E. Connexin-43 gap junctions are involved in multi-connexin-expressing stromal support of hemopoietic progenitors and stem cells. *Blood*, 96:498–505, 2000.

[9] Rosendaal M. and Krenacs T. T. Regulatory pathways in blood-forming tissue with particular reference to gap junctional communication. *Pathology and Oncology Research*, 6:243–249, 2000.

[10] Montecino-Rodriguez E. and Dorshkind K. Regulation of hematopoiesisby gap junction-mediatedintercellularcommunication. *Journal of Leukocyte Biology*, 70:341–347, 2001.

[11] W. Howard Evans and Patricia E. M. Martin. Gap junctions: structure and function (review). *Molecular Membrane Biology*, 19:121–136, 2002.

[12] Verselis V.K. and Veenstra R.D. Gap junction channels: Permeability and voltage gating. In Hertzberg E.L., editor, *Gap Junctions*, pages 129–192. Jai Press, Stamford, 2000.

[13] Massimiliano Bicego, Martina Beltramello, Salvatore Melchionda, Massimo Carella, Valeria Piazza, Leopoldo Zelante, Feliksas F. Bukauskas, Edoardo Arslan, Elona Cama, Sergio Pantano, Roberto Bruzzone, Paola D'Andrea, and Fabio Mammano. Pathogenetic role of the deafness-related m34t mutation of cx26. *Human Molecular Genetics*, 15:2569–2587, 2006.

[14] Martina Beltramello, Valeria Piazza, Feliksas F. Bukauskas, Tullio Pozzan, and Fabio Mammano. Impaired permeability to $ins(1,4,5)p_3$ in a mutant connexin underlies recessive hereditary deafness. *Nature Cell Biology*, 7:63–69, 2005.

[15] Hernandez V.H., Bortolozzi M., Pertegato V., Beltramello M., Giarin M., Zaccolo M., Pantano S., and Mammano F. Unitary permeability of gap junction channels to second messengers measured by fret microscopy. *Nature Methods*, 4:353–358, 2007.

[16] Andrew L Harris. Connexin channel permeability to cytoplasmic molecules. *Progress in biophysics and molecular biology*, 94(1):120–143, 2007.

[17] Shoji Maeda, So Nakagawa, Michihiro Suga, Eiki Yamashita, Atsunori Oshima, Yoshinori Fujiyoshi, and Tomitake Tsukihara. Structer of the connexin 26 gap junction channel at 3.5 Å resolution. *Nature*, 458:597–602, 2009.

[18] Kwon T., Harris A.L., Rossi A., and Bargiello T.A. Molecular dynamics simulations of the cx26 hemichannel: evaluation of structural models with brownian dynamics. *J Gen Physiol*, 138:475–493, 2011.

[19] Francesco Zonta, Guido Polles, Giuseppe Zanotti, and Fabio Mammano. Permeation pathway of homomeric connexin 26 and connexin 30 channels investigated by molecular dynamics. *Biomolecular Structure & Dynamics*, 29:985–998, 2012.

[20] Francesco Zonta and other. The 3.5 angström x-ray structure of the human connexin26 gap junction channel is unlikely that of a fully open channel. *Cell Comunication and signaling*, 11:15:–, 2013.

[21] Francesco Zonta, Damiano Buratto, Chiara Cassini, Mario Bortolozzi, and Fabio Mammano. Molecular dynamics simulations highlight structural and functional alterations in deafness-related m34t mutation of connexin 26. *Frontiers in Physiology*, 5:85:–, 2014.

[22] Francesco Zonta, Giorgia Girotto, Damiano Buratto, Giulia Crispino, Anna Morgan, Khalid Abdulhadi, Moza Alkowari, Ramin Badii, Paolo Gasparini, and Fabio Mammano. The p.cys169tyr variant of connexin 26 is not a polymorphism. *Human Molecular Genetics*, 24:2641–2648, 2015.

[23] Daniel A. Goodenough and David L. Paul. Gap junctions. *Cold Spring Harbor Perspectives in Biology*, 1(1), 2009.

[24] Daniel J. Müller, Dimitrios Fotiadis, and Andreas Engel. Mapping flexible protein domains at subnanometer resolution with the atomic force microscope. *FEBS Letters*, 430:105–111, 1998.

[25] Daniel J. Müller, Galen M. Hand, Andreas Engel, and Gina E. Sosinsky. Conformational changes in surface structures of isolated connexin 26 gap junctions. *The EMBO Journal*, 21:3598–3607, 2002.

[26] Binnig G., Quate C.F., and Gerber C. Atomic force microscope. *Phys. Rev. Lett.*, 56:930–933, 1986.

[27] Hoh J.H., Lal R., John S.A., Revel J.-P., and Arnsdorf M.F. Atomic force microscopy and dissection of gap junctions. *Science*, 253:1405–1408, 1991.

[28] Hoh J.H., Sosinsky G.E., Revel J.-P., and Hansma P.K. Structure of the extracellular surface of the gap junction by atomic force microscopy. *Biophys. J.*, 65:149–163, 1993.

[29] Brad C. Bennett, Michael D. Purdy, Kent A. Baker, Chayan Acharya, William E. McIntire, Raymond C. Stevens, Qinghai Zhang, Andrew L. Harris, Ruben Abagyan, and Mark Yeager. An electrostatic mechanism for ca(2+)-mediated regulation of gap junction channels. *Nature communications*, 7:8770, 2016.

[30] Willecke K., Eiberger J., Degen J., Eckardt D., Romualdi A., Guldenagel M., Deutsch U., and Soehl G. Structural and functional diversity of connexin genes in the mouse and human genome. *Biological Chemistry*, 383:725–737, 2002.

[31] Beyer E.C., Paul D.L., and Goodenough D.A. Connexin family of gap junction proteins. *J Membr Biol.*, 116(3):187–194, 1990.

[32] Unger V.M., Kumar N.M., Gilula N.B., and Yeager M. Three-dimensional structure of a recombinant gap junction membrane channel. *Science*, 283:1176–1180, 1999.

[33] Fleishman .J., Unger SV.M., Yeager M., and Ben-Tal N. A calpha model for the transmembrane alpha helices of gap junction intercellular channels. *Mol Cell*, 15:879–888, 2004.

[34] Kovacs J.A., Baker K.A., Altenberg G.A., Abagyan R., and Yeager M. Molecular modeling and mutagenesis of gap junction channels. *Prog Biophys Mol Biol*, 94:15–28, 2007.

[35] Pantano S., Zonta F., and Mammano F. A fully atomistic model of the cx32 connexon. *PLoS One*, 3:e2614, 2008.

[36] W. Howard Evans, Elke De Vuyst, and Luc Leybaert. The gap junction cellular internet: connexin hemichannels enter the signalling limelight. *Biochemical Journal*, 397:1–14, 2006.

[37] Mauricio A. Retamal and Juan C. Saez. Hemichannels; from the molecule to the function. *frontiers in physiology*, 5:1, 2014.

[38] Richard F., Hyunsoo X., Xin P., Chin-Jen W., Stephen C., Bishwanath C., and Cecilia L. Connexin43 modulates cell polarity and directional cell migration by regulating microtubule dynamics. *PLoS ONE*, 6(10):e26379, 2011.

[39] Levin M. and Mercola M. Gap junctions are involved in the early generation of left-right asymmetry. *Dev. Biol.*, 203(1):90–105, 1998.

[40] Levin M. and Mercola M. Gap junction-mediated transfer of left-right patterning signals in the early chick blastoderm is upstream of shh asymmetry in the node. *Development.*, 126(21):4703–14, 1999.

[41] Bani-Yaghoub M., Bechberger J.F., Underhill T.M., and Naus C.C. The effects of gap junction blockage on neuronal differentiation of human ntera2/clone d1 cells. *Exp Neurol.*, 156(1):16–32, 1999.

[42] Donahue H.J., Li Z., Zhou Z., and Yellowley C.E. Differentiation of human fetal osteoblastic cells and gap junctional intercellular communication. *Cell Physiol.*, 278(2):C315–22, 2000.

[43] Cronier L., Frendo J.L., Defamie N., Pidoux G., Bertin G., Guibourdenche J., Pointis G., and Malassine A. Requirement of gap junctional intercellular communication for human villous trophoblast differentiation. *Biol. Reprod.*, 69(5):1472–80, 2003.

[44] El-Sabban M.E., Sfeir A.J., Daher M.H., Kalaany N.Y., Bassam R.A., and Talhouk R.S. Ecm-induced gap junctional communication enhances mammary epithelial cell differentiation. *J. Cell. Sci.*, 116:3531–41, 2003.

[45] Andrew L.Harris. Emerging issues of connexin channels: biophysics fills the gap. *Quarterly Reviews of Biophysics*, 34(3):325–472, 2001.

[46] Hong-Bo Zhao. Connexin26 is responsible for anionic molecule permeability in the cochlea for intercellular signalling and metabolic communications. *EJN*, 21(7):1859–1868, 2005.

[47] DeVries S.H. and Schwartz E.A. E.A. Hemi-gap-junction channels in solitary horizontal cells of the catfish retina. *The Journal of Physiology*, 445(1):201, 1992.

[48] Federico Ceriani, Tullio Pozzan, and Fabio Mammano. Critical role of atp-induced atp release for ca2+ signaling in nonsensory cell networks of the developing cochlea. *Proceedings of the National Academy of Sciences*, page 201616061, 2016.

[49] HVM Van Rijen, Ronald Wilders, Antoni CG Van Ginneken, and Habo J Jongsma. Quantitative analysis of dual whole-cell voltage-clamp determination of gap junctional conductance. *Pflügers Archiv*, 436(1):141–151, 1998.

[50] Moreno A.P. Biophysical properties of homomeric and heteromultimeric channels formed by cardiac connexins. *Cardiovasc Res.*, 62(2):267–286, 2004.

[51] Jacques Neyton and Alain Trautmann. Single-channel currents of an intercellular junction. *Nature*, 317(6035):331, 1985.

[52] Richard D Veenstra and Robert L DeHaan. Measurement of single channel currents from cardiac gap junctions. *Science*, 233(4767):972–974, 1986.

[53] R Weingart. Electrical properties of the nexal membrane studied in rat ventricular cell pairs. *The Journal of physiology*, 370(1):267–284, 1986.

[54] Ida Chow and Steven H Young. Opening of single gap junction channels during formation of electrical coupling between embryonic muscle cells. *Developmental biology*, 122(2):332–337, 1987.

[55] MB Rook, HJ Jongsma, and AC Van Ginneken. Properties of single gap junctional channels between isolated neonatal rat heart cells. *American Journal of Physiology-Heart and Circulatory Physiology*, 255(4):H770–H782, 1988.

[56] RD Veenstra, HZ Wang, EM Westphale, and EC Beyer. Multiple connexins confer distinct regulatory and conductance properties of gap junctions in developing heart. *Circulation Research*, 71(5):1277–1283, 1992.

[57] Yozo Nishimura, Ricardo L Smith, and Kazuyo Shimai. Junction-like structure appearing at apposing membranes in the double cone of chick retina. *Cell and tissue research*, 218(1):113–116, 1981.

[58] Feliksas F Bukauskas, Rolf Vogel, and Robert Weingart. Biophysical properties of heterotypic gap junctions newly formed between two types of insect cells. *The Journal of physiology*, 499(Pt 3):701, 1997.

[59] Valiunas V., Manthey D., Vogel R., Willecke K., and Weingart R. Biophysical properties of mouse connexin30 gap junction channels studied in transfected human hela cells. *J. Physiol.*, 519:631–644, 1999.

[60] DL Paul, L Ebihara, LJ Takemoto, KI Swenson, and DA Goodenough. Connexin46, a novel lens gap junction protein, induces voltage-gated currents in nonjunctional plasma membrane of xenopus oocytes. *The Journal of cell biology*, 115(4):1077–1089, 1991.

[61] SH DeVries and EA Schwartz. Hemi-gap-junction channels in solitary horizontal cells of the catfish retina. *The Journal of Physiology*, 445:201, 1992.

[62] LISA Ebihara and ERIK Steiner. Properties of a nonjunctional current expressed from a rat connexin46 cdna in xenopus oocytes. *The Journal of general physiology*, 102(1):59–74, 1993.

[63] Guido A Zampighi, Donald DF Loo, Michael Kreman, Sepehr Eskandari, and Ernest M Wright. Functional and morphological correlates of connexin50 expressed in xenopus laevis oocytes. *The Journal of general physiology*, 113(4):507–524, 1999.

[64] Jay D Pal, Xiaoqin Liu, Donna Mackay, Alan Shiels, Viviana M Berthoud, Eric C Beyer, and Lisa Ebihara. Connexin46 mutations linked to congenital cataract show loss of gap junction channel function. *American Journal of Physiology-Cell Physiology*, 279(3):C596–C602, 2000.

[65] Sanchez H.A., Villone K., Srinivas M., and Verselis V.K. The d50n mutation and syndromic deafness: altered cx26 hemichannel properties caused by effects on the pore and intersubunit interactions. *J Gen Physiol.*, 142(1):3–22, 2013.

[66] Werner R Loewenstein and Yoshinobu Kanno. Studies on an epithelial (gland) cell junction i. modifications of surface membrane permeability. *The Journal of cell biology*, 22(3):565–586, 1964.

[67] George D Pappas and Michael VL Bennett. Specialized junctions involved in electrical transmission between neurons. *Annals of the New York Academy of Sciences*, 137(2):495–508, 1966.

[68] Edwin J Furshpan and David D Potter. Low-resistance junctions between cells in embryos and tissue culture. *Current topics in developmental biology*, 3:95–127, 1968.

[69] Li H., Liu T.-F., Lazrak A., Peracchia C., Goldberg G.S., Lampe P.D., and Johnson R.G. Properties and regulation of gap junctional hemichannels in the plasma membrane of cultured cells. *J. Cell Biol.*, 134:1019–1030, 1996.

[70] MARTHA M Bosma. Anion channels with multiple conductance levels in a mouse b lymphocyte cell line. *The Journal of physiology*, 410:67, 1989.

[71] Thomas H Steinberg, Alan S Newman, JA Swanson, and Samuel C Silverstein. Atp4-permeabilizes the plasma membrane of mouse macrophages to fluorescent dyes. *Journal of Biological Chemistry*, 262(18):8884–8888, 1987.

[72] Louise C Nuttle and George R Dubyak. Differential activation of cation channels and non-selective pores by macrophage p2z purinergic receptors expressed in xenopus oocytes. *Journal of Biological Chemistry*, 269(19):13988–13996, 1994.

[73] A Surprenant, F Rassendren, E Kawashima, RA North, and G Buell. The cytolytic p2z receptor for extracellular atp identified as a p2x receptor (p2x7). *Science*, 272(5262):735, 1996.

[74] Rolf Dermietzel, Theng-Khing Hwang, Reinhard Buettner, Andreas Hofer, Elisabeth Dotzler, Marian Kremer, Rainer Deutzmann, Friedrich P Thinnes, Glenn I Fishman, and David C Spray. Cloning and in situ localization of a brain-derived porin that constitutes a large-conductance anion channel in astrocytic plasma membranes. *Proceedings of the National Academy of Sciences*, 91(2):499–503, 1994.

[75] H Sauer, J Hescheler, and M Wartenberg. Mechanical strain-induced ca2+ waves are propagated via atp release and purinergic receptor activation. *American Journal of Physiology-Cell Physiology*, 279(2):C295–C307, 2000.

[76] Hille B. Ionic channels in excitable membranes. current problems and biophysical approaches. *Biophys J.*, 22:283–294, 1978.

[77] Nielsen M.S., Axelsen L.N., Sorgen P.L., Verma V., Delmar M., and Holstein-Rathlou N.H. Gap junctions. *Compr Physiol.*, 2(3):1981–2035, 2012.

[78] Bukauskas F.F. and Verselis V.K. Gap junction channel gating. *Biochim Biophys Acta*, 1662:42, 2004.

[79] Verselis V. K., Ginter C. S., and Bargiello T. A. Opposite voltage gating polarities of two closely related connexins. *Nature*, 368:348–351, 1994.

[80] Feliksas F Bukauskas and Vytas K Verselis. Gap junction channel gating. *Biochimica et Biophysica Acta (BBA) - Biomembranes*, 1662:42–60, 2004.

[81] Sanchez Helmuth A., Slavi Nefeli, Srinivas Miduturu, and Verselis Vytas K. Syndromic deafness mutations at asn 14 differentially alter the open stability of cx26 hcmichanncls. *J. Gen. Physiol.*, 148:25–42, 2016.

[82] Loewenstein W.R. Permeability of membrane junctions. *Ann. NY Acad. Sci.*, 137:441–472, 1966.

[83] Werner R Loewenstein and Birgit Rose. Calcium in (junctional) intercellular communication and a thought on its behavior in intracellular communication. *Annals of the New York Academy of Sciences*, 307(1):285–307, 1978.

[84] Peracchia C. Chemical gating of gap junction channels; roles of calcium, ph and calmodulin. *Biochim Biophys Acta*, 1662:61–80, 2004.

[85] Peracchia A. C., Sotkis X.G., Wang L.L., Peracchia A., and Persechini. Calmodulin directly gates gap junction channels. *J Biol Chem*, 275:26220–26224, 2000.

[86] Katalin TÖRÖK, Kathryn Stauffer, and W Howard EVANS. Connexin 32 of gap junctions contains two cytoplasmic calmodulin-binding domains. *Biochemical Journal*, 326(2):479–483, 1997.

[87] Ryan Dodd, Camillo Peracchia, Daniel Stolady, and Katalin Török. Calmodulin association with connexin32-derived peptides suggests trans-domain interaction in chemical gating of gap junction channels. *Journal of Biological Chemistry*, 283(40):26911–26920, 2008.

[88] Gary S Burr, Cheryl K Mitchell, Yenabi J Keflemariam, Ruth Heidelberger, and John O'Brien. Calcium-dependent binding of calmodulin to neuronal gap junction proteins. *Biochemical and biophysical research communications*, 335(4):1191–1198, 2005.

[89] Monica M Lurtz and Charles F Louis. Intracellular calcium regulation of connexin43. *American Journal of Physiology-Cell Physiology*, 293(6):C1806–C1813, 2007.

[90] Yubin Zhou, Wei Yang, Monica M Lurtz, Yanyi Chen, Jie Jiang, Yun Huang, Charles F Louis, and Jenny J Yang. Calmodulin mediates the ca 2+-dependent regulation of cx44 gap junctions. *Biophysical journal*, 96(7):2832–2848, 2009.

[91] C Peracchia, KC Young, XG Wang, and LL Peracchia. Is the voltage gate of connexins co2-sensitive? cx45 channels and inhibition of calmodulin expression. *The Journal of membrane biology*, 195(1):53–62, 2003.

[92] Vuyst E.D., Decrock E., Cabooter L., Dubyak G.R., Naus C.C., Evans W.H., and Leybaert L. Intracellular calcium changes trigger connexin 32 hemichannel opening. *The EMBO Journal*, 25:34–44, 2006.

[93] Kamermans M., Fahrenfort I., Schultz K., Janssen-Bienhold U., Sjoerdsma T., and Weiler R. Hemichannel-mediated inhibition in the outer retina. *Science*, 292(5519):1178–1180, 2001.

[94] Pfahnl A. and Dahl G. Gating of cx46 gap junction hemichannels by calcium and voltage. *Pflugers Arch.*, 437(3):345–353, 1999.

[95] Liu S., Taffet S., Stoner L., Delmar M., Vallano M.L., and Jalife J. A structural basis for the unequal sensitivity of the major cardiac and liver gap junctions to intracellular acidification: the carboxyl tail length. *Biophys J*, 64:1422–1433, 1993.

[96] Morley G.E., Taffet S.M., and Delmar M. Intramolecular interactions mediate ph regulation of connexin43 channels. *Biophys J*, 70:1294–1302, 1996.

[97] Skerrett I.M. and Williams J. A structural and functional comparison of gap junction channels composed of connexins and innexins. *Developmental Neurobiology*, Accepted Article, 2016.

[98] Wei C.J., Xu X., and Lo C.W. Connexins and cell signaling in development and disease. *Annu. Rev. Cell Dev. Biol.*, 20:811–838, 2004.

[99] Laird D.W. Life cycle of connexins in health and disease. *Biochem. J.*, 394(Pt 3):527–543, 2006.

[100] Dobrowolski R. and Willecke K. Connexin-caused genetic diseases and corresponding mouse models. *Antioxid. Redox Signal.*, 11:283–295, 2009.

[101] VanSlyke J.K., Deschenes S.M., and Musil L.S. Intracellular transport, assembly, and degradation of wild-type and disease-linked mutant gap junction proteins. *Molecular Biology of the Cell*, 11:1933–1946, 2000.

[102] Bergoffen J., Scherer S.S., Wang S., Scott M.O., Bone L.J., Paul D.L., Chen K., Lensch M.W., Chance P.F., and Fischbeck K.H. Connexin mutations in x-linked charcot-marie-tooth disease. *Science*, 262(5142):2039–42, 1993.

[103] Balice-Gordon R.J., Bone L.J., and Scherer S.S. Unctional gap junctions in the schwann cell myelin sheat. *J. Cell Biol.*, 142:1095–1104, 1998.

[104] Steel K.P. and Kras C.J. A genetic approach to understanding auditory function. *Nature Genetics*, 27:143–149, 2001.

[105] Rabionet R., Gasparini P., and Estivill X. Molecular genetics of hearing impairment due to mutations in gap junction genes encoding beta connexins. *Human Mutations*, 16:190–202, 2000.

[106] Kelsell D.P., Dunlop J., and Hodgins M.B. Human diseases: clues to cracking the connexin code? *Trends in Cell Biology*, 11:2–6, 2001.

[107] Rouan F., White T.W., Brown N., Taylor A.M., Lucke T.W., Paul D.L., Munro C.S., Uitto J., Hodgins M.B., and Richard G. rans-dominant inhibition of connexin-43 by mutant connexin-26: implications for dominant connexin disorders affecting epidermal differentiation. *Journal of Cell Science*, 114:2105–2113, 2001.

[108] Pal J.D., Liu X., Mackay D., Shiels A., Berthoud V.M., Beyer E.C., and Ebihara L. Connexin46 mutations linked to congenital cataract show loss of gap junction channel function. *American Journal of Physiology*, 279:C596–C602, 2000.

[109] Bruzzone R., Veronesi V., Gomès D., Bicego M., Duval N., Marlin S., Petit C., D'Andrea P., and White T.W. Loss-of-function and residual channel activity of connexin26 mutations associated with non-syndromic deafness. *FEBS Letters*, 533:79–88, 2003.

[110] D'Andrea P., Veronesi V., Bicego M., Melchionda S., Zelante L., Di Iorio E., and Gasparini R., Bruzzone P. Hearing loss: frequency and functional studies of the most common connexin26 alleles. *Biochem Biophys Res Commun.*, 296(3):685–91, 2002.

[111] David C. Dawson. Permeability and conductance of ion channels a primer. In Stanley G. Schultz, Thomas E. Andreoli, M. Brown Arthur, M. Fambrough Douglas, Joseph F. Hoffman, and Michael J. Welsh, editors, *Molecular Biology of Membrane Transport Disorders*, chapter 5, pages 87–110. Plenum Press, New York and London, 1996.

[112] Hess B., Kutzner C., and other. Gromacs 4: Algorithms for highly efficient, load-balanced, and scalable molecular simulation. *Journal of chemical theory and computation*, 4:435–447, 2008.

[113] David A.Case, Thomas E.Cheatham, and other. The amber biomolecular simulation programs. *J Comput Chem*, 26:1668–1688, 2005.

[114] H.J.C. Berendsen, J.P.M. Postma, W.F. van Gunsteren, A. Dinola, and J.R. Haak. Molecular dynamics with coupling to an external bath. *The Journal of Chemical Physics*, 81:3684, 1984.

[115] Tom Darden, Darrin York, and Lee Pedersen. Article mesh ewald: an $nlog(n)$ method for ewald sums in large systems. *The Journal of Chemical Physics*, 98:10089, 1993.

[116] Nicolas Guex and Manuel C. Peitsch. Swiss-model and the swiss-pdb viewer: An environment for comparative protein modeling. *Electrophoresis*, 18:2714–2723, 1997.

[117] Rcsb protein data bank. http://www.pdb.org/pdb/home/home.do.

[118] Yong Duan, Chun Wu, Shibasish Chowdhury, Mathew C Lee, Guoming Xiong, Wei Zhang, Rong Yang, Piotr Cieplak, Ray Luo, Taisung Lee, et al. A point-charge force field for molecular mechanics simulations of proteins based on condensed-phase quantum mechanical calculations. *Journal of computational chemistry*, 24(16):1999–2012, 2003.

[119] Lindorff-Larsen K., Piana S., Palmo K., Maragakis P., Klepeis J.L., Dror R.O., and Shaw D.E. Improved side-chain torsion potentials for the amber ff99sb protein force field. *Proteins*, 78(8):1950–1958, 2010.

[120] Atsunori Oshima, Tomoko Doi, Kaoru Mitsuoka, Shoji Maeda, and Yoshinori Fujiyoshi. Roles of met-34, cys-64, and arg-75 in the assembly of human connexin 26 implication for key amino acid residues for channel formation and function. *Journal of Biological Chemistry*, 278(3):1807–1816, 2003.

[121] Gerhard Dahl, Eric LEVINE, Cristina RABADAN-DIEHL, and Rudolf WERNER. Cell/cell channel formation involves disulfide exchange. *European journal of biochemistry*, 197(1):141–144, 1991.

[122] Gerhard Dahl, Rudolf Werner, Eric Levine, and Cristina Rabadan-Diehl. Mutational analysis of gap junction formation. *Biophysical journal*, 62(1):172, 1992.

[123] Hela Azaiez, G Parker Chamberlin, Stephanie M Fischer, Chelsea L Welp, Sai D Prasad, R Thomas Taggart, Ignacio del Castillo, Guy Van Camp, and Richard JH Smith. Gjb2: The spectrum of deafness-causing allele variants and their phenotype. *Human mutation*, 24(4):305–311, 2004.

[124] M Khalifa Alkowari, G Girotto, K Abdulhadi, S Dipresa, R Siam, N Najjar, R Badii, and Paolo Gasparini. Gjb2 and gjb6 genes and the a1555g mitochondrial mutation are only minor causes of nonsyndromic hearing loss in the qatari population. *International journal of audiology*, 51(3):181–185, 2012.

[125] Ralf Birkenhäger, Nicola Prera, Antje Aschendorff, Roland Laszig, and Susan Arndt. A novel homozygous mutation in the ec1/ec2 interaction domain of the gap junction complex connexon 26 leads to profound hearing impairment. *BioMed research international*, 2014, 2014.

[126] Mary E Karpen, Douglas J Tobias, and Charles L Brooks III. Statistical clustering techniques for the analysis of long molecular dynamics trajectories: analysis of 2.2-ns trajectories of ypgdv. *Biochemistry*, 32(2):412–420, 1993.

[127] Simpson A.M., Swan M.A., Liu G.J., Tao C., O'Brien B.A, Ch'ng E., Castro L.M., Ting J., Elgundi Z., An T., Lutherborrow M., Torpy F., Martin D.K., Tuch B.E., and Nicholson G.M. Insulin trafficking in a glucose responsive engineered human liver cell line is regulated by the interaction of atp-sensitive potassium channels and voltage-gated calcium channels. In Molina F.M., editor, *Gene Therapy - Tools and Potential Applications*. CC BY 3.0 license, 2013.

[128] James Gumbart, Fatemeh Khalili-Araghi, Marcos Sotomayor, and Benoît Roux. Constant electric field simulations of the membrane potential illustrated with simple systems. *Biochimica et Biophysica Acta*, 1818:294–302, 2012.

[129] Benoît Roux. The membrane potential and its representation by a constant electric field in computer simulations. *Biophysical Journal*, 95:4205–4216, 2008.

[130] Aleksij Aksimentiev and Klaus Schulten. Imaging alpha-hemolysin with molecular dynamics: ionic conductance, osmotic permeability, and the electrostatic potential map. *Biophysical Journal*, 88:3745–3761, 2005.

[131] Liang Xua, Andrea Carrer, Francesco Zonta, Zhihu Qu, Sheng Li, Federico Ceriani, Damiano Buratto, Giulia Crispino, Veronica Zorzi, Gaia Ziraldo, Sichun Xie, Xuemei Yang, Jun Liao, Youjun Chu, Guang Yang, Richard A. Lerner, and Fabio Mammano. A human recombinant antibody that inhibits disease-related gain-of-function mutant connexin hemichannels. *Nature Medicine*, article under review.

[132] Charles A Janeway, Jr Paul Travers, Mark Walport, and Mark J Shlomchik. *The Immune System in Health and Disease*. Garland Science, 2001.

[133] The biology project. http://www.biology.arizona.edu, 2000. University of Arizona.

[134] J. S. Huston, D. Levinson, M. Mudgett-Hunter, M. S. Tai, J. Novotný, M. N. Margolies, and R. Crea. Protein engineering of antibody binding sites: recovery of specific activity in an anti-digoxin single-chain fv analogue produced in escherichia coli. *Proceedings of the National Academy of Sciences of the United States of America (PNAS)*, 85:5879–5883, 1988.

[135] Eric Peterson, SM Owens, and RL Henry. Monoclonal antibody form and function: Manufacturing the right antibodies for treating drug abuse. *AAPS Journal*, 8:E383–E390, 2006.

[136] Anuj Chaudhri, Isidro E. Zarraga, Sandeep Yadav, Thomas W. Patapoff, Steven J. Shire, and Gregory A. Voth. The role of amino acid sequence in the self-association of therapeutic monoclonal antibodies: Insights from coarse-grained modeling. *The Journal of Physical Chemistry B*, 117:1269–1279, 2013.

[137] Richard A. Lerner, Rajesh K. Grover, Hongkai Zhang, Jia Xie, Kyung Ho Han, Yingjie Peng, and Kyungmoo Yea. Antibodies from combinatorial libraries use functional receptor pleiotropism to regulate cell fates. *Quarterly reviews of biophysics*, 48:389–394, 2015.

[138] Hongkai Zhang, Ian A. Wilson, and Richard A. Lerner. Selection of antibodies that regulate phenotype from intracellular combinatorial antibody libraries. *Proceedings of the National Academy of Sciences of the United States of America*, 109:15728–15733, 2012.

[139] Emil Bujak, Mattia Matasci, Dario Neri, and Sarah Wulhfard. Reformatting of scfv antibodies into the scfv-fc format and their downstream purification. *Methods in Molecular Biology*, 1131:315–334, 2014.

[140] Noah A. Levit, Caterina Sellitto, Hong-Zhan Wang, Leping Li, Miduturu Srinivas, Peter R. Brink, and Thomas W White. Aberrant connexin26 hemichannels underlying keratitis-ichthyosis-deafness syndrome are potently inhibited by mefloquine. *J Invest Dermatol*, 135:1033–1042, 2015.

[141] Helmuth A. Sanchez, Rick Bienkowski, Nefeli Slavi, Miduturu Srinivas, and Vytas K. Verselis. Altered inhibition of cx26 hemichannels by ph and zn^{2+} in the a40v mutation associated with keratitis-ichthyosis-deafness syndrome. *The Journal of biological chemistry*, 289:21519–21532, 2014.

[142] Ilaria Fasciani, Ana Temperán, Leonel F. Pérez-Atencio, Adel Escuderoa, Paloma Martínez-Montero, Jesús Molano, Juan M. Gómez-Hernández, Carlos L. Paino, Daniel González-Nieto, and Luis C. Barrio. Regulation of connexin hemichannel activity by membrane potential and the extracellular calcium in health and disease. *Neuropharmacology*, 7:8770, 2013.

[143] Juan C. Sáez and Luc Leybaert. Hunting for connexin hemichannels. *FEBS letters*, 588:1205–1211, 2014.

[144] Juan C. Sáez, Mauricio A. Retamal, Daniel Basilio, Feliksas F. Bukauskas, and Michael V.L. Bennett. Connexin-based gap junction hemichannels: gating mechanisms. *Biochimica et biophysica acta*, 1711:215–224, 2005.

[145] Stephen R. Comeau, David W. Gatchell, Sandor Vajda, and Carlos J. Camacho. Cluspro: an automated docking and discrimination method for the prediction of protein complexes. *Bioinformatics*, 20:45–50, 2004.

[146] Ryan Brenke, David R. Hall, Gwo-Yu Chuang, Stephen R. Comeau, Tanggis Bohnuud, Dmitri Beglov, Ora Schueler-Furman, Sandor Vajda, and Dima Kozakov. Application of asymmetric statistical potentials to antibody-protein docking. *Bioinformatics*, 28:2608–2614, 2012.

[147] Sirah force field for amino acids, solvent and nucleotides. http://www.sirahff.com/2012/06/sirah-forcefield.html, 2016. SIRAH.

[148] Leonardo Darré, Matías Rodrigo Machado, Astrid Febe Brandner, Humberto Carlos González, Sebastián Ferreira, and Sergio Pantano. Sirah: A structurally unbiased coarse-grained force field for proteins with aqueous solvation and long-range electrostatics. *Journal of Chemical Theory and Computation*, 11(2):723–739, 2015.

[149] Damiano Buratto, Francesco Francesco, Carlos Cruz, Guang Yang, Sergio Pantano, and Fabio Mammano. Multi scale molecular dynamics simulations recover the permeable state of gap junction channels. -, unsabmitted article.

[150] Kmiecik S., Gront D., Kolinski M., Wieteska L., Dawid A.E., and Kolinski A. Coarse-grained protein models and their applications. *Chemical Reviews*, 116:53–62, 2016.

[151] Oesterle E.C. and Dallos P. Intracellular recordings from supporting cells in the guinea pig cochlea: Dc potentials. *Journal of Neurophysiology*, 64:617–636, 1990.

[152] Lautermann J., ten Cate Wouter-Jan F., Altenhoff Petra, Grümmer Ruth, Traub Otto, Frank H.-G., Jahnke Klaus, and Winterhager Elke. Intracellular recordings from supporting cells in the guinea pig cochlea: Dc potentials. *Cell and Tissue Research*, 294:415–420, 1998.

[153] David Chandler. Statistical mechanics of isomerization dynamics in liquids and the transition state approximation. *The Journal of Chemical Physics*, 68:2959, 1978.

[154] Benoît Roux and Martin Karplus. Ion transport in a gramicidin-like channel: dynamics and mobility. *The Journal of Physical Chemistry*, 95:4856–4868, 1991.

[155] Toby W.Allen, Olaf S.Andersen, and Benoît Roux. Molecular dynamics - potential of mean force calculations as a tool for understanding ion permeation and selectivity in narrow channels. *Biophysical Chemistry*, 124:251–267, 2006.

[156] John G. Kirkwood. Statistical mechanics of fluid mixtures. *The Journal of Chemical Physics*, 3:300, 1935.

[157] Hodgkin A.L. and Keynes R.D. The potassium permeability of a giant nerve fibre. *J. Physiol. (Lond.)*, 128:61–88, 1955.

[158] Heckmann K. Zur theorie der "single file"-diffusion. part i. *Phys. Chem.*, 44:184–203, 1965.

[159] Heckmann K. Zur theorie der "single file"-diffusion. part ii. *Phys. Chem.*, 46:1–25, 1965.

[160] Heckmann K. Zur theorie der "single file"-diffusion. part iii. sigmoide konzentrationsabhängigkeit unidirectionaler flüsse bei "single file" diffusion. *Z. Phys. Chem.*, 58:201–219, 1968.

[161] Heckmann K. Single-file diffusion. *Biomembranes*, Vol.3: Passive Permeability of Cell Membranes:127–153, 1972.

[162] Läuger P. Ion transport through pores: A rate-theory analysis. *Biochim. Biophys. Acta*, 311:423–441, 1973.

[163] Atsunori Oshima, Kazutoshi Tani, Masoud M. Toloue, Yoko Hiroaki, Amy Smock, Sayaka Inukai, Angela Cone, Bruce J. Nicholson, Gina E. Sosinsky, and Yoshinori Fujiyoshi. Asymmetric configurations and n-terminal rearrangements in connexin26 gap junction channels. *Journal of Molecular Biology*, 405:724–735, 2011.

[164] Ingrid M Skerrett, W-L Di, Eileen M Kasperek, David P Kelsell, and Bruce J Nicholson. Aberrant gating, but a normal expression pattern, underlies the recessive phenotype of the deafness mutant connexin26m34t. *The FASEB journal*, 18(7):860–862, 2004.

[165] Yun Luo, Angelo R. Rossi, and Andrew L. Harris. Computational studies of molecular permeation through connexin26 channels. *Biophysical Journal*, 110:584–599, 2016.

[166] Glenn M. Torrie and John P. Valleau. Monte carlo free energy estimates using non-boltzmann sampling: Application to the sub-critical lennard-jones fluid. *Chemical Physics Letters*, 28:578–581, 1974.

[167] Benoît Roux. The calculation of the potential of mean force using computer simulations. *Computer Physics Communications*, 91(1):275–282, 1995.

[168] John G Kirkwood. Statistical mechanics of fluid mixtures. *The Journal of Chemical Physics*, 3(5):300–313, 1935.

[169] Glenn M Torrie and John P Valleau. Nonphysical sampling distributions in monte carlo free-energy estimation: Umbrella sampling. *Journal of Computational Physics*, 23(2):187–199, 1977.

[170] Marc Souaille and Benoît Roux. Extension to the weighted histogram analysis method: combining umbrella sampling with free energy calculations. *Computer physics communications*, 135(1):40–57, 2001.

[171] inositol 1,4,5-trisphosphate(6-). http://www.ebi.ac.uk/chebi/searchId.do?chebiId=203600. CHEBI:203600.

[172] Atp. http://www.ebi.ac.uk/chebi/searchId.do?chebiId=CHEBI:15422#. CHEBI:15422.

[173] glucose. http://www.ebi.ac.uk/chebi/searchId.do?chebiId=CHEBI:15903. CHEBI:15903.

[174] M. J. Frisch, G. W. Trucks, H. B. Schlegel, G. E. Scuseria, M. A. Robb, J. R. Cheeseman, G. Scalmani, V. Barone, B. Mennucci, G. A. Petersson, H. Nakatsuji, M. Caricato, X. Li, H. P. Hratchian, A. F. Izmaylov, J. Bloino, G. Zheng, J. L. Sonnenberg, M. Hada, M. Ehara, K. Toyota, R. Fukuda, J. Hasegawa, M. Ishida, T. Nakajima, Y. Honda, O. Kitao, H. Nakai, T. Vreven, J. A. Montgomery, J. E. Peralta, F. Ogliaro, M. Bearpark, J. J. Heyd, E. Brothers, K. N. Kudin, V. N. Staroverov, R. Kobayashi, J. Normand, K. Raghavachari, A. Rendell, J. C. Burant, S. S. Iyengar, J. Tomasi, M. Cossi, N. Rega, J. M. Millam, M. Klene, J. E. Knox, J. B. Cross, V. Bakken, C. Adamo, J. Jaramillo, R. Gomperts, R. E. Stratmann, O. Yazyev, A. J. Austin, R. Cammi, C. Pomelli, J. W. Ochterski, R. L. Martin, K. Morokuma, V. G. Zakrzewski, G. A. Voth, P. Salvador, J. J. Dannenberg, S. Dapprich, A. D. Daniels, O. Farkas, J. B. Foresman, J. V. Ortiz, J. Cioslowski, and D. J. Fox. Gaussian 09 revision e.01. Gaussian Inc. Wallingford CT 2009.

[175] Wang J., Wang W., Kollman P. A., and Case D. A. Automatic atom type and bond type perception in molecular mechanical calculations. *Journal of Molecular Graphics and Modelling*, 25:247260, 2006.

[176] Wang J., Wolf R. M., Caldwell J. W., Kollman P. A., and Case D. A. Development and testing of a general amber force field. *Journal of Computational Chemistry*, 25:1157–1174, 2004.

[177] Somlyo A.P. and Somlyo A.V. Signal transduction and regulation in smooth muscle. *Nature*, 372:231–6, 1994.

[178] Worley P.F., Baraban J.M., and Snyder S.H. Inositol 1,4,5-trisphosphate receptor binding: autoradiographic localization in rat brain. *J. Neurosci.*, 9(1):339–46, 1989.

[179] Törnroth-Horsefield S. and Neutze R. Opening and closing the metabolite gate. *Proc. Natl. Acad. Sci. USA.*, 105(50):19565–19566, 2008.

[180] Lohmann K. Über die pyrophosphatfraktion im muskel. *Naturwissenschaften*, 17(31):624–625, 1929.

[181] Maruyama K. The discovery of adenosine triphosphate and the establishment of its structure. *J. Hist. Biol.*, 24(1):145–154, 1991.

[182] Martin R.B. Free energy and equilibria of peptide bond hydrolysis and formation. *Biopolymers*, 45(5):351–353, 1998.

[183] Stephen C. Harvey, Robert K.-Z. Tan, and Thomas E. Cheatham III. The flying ice cube: Velocity rescaling in molecular dynamics leads to violation of energy equipartition. *Journal of Computational Chemistry*, 19(7):726–740, 1998.

[184] Tariq A. Andrea, William C. Swope, and Hans C. Andersen. The role of long ranged forces in determining the structure and properties of liquid water. *The Journal of Chemical Physics*, 79:4576, 1983.

[185] P.P. Ewald. The calculation of optical and electrostatic grid potential. *ANNALEN DER PHYSIK*, 64(3):253–287, 1921.

[186] William L. Jorgensen, Jayaraman Chandrasekhar, Jeffry D. Madura, Roger W. Impey, and Michael L. Klein. Comparison of simple potential functions for simulating liquid water. *The Journal of Chemical Physics*, 79:926, 1983.

[187] David Leonard Chapman. Li. a contribution to the theory of electrocapillarity. *Philosophical Magazine Series 6*, 25(148):475–481, 1913.

[188] Svante Arrhenius. Über die reaktionsgeschwindigkeit bei der inversion von rohrzucker durch säuren. *Zeitschrift für physikalische Chemie*, 4:226–248, 1889.

[189] Henry Eyring. The activated complex in chemical reactions. *The Journal of Chemical Physics*, 3(2):107–115, 1935.

[190] Merdith G Evans and Michael Polanyi. Some applications of the transition state method to the calculation of reaction velocities, especially in solution. *Transactions of the Faraday Society*, 31:875–894, 1935.

[191] David Chandler. Statistical mechanics of isomerization dynamics in liquids and the transition state approximation. *The Journal of Chemical Physics*, 68(6):2959–2970, 1978.

[192] Peter Kollman. Free energy calculations: applications to chemical and biochemical phenomena. *Chemical reviews*, 93(7):2395–2417, 1993.

[193] Johannes Kästner. Umbrella sampling. *Wiley Interdisciplinary Reviews: Computational Molecular Science*, 1(6):932–942, 2011.

[194] Shankar Kumar, John M Rosenberg, Djamal Bouzida, Robert H Swendsen, and Peter A Kollman. The weighted histogram analysis method for free-energy calculations on biomolecules. i. the method. *Journal of computational chemistry*, 13(8):1011–1021, 1992.